FUNCTIONALIZATION OF GRAPHENE

NANOFLAKES THROUGH THERMAL PLASMA

Ulrich Legrand

Chemical Engineering Department

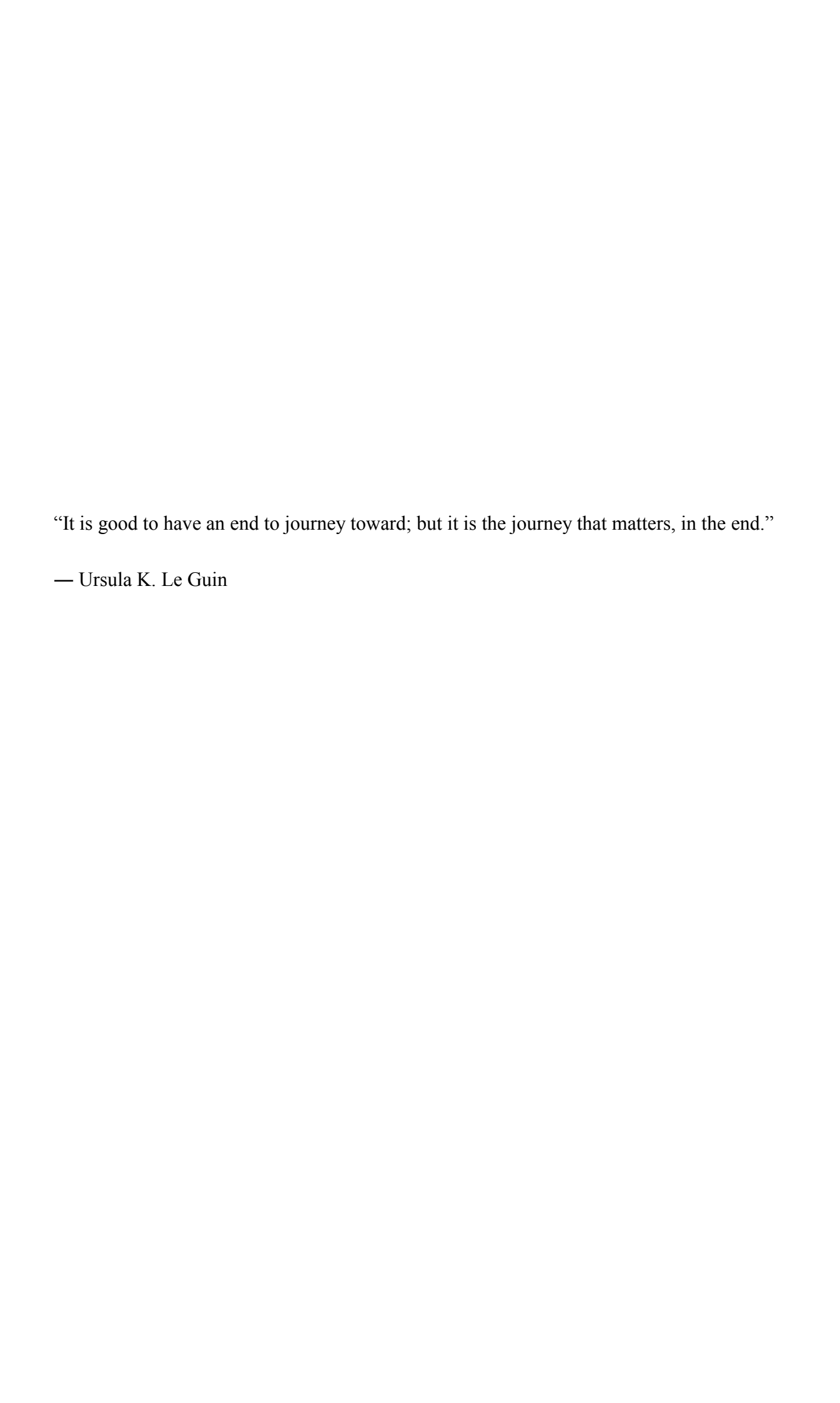
McGill University, Montréal

May 2017

A thesis submitted to McGill University in partial fulfillment of the requirements of the degree of Doctor of Philosophy

© Ulrich Legrand, 2017





ACKNOWLEDGEMENTS

I would like to thank my supervisors, Professors Jean-Luc Meunier and Dimitrios Berk for their guidance over the years. I am grateful they gave me help and advice when I needed it. Through their experience and knowledge, I was able to become an independent research scientist.

I would also like to thank my office mate and friend Pierre Pascone. He taught me everything I had to know about the graphene nanoflakes, and working with him on a daily basis was really refreshing. Our projects being similar on different aspects, I appreciated the insightful discussions and the mutual aid we gave each other. I draw a special attention to my lab mates from the Plasma Processing Laboratory, and especially Mathew Evans, Pablo Diaz Gomez Maqueo, Mark McArthur, Nathan Hordy and Rémi Laraque for making the Ph.D. an enjoyable experience. I would like to single out Norma Yadira Mendoza-Gonzalez for her time on the modelling of the plasma reactor.

A special thanks to my family who provided me support despite the long distance and to my girlfriend Charlotte who believed in me and encouraged me throughout this experience.

I would like to thank the staff at McGill who assisted me throughout my Ph.D.: Mrs. Jo-Ann Gadsby and the other academic staff for all of the administrative questions, Mr Frank Caporuscio for the safety aspect among many other things, Dr. David Liu for the electron microscopy imaging, and Dr. Cornelia Chilian for the neutron activation analysis.

Finally, this research would not have been possible without the financial support from the Natural Science and Engineering Research Council of Canada (NSERC) the Fonds de recherché du Québec Nature et Technologies (FRQNT), and McGill University.

ABSTRACT

This Ph.D. thesis explores the functionalization of graphene nanoflakes (GNFs) through a thermal plasma process. The GNFs are grown following an existing method developed by Pristavita *et al.* in 2011. Using the same thermal plasma reactor used to grow the GNFs, the plasma conditions are modified to introduce specific precursors, leading the GNFs functionalization. The growth and functionalization of the GNFs follow a single batch process in two steps, where the growth and deposition of the nanoparticles on the walls of the reactor represent the first step, and the functionalization the second step.

Following this method, iron functionalization is performed on nitrogen functionalized GNFs, for the synthesis of non-noble metal catalyst for the oxygen reduction reaction. First, aqueous iron salts and iron powders are tested as precursors for the functionalization step, leading to the deposition of iron oxide nanoparticles on the surface of the GNFs. The addition of iron oxide nanoparticles enhances the electrocatalytic activity of the samples compared to the non-functionalized samples. Then, iron (II) phthalocyanine solution is tested as the precursor to induce atomically dispersed iron on the surface of the GNFs. Again, an enhancement of the electrocatalytic activity of the functionalized samples is observed, with slightly higher performances than the iron oxide nanoparticles.

Sulphur functionalization of the GNFs is also described to make non-metal catalysts for the oxygen reduction reaction. The samples exhibit a complex composition, with sulphur atoms incorporated to the graphitic structure, but also sulphur based polymer partially covering the GNFs, and traces of orthorhombic sulphur. The resulting catalysts see an enhancement of their electrocatalytic activity, but lower compared to the iron based catalysts.

Finally, oxygen functionalities are added on the surface of the GNFs. The graphene nanoflakes are naturally hydrophobic, and the oxygen functionalities transform the

nanoparticles into fully hydrophilic material. The functionalized GNFs can be dispersed to form a stable nanofluid without the addition of surfactants. The resulting nanofluids are stable over months, and resist to a temperature up to 90°C in the case of water based nanofluids.

RÉSUMÉ

Cette thèse de doctorat s'attache à explorer la fonctionnalisation des nanoflocons de graphène (NFG) par plasma thermique. Les NFGs sont synthétisés par une méthode existante et développée par Pristavita *et al.* en 2011. À l'intérieur du même réacteur à plasma thermique servant à la synthèse des nanoflocons, les conditions plasma sont modifiées pour l'injection de précurseurs conduisant à la fonctionnalisation des nanoparticules. La synthèse et fonctionnalisation des NFGs est ainsi réalisée dans un processus batch en deux étapes, la première étape étant la synthèse des NFGs et leur dépôt sur la paroi du réacteur, la deuxième étape étant la fonctionnalisation.

En suivant cette méthode, une étape de fonctionnalisation au fer est réalisée sur des NFGs préalablement fonctionnalisés à l'azote, ayant pour but la réalisation de catalyseur à base de métaux non-nobles pour la réaction de réduction de l'oxygène. En premier lieu, une solution de fer aqueuse, ainsi que des poudres de fer sont testées comme précurseurs dans l'étape de fonctionnalisation, conduisant au dépôt de nanoparticules d'oxyde de fer sur les nanoflocons. L'addition des nanoparticules de fer provoque une augmentation de l'activité électrocatalytique des échantillons, lorsque comparé aux échantillons non-fonctionnalisés. Ensuite, une solution de phtalocyanine de fer (II) est utilisée comme précurseur de fer afin de créer une dispersion atomique de fer à la surface des NFGs. De nouveau, une amélioration de l'activité électrocatalytique des échantillons est observée, avec des performances légèrement meilleures qu'avec les nanoparticules d'oxyde de fer.

La fonctionnalisation au soufre des NFGs est aussi étudiée afin de créer des catalyseurs non-métalliques pour la réaction de réduction de l'oxygène. Les échantillons possèdent une composition relativement complexe, avec des atomes de soufre intégrés dans la structure graphitique, mais aussi un polymère à base de soufre couvrant partiellement les

NFGs, ainsi que des traces de soufre solide orthorhombique. Les catalyseurs à base de graphène et de soufre présentent eux aussi une amélioration de leur activité électrocatalytique, mais dans une moindre mesure comparée aux catalyseurs à base de fer.

Finalement, des groupes fonctionnels d'oxygène sont ajoutés à la surface des NFGs. Les nanoflocons sont naturellement hydrophobes, et les groupes fonctionnels d'oxygène transforment les nanoparticules en matériau parfaitement hydrophile. Les NFGs fonctionnalisés à l'oxygène sont capables d'être dispersés en un nanofluide stable sans l'addition de molécules tensio-actives. Les nanofluides à base de graphène fonctionnalisés restent stable sur une période de plusieurs mois, et résistent à une température jusqu'à 90°C dans le cas de nanofluides à base d'eau.

TABLE OF CONTENTS

Acknowledg	gements	l
Abstract		ii
Résumé		iv
Table of Co	ontents	vi
List of Table	es	ix
List of Figur	res	x
List of abbro	eviations	
CHAPTER 1	INTRODUCTION	1
1. Problem o	definitiondefinition	1
2. Objective	?s	2
3. Organisa	tion of the thesis	
CHAPTER 2	BACKGROUND & LITERATURE REVIEW	5
PART I THERM.	IAL PLASMA	5
1. Descripti	ion of thermal plasma	5
2. Thermal p	plasma torches	6
3. Application	ons of thermal plasma	7
3.1. Plasma s	spraying & powder spheroidisation	7
	reatment	
·	rticles synthesis	
4. Plasma fi	unctionalization	10
PART II CARBO	ON NANOPARTICLES	12
2. Carbon b	plack	13
3. Diamond	ls	14
4. Carbon n	anotubes	16
5. Graphene	e and stacked-graphene	18
	ICATIONS FOR THE FUNCTIONALIZED NANOPARTICLES	
1. Alkaline I	Fuel cells	20
	l types	
1.2. Oxygen	reduction reaction in AFCs	22
1.3. Platinum	n catalyst for the ORR	23
1.4. Alternat	tives of platinum catalysts	24
2. Nanofluid	ds	27
CHAPTER 3	EXPERIMENTAL EQUIPMENT AND M	MATERIAL
CHARACTERI	IZATION	30
PART I THERM.	IAL PLASMA REACTOR	30
1. RF Gener	rator	30
	h	
	oling system	
	system	
	reactor	
6. Precurson	r and main gas feeding techniques	36
6.1. Gas feed	ding	36
6.2 Liquid n	recursors	37

6.3. Solid precursorsPART II CHARACTERIZATION TECHNIQUES	
1. Scanning electron microscopy	
2. Transmission electron microscopy	
3. Energy dispersive X-ray spectroscopy	
4. X-ray photoelectron spectroscopy	
5. Neutron activation analysis	
6. Raman spectroscopy	
7. X-Ray Diffraction	
8. Thermogravimetric analysis	
9. UV-visible spectroscopy	
10. Rotating disk electrode	
CHAPTER 4 IRON FUNCTIONALIZATION OF	
NANOFLAKES FOR NON-NOBLE METAL CATALYST	APPLICATIONS49
PART I IRON FUNCTIONALIZATION ON GRAPHENE NANOFLAKES	USING IRON POWDERS
AND IRON ACETATE AS PRECURSORS	49
1. Introduction	
2. Experimental methods	53
2.1. Catalyst generation	53
2.2. Physical characterization	56
2.3. Electrochemical characterization	
3. Results and discussion	58
3.1. Structure of the N/Fe-GNFs	58
3.2. Chemical composition of the N/Fe-GNFs	64
3.3. Activity of the catalysts	70
3.4. Discussion	72
4. Conclusion	74
PART II IRON FUNCTIONALIZATION ON GRAPHENE NANOFLA	KES USING IRON (II)
PHTHALOCYANINE AS PRECURSOR	75
1. Introduction	
2. Materials and methods	78
2.1. Catalyst synthesis	78
2.2. Physical characterization	80
2.3. Electrochemical characterization	
3. Results and discussion	82
3.1. Chemical composition of the N/Fe-GNFs	82
3.2. Observation of the N/Fe-GNFs	85
3.3. Crystallinity of the samples	86
3.4. Electrocatalytic activity of the N/Fe-GNFs	
4. Conclusion	
CHAPTER 5 SULPHUR FUNCTIONALIZATION OF	
NANOFLAKES FOR NON-METAL CATALYST APPLICATION OF THE PROPERTY	
PART I ADDITION OF SULPHUR TO GRAPHENE NANOFLAKES US	
FOR OXYGEN REDUCTION REACTION IN ALKALINE MEDIUM 1. Introduction	
2. Experimental methods	
*	
2.1. Catalyst synthesis	97

2.2. Physical characterization	100
2.3. Electrochemical characterization	
3. Results and discussion	102
3.1. Thermodynamic considerations	102
3.2. Elemental composition of the S-GNFs	104
3.3. Structure of the S-GNFs	109
3.4. Electrocatalytic activity of the S-GNFs	114
3.5. Discussion	
4. Conclusion	
PART II ADDITIONAL INFORMATION ON THE SULPHUR FUNCTIONALIZAT	`
PUBLISHED): TEM ANALYSISCHAPTER 6 OXYGEN FUNCTIONALIZATION OF THE GR	
NANOFLAKES FOR NANOFLUID APPLICATIONS	
PART I SYNTHESIS AND IN-SITU OXYGEN FUNCTIONALIZATION OF	DEPOSITED
GRAPHENE NANOFLAKES FOR NANOFLUID GENERATION	122
1. Introduction	124
2. Methods	126
3. Results and discussion	131
3.1. Oxygen content	131
3.2. Homogeneity and crystallinity	135
3.3. Decomposition temperature	141
3.4. Dispersion tests	142
4. Conclusion	
PART II ADDITIONAL INFORMATION ON THE OXYGEN FUNCTIONALIZAT	
PUBLISHED): STUDY ON THE NANOFLUID STABILITY	
1. Absorption coefficient of the materials	
2. Stability over the time	
3. Stability after heating in water	
4. Further characterization of the O-GNFs based nanofluids	
4.1. Stability after heating in Ethylene Glycol	152
4.2. Influence of the pH on the nanofluid stability	
CHAPTER 7 CONCLUSION AND RECOMMENDATIONS	
1. Conclusion	
2. Original contribution	
3. Recommendations	157
REFERENCES 159	

LIST OF TABLES

LIST OF FIGURES

FIGURE 2-1: REPRESENTATION OF THE HEXAGONAL GRAPHITE STRUCTURE, SHOWING THE UNIT CELL [38]
FIGURE 2-2: TURBOSTRATIC STRUCTURE (RIGHT) COMPARED TO THE PERFECT GRAPHITE STRUCTURE (LEFT) [42]
FIGURE 2-3: REPRESENTATION OF THE DIAMOND STRUCTURE
Figure 2-4: Representation of a single-wall (left) and multi-wall (right) carbon nanotube
FIGURE 2-5: STRUCTURE OF A POSSIBLE CATALYTIC SITE, INSPIRED BY [82]
Figure 2-6: Possible structures of iron-based catalyst sites incorporated in graphene sheets proposed by Kramm et al. [83]. For each catalytic site, a top and side view is given, as well as the energy scheme and filling of the orbitals for the iron (II) ion. The three cases A, B and C are extracted from doublets obtained in a Mössbauer analysis
FIGURE 3-1: PICTURE OF THE EXPERIMENTAL SET-UP. (A) CONTROL CONSOLE (B) RF GENERATOR (C) ICP TORCH IN THE FARADAY CAGE (D) CONICAL REACTOR (E) EXHAUST CONNECTED TO THE VACUUM PUMP
FIGURE 3-2: SCHEMATIC OF AN ICP TORCH (©TEKNA). 32
FIGURE 3-3: TEMPERATURE PROFILE AND STREAM FUNCTION OF AN ARGON PLASMA IN THE CONICAL REACTOR
Figure 3-4: (Left) Mapping of the condensation coefficient for the GNFs in the argon thermal plasma. (Right) Zoom-in on the nucleation and growth region on the central axis [28]
Figure 3-5: The liquid injection system based on a stainless steel syringe and a push-syringe
Figure 3-6: The powder feeder
FIGURE 4-1. SEM PICTURE OF THE SAMPLES A) N/Fe-GNF8 AND B) N/Fe-GNF1 FOR A SCALE BAR OF 500 NM
FIGURE 4-2. TEM PICTURE OF N/FE-GNF5 WITH A SCALE BAR OF 200 NM, WITH EDX SPECTRA OF THE ZONE A, CONTAINING IRON OXIDE NANOPARTICLES (IN RED) AND THE ZONE B, CONTAINING ONLY GNFS (IN BLACK)
FIGURE 4-3. HIGH RESOLUTION TEM PICTURE OF N/FE-GNF1
FIGURE 4-4: RAMAN SPECTRA FOR NON-FUNCTIONALIZED AND TWO FUNCTIONALIZED SAMPLES (N/Fe-GNF1 AND N/Fe-GNF5)
FIGURE 4-5: XPS SURVEY SCAN OF TWO SAMPLES (N/Fe-GNF1 AND N/Fe-GNF6) COMPARED TO THE N-GNFS
Figure 4-6: High resolution of Carbon C1s peak for the eight samples compared to the non-functionalized GNFs. 67
Figure 4-7: High resolution and deconvolution peak of nitrogen N1s from the samples N/Fe-GNF1 and N/Fe-GNF8. N1, N2 and N3 are respectively associated to pyridinic, pyrrolic and graphitic nitrogen

FIGURE 4-8: HIGH RESOLUTION OF IRON XPS PEAK FROM THE SAMPLE N/Fe-GNF2
Figure 4-9. Linear sweep voltammetry of samples N/Fe-GNF1 (blue) and N/Fe-GNF5 (red) compared to the N-GNFs in $\rm O_2$ saturated 0.1 M NaOH, at a scan rate of 20 mV/s, for a rotation speed of 2500 rpm
FIGURE 4-10: (A) TYPICAL XPS SURVEY OBTAINED FOR N-FE/GNF7. HIGH RESOLUTION PEAKS OF (B) CARBON C1s, (C) NITROGEN N1s, (D) OXYGEN O1s FOR THE SAMPLE N-FE/GNF7. N1, N2, N3 AND N4 RESPECTIVELY CORRESPOND TO OXIDIZED, QUATERNARY, PYRROLIC, AND PYRIDINIC NITROGEN
Figure 4-11: Observation of the sample N-Fe/GNF8 under (a) SEM with a bar scale of 1 μM and (b) TEM with a bar scale of 200 nm. $$
FIGURE 4-12: RAMAN SPECTRUM OF THE SAMPLE N-FE/GNF3
FIGURE 4-13: (A) LSV OF TWO TYPICAL CATALYSTS COMPARED TO THE NON-FUNCTIONALIZED GNFS. (B) LSV AT ROTATION RATES BETWEEN 100 AND 2500 RPM FOR THE SAMPLE N-FE/GNF3
FIGURE 5-1: LEFT: OVERALL ICP THERMAL PLASMA REACTOR GEOMETRY USING A CONICAL EXPANSION FOR CONTROLLING THE FLOW PATTERNS AND THE LOCATION OF THE NANOPARTICLE NUCLEATION ZONES, AND A PUMPING MANIFOLD FOR AXIAL GAS EXHAUST IN A STAGNATION-POINT FLOW GEOMETRY. RIGHT: MODELLING RESULTS OF TYPICAL TEMPERATURE PROFILES (LEFT SIDE) AND THE NARROW ZONE OF GRAPHENE NUCLEATION (RIGHT SIDE, RED MAPPING) [28]
Figure 5-2: Equilibrium thermodynamic evaluation of the nature and amount of species generated from the decomposition and recombination of carbon disulphide in an argon thermal plasma as a function of temperature (0.017 moles of CS_2 in 2.54 moles of Ar).
FIGURE 5-3: XPS SPECTRUM OF THE S-GNFS. (A) SURVEY OF THE SAMPLE S-GNF1. HIGH RESOLUTION SULPHUR S2P PEAK OF (B) S-GNF1 AND (C) S-GNF7. HIGH RESOLUTION PEAK OF CARBON C1S OF (D) S-GNF1 AND (E) S-GNF7
FIGURE 5-4: (A) RAMAN SPECTRUM OF S-GNF1. DECONVOLUTION OF THE D-G PEAKS OF (B) S-GNF1 AND (C) S-GNF8
FIGURE 5-5: (A) X-RAY DIFFRACTOGRAM OF S-GNF3, (B) COMPARISON BETWEEN S-GNF3 (IN BLACK) AND ORTHORHOMBIC SULPHUR (IN RED) TAKEN FROM RRUFF DATABASE [154], (C) X-RAY DIFFRACTOGRAM OF S-GNF8
FIGURE 5-6: SEM MICROGRAPHS OF (A) S-GNF8 AND (B) S-GNF4
Figure 5-7: (a) LSV of some representative S-GNFs samples, (b) LSV for S-GNF6 for rotation rate from 100 to 2500 rpm, (c) Koutecky-Levich Plot for S-GNF6 at 0.0, 0.2 and 0.4 V, (d) Number of electrons transferred to the ORR for some representative S-GNFs samples at different potentials
FIGURE 5-8: TEM MICROGRAPHS OF THE SAMPLE S-GNFS SHOWING AREAS WITH (A) PRESENCE OF POLYMER (B) ABSENCE OF POLYMER. THE RED CIRCLE REPRESENTS THE AREA WHERE THE RESPECTIVE EDX SPECTRA HAVE BEEN RECORDED IN (C) AND (D). 119
Figure 5-9: High resolution micrograph showing the sulphur based plasma polymer covering GNFs

PIGURE 6-1: TEMPERATURE AND VELOCITY PROFILES FOR TESTED CONDITIONS: A) 55.2 KPA 20 kW and B) 13.8 kPa / 25 kW for a length scale bar of 5cm. Note the velocity fields are higher by a factor 4 in the (B) case
FIGURE 6-2: XPS SURVEY SCAN OF O-GNFS (SAMPLE C)
FIGURE 6-3: HIGH RESOLUTION AND DECONVOLUTION OF OXYGEN PEAK ANI DECONVOLUTION FOR O-GNFs (SAMPLE C)
FIGURE 6-4: HIGH RESOLUTION AND DECONVOLUTION OF CARBON PEAK FOR O-GNFs FROM SAMPLE C
FIGURE 6-5: SEM PICTURE OF A) NON-FUNCTIONALIZED GNFs AND B) O-GNFs FROM SAMPLE C, FOR A LENGTH SCALE BAR OF 2 μ M
FIGURE 6-6: TEM PICTURE OF NON-FUNCTIONALIZED GNFS (TOP) AND 14.2 AT%O-GNFS FROM SAMPLE C (BOTTOM), FOR A LENGTH SCALE BAR OF RESPECTIVELY 10 NM AND SMM. THE ELECTRON DIFFRACTION PATTERN FOR BOTH MATERIALS ARE ADDED. AS ENLARGEMENT OF THE O-GNFS EDGES IN THE BOTTOM RIGHT CORNER SHOWS A STRUCTURE HAVING 19 GRAPHENE PLANES.
Figure 6-7: Identification of the diffraction pattern for graphitic materials [172]
FIGURE 6-8: RAMAN SPECTRUM FOR NON-FUNCTIONALIZED GNFs (TOP) AND O-GNFS FROM SAMPLE C (BOTTOM)
FIGURE 6-9: TGA PROFILE FOR 14.2 AT%O-GNFs (SAMPLE C) AND NON-FUNCTIONALIZED GNFs in full lines with their respective derivative in dash lines
FIGURE 6-10: ZETA POTENTIAL MEASUREMENTS FOR THE A, B, C AND D SAMPLES IN A 1 MN NAHCO3 SOLUTION
Figure 6-11. Observed stability after 6 weeks for a) O-GNFs with 14.2 at% Oxygen in ethanol b) O-GNFs with 14.2 at% Oxygen in water c) O-GNFs with 6.4 at% Oxygen in water and d) non-functionalized GNFs in water
Figure 6-12: Average (15 measurements) of the absorbance coefficient of the O GNFs, EOG and GO nanofluids with the 95% confidence interval calculated based on concentrated suspensions from 5 to 200 mg/L
FIGURE 6-13: TIME EVOLUTION OF THE RELATIVE CONCENTRATION OF THE NANOFLUIDS. 149
Figure 6-14: Relative concentration of the O-GNFs suspensions in water after heating at 90°C for 1h. The line at 100% represents no change in the concentration before and after the heating step
FIGURE 6-15: AVERAGE OF THE RELATIVE CONCENTRATION OF THE O-GNFS, EOG AND GO NANOFLUIDS IN WATER AFTER HEATING AT 90°C FOR 1H. THE LINE AT 100% REPRESENTS NO CHANGE IN THE CONCENTRATION BEFORE AND AFTER THE HEATING STEP.
FIGURE 6-16: RELATIVE CONCENTRATION OF THE O-GNFs SUSPENSIONS IN ETHYLENG GLYCOL AFTER HEATING AT 90°C FOR 1H. THE LINE AT 100% REPRESENTS NO CHANGI IN THE CONCENTRATION BEFORE AND AFTER THE HEATING STEP
FIGURE 6-17: AVERAGE OF THE RELATIVE CONCENTRATION OF THE O-GNFs IN WATER HAVING A RANGE OF PH FROM 2 TO 12. THE LINE AT 100% REPRESENTS NO CHANGE IN THE CONCENTRATION

LIST OF ABBREVIATIONS

AFC: Alkaline Fuel Cell

at%: Atomic Percent

CFD: Computational Fluid Dynamics

CNT: Carbon Nanotube

CVD: Chemical Vapour Deposition

DC: Direct Current

EDX: Energy Dispersive X-ray spectroscopy

GNF: Graphene Nanoflake

GO: Graphene Oxide

HR-TEM: High Resolution Transmission Electronic Microscopy/Micrograph

ICP: Inductively Coupled Plasma

LTE: Local Thermodynamic Equilibrium

MCFC: Molten Carbonate Fuel Cell

N/Fe-GNF: Nitrogen and Iron Functionalized Graphene Nanoflake

NAA: Neutron Activation Analysis

N-GNF: Nitrogen Functionalized Graphene Nanoflake

NNMC: Non Noble Metal Catalyst

O-GNF: Oxygen Functionalized Graphene Nanoflake

ORR: Oxygen Reduction Reaction

PAFC: Phosphoric Acid Fuel Cell

PEMFC: Polymer Electrolyte Membrane/Proton Exchange Membrane Fuel Cell

RDE: Rotating Disk Electrode

RF: Radio Frequency

RGO: Reduced Graphene Oxide

RHE: Reverse Hydrogen Electrode

SEM: Scanning Electron Microscopy/Micrograph

S-GNF: Sulphur Functionalized Graphene Nanoflake

SHE: Standard Hydrogen Electrode

SOFC: Solid Oxide Fuel Cell

SWNT: Single Wall Carbon Nanotube

TEM: Transmission Electron Microscopy/Micrograph

TGA: Thermogravimetric Analysis

UV: Ultraviolet

wt%: Weight Percent

XPS: X-ray Photoelectron Spectroscopy

XRD: X-Ray Diffraction

Chapter 1 Introduction

1. Problem definition

Graphene has drawn a lot of attention from 2004 when a research group in Manchester isolated single sheets of graphene by peeling graphite [1]. This material being only one atom thick exhibited outstanding properties in terms of strength and electrical conductivity. These properties make graphene interesting for many applications, including electronics, medicine, energy storage, sensors, and many others [2]. For some of these applications, graphene has to be functionalized, meaning its surface chemistry has to be modified with the incorporation of functional groups. For example, the addition of NO₂ or NH₃ molecules in the structure of graphene leads to the creation of respectively p-type and n-type semiconductors [3].

The main issue for the full industrial use of graphene in its potential application is its production method. Indeed, techniques which produce the purest graphene, such as chemical vapour deposition, do not generate industrial quantities of graphene [4]. Also, techniques which produce large amount of graphene, such as exfoliation of graphite followed by graphene oxide reduction, lead to a material having a lot of crystalline defects [5], lowering the overall performances of graphene.

Pristavita *et al.* developed in 2011 a thermal plasma technique to produce nanoparticles of stacked graphene, referred to as graphene nanoflakes [6]. Even if these nanoparticles are a stacked of graphene layers and not single layers, most techniques to produce graphene actually lead to the formation of a few layers stacked together, which have similar properties to single layer graphene [7]. The graphene nanoflakes exhibit a crystalline

structure with a much lower defect content, and the plasma technique can be scaled-up for larger quantities of material.

By adding nitrogen gas in the thermal plasma reactor, Pristavita succeeded in incorporating nitrogen functionalities in the structure of the GNFs, up to 2 at% of nitrogen on the surface of the nanoparticles [6]. Binny increased the nitrogen content up to 25 at% by developing a functionalization step where the argon plasma was replaced by a nitrogen plasma [8]. In this process, the nanoparticles were functionalized using the downstream afterglow of the nitrogen thermal plasma. The aim for the addition of nitrogen functionalities to graphene was the development and synthesis of non-noble metal catalysts for the oxygen reduction reaction occurring in the anode of a fuel cell [9]. Indeed, the addition of nitrogen and iron on a carbon matrix can lead to the formation of catalytic sites dispersed at the atomic level, which is of great interest in the scientific and industrial community.

This thesis continues the work initiated by Pristavita, by developing an iron functionalization step to the existing GNFs growth step. Following the same two-stage method, other types of functionalization are explored in this thesis. Sulphur is added to the GNFs in order to generate non-metal catalysts for the oxygen reduction reaction. Oxygen functionalities are also added on the surface of the GNFs to make them hydrophilic and allow their dispersion into a stable nanofluid, and make the preparation of a catalyst ink more efficient.

2. Objectives

This Ph.D. project focuses on implementing one or more functionalization steps with different elements (iron, oxygen and sulphur) to the existing graphene nanoflakes synthesis for different applications, and more particularly to act as a catalyst for the oxygen

reduction reaction (ORR) in alkaline fuel cells (AFCs). The specific objectives for the thesis are listed below:

- Provide the atomic dispersion of iron coordinated to nitrogen on the surface of the nitrogen functionalized graphene nanoflakes using the downstream recombining zone of a thermal plasma stream.
- 2) Functionalize graphene nanoflakes by generating reactive species in the afterglow of the thermal plasma and adding sulphur functionalities on the surface of the graphene nanoflakes for the development of a non-metal catalyst using supports.
- 3) Evaluate the improvement of graphene nanoflakes dispersion in a fluid by the addition of oxygen functionalities on the surface of the nanoparticles for facilitating the preparation of catalysts inks in order to optimize the integration of GNF-based catalysts within the fuel cell stack and allow their full surface area potential for current transfer.

The methodology for reaching these objectives includes the identification of the appropriate precursor and the development of a feeding method within the thermal plasma reactor to generate and sustain reactive species able to functionalize the surface of the nanoparticles in the case of the iron, sulphur and oxygen functionalization. This methodology also involves the development of a single batch process including graphene nanoflakes growth and functionalization step needing no additional processing step after the powder collection.

3. Organisation of the thesis

This thesis consists of 7 chapters. After the Introduction, Chapter 2 provides a literature review in relation with the background of the project. This includes a presentation of the thermal plasma technology and its different applications, followed by an overview of the existing carbon nanoparticles. Finally, the applications using the functionalized GNFs are

detailed. The experimental apparatus used to grow and functionalize the GNFs is described in Chapter 3, as well as the different characterization techniques commonly employed in the following chapters. The main results are summarized in Chapters 4 to 6, consisting in articles accepted or submitted in peer-reviewed journals. Chapter 4 focuses on the iron functionalization of the graphene nanoflakes for non-noble metal catalysts application. Chapter 5 depicts the functionalization of the GNFs with sulphur for non-metal catalysts application. Chapter 6 covers the oxygen functionalization of the GNFs for nanofluids application. A final chapter summarizes the conclusions of the different studies, gives an overview of the contributions brought during this thesis, and suggests some recommendations for future work.

Chapter 2 BACKGROUND & LITERATURE REVIEW

Part I Thermal plasma

This part aims to provide a background on the thermal plasma technology by briefly describing the specific nature of a thermal plasma, how it is generated at the laboratory scale and its different applications.

1. Description of thermal plasma

Plasma is the fourth state of matter and composes more than 99% of the known matter in the universe, but represents only less than 1% of the matter on Earth. The plasma state is made of charged particles, such as electrons and ions, but also neutral particles, photons, excited species and electromagnetic radiations. Despite being composed of charged particles, plasmas globally respect the principle of quasineutrality, where negative and positive particles compensate each other in large volume scales. The plasma quasineutrality is not true on shorter length scales, where the charged particles can be shielded from each other and areas depleted from ions or electrons are formed [10].

An important aspect of plasmas is their collective behaviour compared to neutral gases. Atoms in a neutral gas can only interact by collisions with other atoms, typically through short range Van der Waals forces. In plasmas, charged particles can interact with each other with the Coulomb force, an electrostatic interaction over long distances. A large number of charged particles can show a simultaneous response to an external perturbation. A common way to describe plasmas is through the plasma parameter λ_D , referring to the Debye length. The Debye length is the distance in which mobile charge carriers, electrons in the case

of plasmas, screen out the external electric field. The Debye length is a scaling parameter dependent on the electron density and temperature.

Neutral gases can be described by the equations of fluid mechanics, but the nature and composition of plasmas make them more complex to describe. Indeed, electromagnetic interactions from Maxwell equations have to be coupled with the Navier-Stokes equations to predict the plasma motion and behaviour. Thermal plasmas, contrary to cold plasmas, are generally assumed to be close to local thermodynamic equilibrium (LTE) [11]. Plasma in thermodynamic equilibrium is considered in a closed system, where each process is in equilibrium with its reverse process. In this ideal case, the plasma can be characterized with the Boltzmann distribution for the population of excited states, the Maxwell distribution for the velocities, the Saha equation for the ionization degree, and Planck's law for the blackbody radiation. In real plasmas, the equilibrium can be altered for example by the radiation escaping the plasma, but remains valid locally, it is the local thermodynamic equilibrium (LTE). In the LTE, the relations mentioned above remain valid locally with the exception of Planck's law [11]. In this case, the plasma is determined by the collisions, and the radiation processes are neglected. In cold plasmas, or non-equilibrium plasmas, the temperature of the heavy species is much lower than the electron temperature, causing large variation from equilibrium, and none of the relations mentioned remain valid.

2. Thermal plasma torches

Different technologies are used in industry to produce thermal plasmas, and mainly differing by the type of discharges maintaining the plasma [12]. The most common plasma torches are based on direct current (DC) or radio-frequency (RF) discharges. In the DC torch, an electric arc is formed between two electrodes, and a plasma jet is formed by feeding gas around and through the electric arc [11]. DC torches can be operated in two specific modes:

non-transferred and transferred. In the non-transferred DC mode, the electrodes which generate the plasma arc are both contained within the plasma torch body and the high temperature plasma jet is used as a downstream processing plasma. In the transferred DC mode, one electrode is outside the plasma torch, and is generally made of the conductive material to be treated. Inert gases are generally used as carrier gas, such as nitrogen, helium, argon or hydrogen. Unless a good shielding of the electrodes is made, oxidizing gases are generally not recommended due to a potentially higher rate of electrode erosion affecting both their lifetime and the resulting levels of contamination.

On the other side, RF inductively coupled plasma (RF-ICP) torches work by coupling energy to the plasma by the help of an electromagnetic field [11]. A time-varying current is passed through a coil, inducing a time-varying magnetic field around the coil. This magnetic field creates an electric field in the carried gas, resulting in the ionization of the gas. The coil is isolated from the plasma typically by a heavily cooled ceramic tube so that no electrodes participating in the discharge are in contact with the plasma itself. This leads to much larger flexibility in terms of the types of gases that can be introduced in an ICP torch, such as reducing, oxidizing, or corrosive gases, enabling more possibilities in terms of treatment or functionalization.

3. Applications of thermal plasma

Thermal plasmas are widely spread in industry for specific applications. Some of these applications are described in this section.

3.1. Plasma spraying & powder spheroidisation

Both plasma spraying and powder spheroidisation techniques are using solid precursors to be injected into a plasma jet for different purposes.

In the plasma spraying technique, the particles are rapidly heated and accelerated at high velocity to be deposited on a substrate and form a coating. Metallic and ceramics powders having a high melting point can be easily used in plasma spraying. Coatings made by plasma spraying result in stronger, denser and cleaner coatings than the other spraying techniques [13]. For example, many pieces of a jet engine, exposed to combustion gases are covered by plasma coated zirconia, leading to a higher thermal resistance and a longer lifetime of the coating [14].

As its name indicates, the powder spheroidisation is the transformation of any powder into perfectly spherical particles through thermal plasma processing [15]. High melting temperature metals, such as tungsten, titanium or molybdenum are used in this process, and can come from used materials to be recycled. The high temperature from thermal plasma melts the fed powder and the controlled plasma flow allows high-density spherical particles to solidify. Low melting point metals are not suitable for this technique, because the metal could be vaporized instead of molten. Spherical powders contain less impurities which have been vaporized by the thermal plasma. Powders obtained by plasma spheroidisation exhibit interesting properties in terms of flowability, mechanical properties and chemical purity [16].

3.2. Waste treatment

Plasma waste treatment is an interesting alternative to landfills or simple incineration, which expose environment to pollution and greenhouse gases [17,18]. Thermal plasma can be used to vaporize and destroy any waste at high temperature. Most of human waste is made of organics which can be decomposed into carbon, oxygen and hydrogen atoms, leading to the production of carbon monoxide and hydrogen. This gas mixture can be later reused as a fuel. Inorganics contained in waste can be vitrified, meaning they are trapped

into a silicate matrix to form an inert rock, which can be reused later as a construction material [19]. Plasma waste treatment also lead to reducing space operation, up to five times compared to usual combustion devices.

3.3. Nanoparticle synthesis

Thermal plasmas have high temperatures and strong temperature gradients, making them interesting to synthesize ultra-fine particles. A large range of elements can be used in this technique to synthesize nanoparticles, leading to ceramic powders based on carbides, nitrides, oxides or solid solution, and metallic powders in oxide or non-oxide forms [20]. Precursors can be fed into the plasma torch in the form of liquid, gases, or solids to be vaporized by the high temperature. The supersaturation of vapour species leads to the homogeneous nucleation of the nanoparticles, followed by the growth of these nanoparticles by condensation and/or coagulation [21]. The growth by condensation corresponds to an increase of the size of the particle by material passing from the vapour state to the liquid state. The coagulation is obtained by collision of the particles which stay strongly attached to each other to form a larger particle. The nucleation, condensation and coagulation phenomena are driven by the cooling rate of the plasma and the concentration of vapour in plasma [22].

One of the key point of the formation of nanoparticles by thermal plasma is the generation of the precursor vapour, which can become challenging with metals having high boiling point, such as iron or tungsten. The vaporization rate of metallic powders in the thermal plasma depends on several parameters, such as the size of the particles injected in the plasma jet to be vaporized, the residence time of these particles in the hot region, as well as the mass flow rate of material injected. Girshick *et al.* have set up conditions for iron powder feeding for obtaining iron nanoparticles, such as a size distribution of injected particles lower than 10 µm and a mass flow rate lower than 3.6 mg·s⁻¹ [23].

Carbon based nanoparticles can also be synthesized by thermal plasma, where a gaseous carbon precursor (methane, ethane, acetylene...) is decomposed and the carbon atoms grow into carbon black [24], graphene [25], or carbon nanotubes [26,27]. Details on the nucleation and growth of carbon nanoparticles are provided in Chapter 3, based on the modelling of the thermal plasma reactor used to grow the graphene nanoflakes developed by Pristavita *et al.* [6,28].

4. Plasma functionalization

Functionalization is the modification of a material surface by adding chemical functional groups in order to change its physical or chemical properties. The process of functionalization should not be mixed-up with doping, a term widely used in the literature for the chemical modification of graphene. Indeed, doping a material consists in adding impurities at small amounts in the bulk of the material to modify its properties while the functionalization is a phenomenon occurring at the surface of the material. Typical functionalities include atoms of carbon, oxygen, nitrogen, fluorine and others [29].

Plasma functionalization techniques are quite effective to incoporate functionalities on a sample surface. A precursor of the functionalities is generally injected in a plasma, generating a high amount of reactive species in the plasma afterglow which can directly react with the surface to be modified. Also, plasma techniques offer generally a better control on the type and level of functionalization compared to other methods, such as wet chemistry functionalization [30].

The most common properties aimed with plasma functionalization are the enhancement of surface hydrophobicity or hydrophilicity [31], improvement of the electrical conduction of the material [32], and modification of the electronic band gap of graphene [33]. For example, Hordy *et al.* described a process to introduce oxygen functionalities on the

surface of carbon nanotubes by a cold plasma process, resulting in hydrophilic carbon nanotubes [34].

Part II Carbon nanoparticles

This section aims to give an insight on the nature and synthesis techniques of some typical carbon structures [35], in order to better understand the interest of the graphene nanoflakes.

1. Graphite

Carbon is one of the most abundant elements in the universe, and on Earth. Its electronic configuration is $1s^2 2s^2 2p^2$. The hybridisation of the s and p orbitals into sp^2 and sp^3 configuration makes carbon able to have different allotropic forms. Graphite is one of the allotropic form of carbon which is abundantly found in nature.

Graphite is made of graphene sheets where carbon is sp2 hybrid and covalently bonded in hexagonal pattern whose structure and unit cell are represented in Figure 2-1. The graphene sheets are stacked by Van der Waals forces, and separated from each other by a distance of 0.334 nm. The particular structure of graphite results in anisotropic properties. Along the graphene planes, the electrons are free to move, providing a high electrical conductivity, which is much lower across the graphene planes. In the same way, thermal properties are highly anisotropic due to phonons which can easily propagate along the graphene planes but not across the planes [36].

Due to its specific properties, graphite is found in applications such as refractories, lubricants, pencils, and many others. Mostly produced from the mineral form, graphite can also be synthesized by different techniques. The main technique to produce synthetic graphite involves the high temperature processing of amorphous carbon precursor derived from petroleum coke, coal, or organic materials [37].

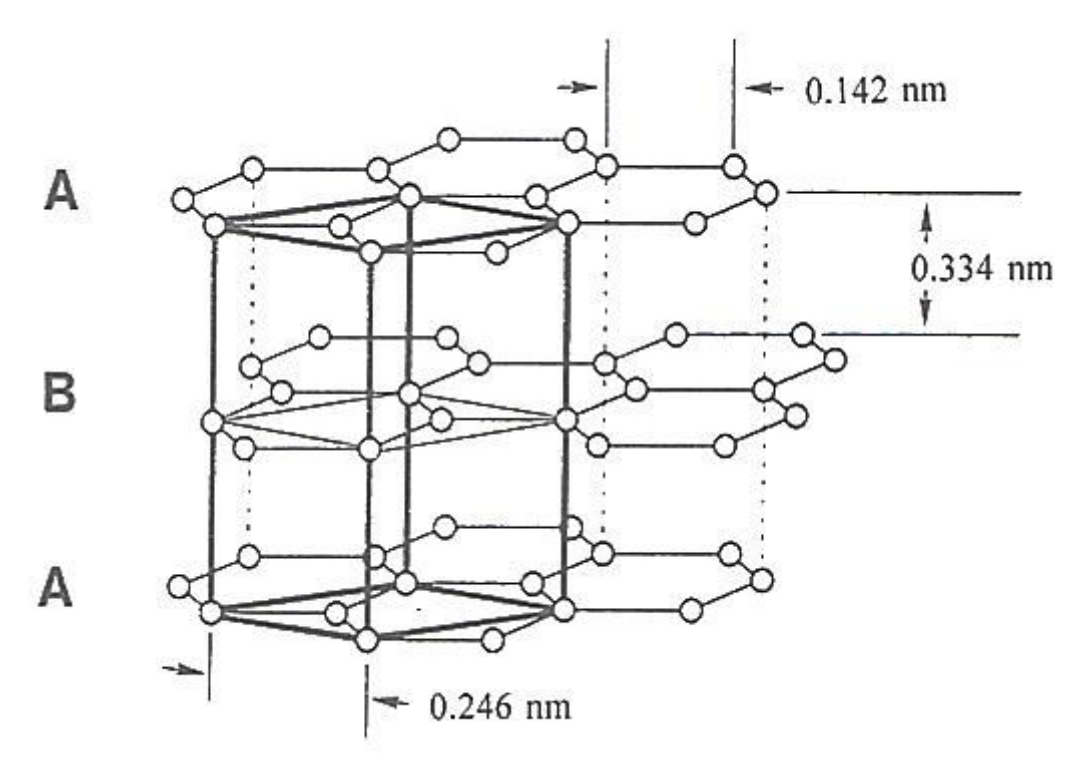


Figure 2-1: Representation of the hexagonal graphite structure, showing the unit cell [38].

2. Carbon black

Carbon black is a powder made of agglomerated nanoparticles and presenting a high surface area [39]. The nanoparticles composing carbon black can show numerous forms of structure, degenerated from graphite. Indeed, layers of graphene sheets are found in carbon black, but without the proper stacking characteristic from graphite. In carbon black, the layers can have more crystalline defects, and stacked in turbostratic structure, where the planes are tilted by an angle from each other (Figure 2-2), or even in lubricostratic structure, where the layers are randomly displaced. Amorphous carbon can also be found in carbon black in coexistence with the other structures [40].

Carbon black is mainly formed by using a carbon feedstock, consisting of heavy aromatic oils or natural gas which are pyrolyzed under controlled conditions of pressure and temperature in a furnace. The most common method to produce carbon black is the furnace

black process, where petroleum oil is injected in high-temperature gases for a partial combustion [41].

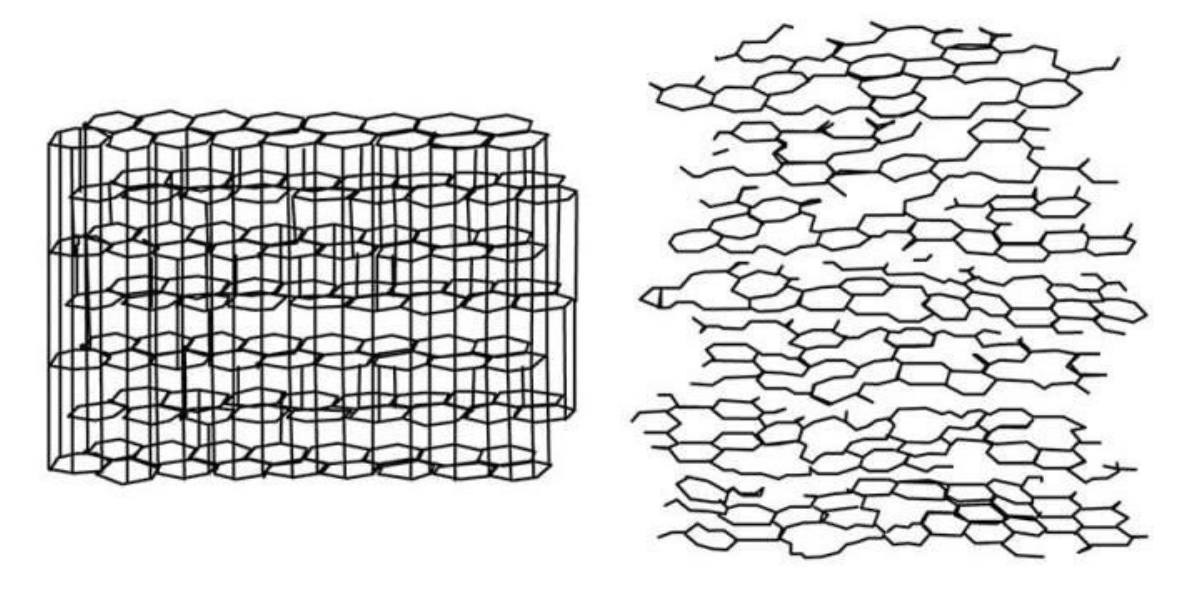


Figure 2-2: Turbostratic structure (right) compared to the perfect graphite structure (left) [42].

The properties of carbon black highly depend on their composition, amount of crystalline defects, and internal structure, and numerous types of carbon blacks have already been described [43]. In general, carbon black exhibits good electrical conductivity and a large surface area. Carbon black is used as a coloring agent in ink, paints or resins, but can also act as a conductive agent. The main application for carbon black is however their heavy use in tires, where it helps to increase the strength and durability of the rubber. Due to their high amount of defects, carbon black particles present a low resistance to corrosive environment [43].

3. Diamond

While graphite is exclusively made of carbon sp2, diamond is entirely composed of carbon sp3, in a variation of the face-centered cubic lattice, where the carbon atoms form tetrahedrons in the primitive cell, as seen in Figure 2-3. Diamond is naturally formed in deep

depth under the surface of Earth where high temperature and high pressure conditions prevail. Industrial processes can also produce synthetic diamonds. The process called high pressure high temperature reproduces the geological conditions of pressure and temperature to form diamond for industrial uses [44]. Another technique consists of the chemical vapor deposition (CVD) assisted by a thermal plasma of carbon feedstock in hydrogen atmosphere [45,46]. Reactive species of carbon are also produced together with a surplus of atomic hydrogen, using different techniques including RF plasma, microwave plasma, arc discharge and others [46–48]. In microelectronic applications particularly, diamond crystallites are often grown on a substrate especially chosen for its crystallographic orientation.

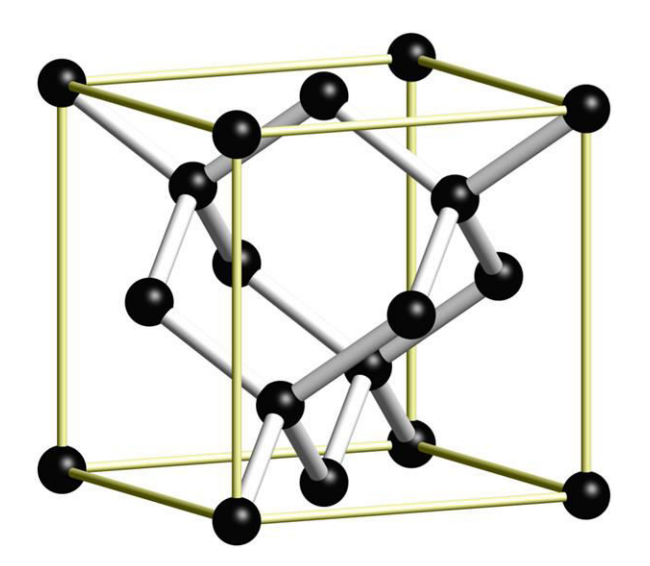


Figure 2-3: Representation of the diamond structure.

Natural and synthetic diamonds share properties including the highest hardness and thermal conductivity of any known material. Diamonds are also excellent electrical insulators and can become semi-conductors when doped with elements like boron or phosphorus [49]. Because of these properties, the use of synthetic diamonds is widespread in the industry for applications such as cutting tools, abrasive agents, heat sinks on electronical components, windows for transmitting infrared and microwaves radiations, and others.

4. Carbon nanotubes

Carbon nanotubes (CNTs) have a cylindrical structure, with carbon sp2 atoms forming a honeycomb structure. Carbon nanotubes can be found in single-wall or multi-walls structures, differentiated by the number of concentric tubes composing the nanotube, which is shown in Figure 2-4. Carbon nanotubes can reach lengths up to centimeters, for only tens to hundreds of nanometers in diameter. These nanoparticles, due to their carbon sp2 composition, exhibit the highest strength of any known material, and an excellent electrical conductivity. However, crystalline defects in the carbon nanotube structure affect their performance, lower than the theoretical values for a perfect carbon nanotube [50]. Carbon nanotubes are used in many applications including energy storage, sensors, electronics, and many others [51].

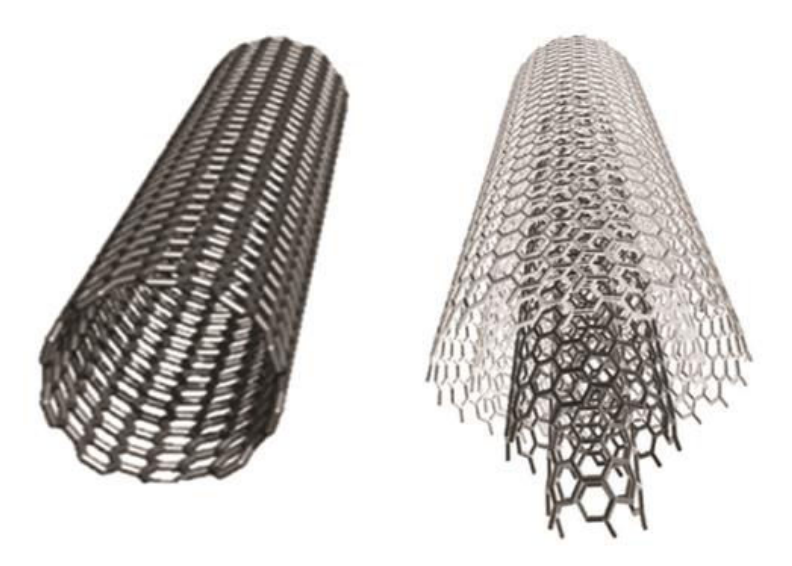


Figure 2-4: Representation of a single-wall (left) and multi-wall (right) carbon nanotube.

Many techniques exist to produce carbon nanotubes. One method to synthesize carbon nanotubes implies the laser vaporization of a graphite rod, where the samples are grown on a catalyst made of cobalt and nickel [52]. This technique leads to small yields, with some drawbacks, such as the need to remove of undesirable fullerenes, and the impossibility

to scale up the process. The laser ablation technique, however, can provide a very clean environment as well as single-walled carbon nanotubes (SWNTs) for the research along the use of these materials for microelectronic applications. The very first reported method to produce carbon nanotubes which was at the basis of their discovery and is still used in their production in industrial quantities was by thermal plasma arcing [53]. An electric current is applied between two carbonaceous electrodes typically containing some amount of catalyst material (most often Ni and Co) in an inert gas atmosphere. The anode is vaporized in the process, while the carbon nanotubes are either growing on the surface of the cathode, or in typical cases for large scale production, are found in the important "web structure" generated on the walls of the reactor. This web structure follows from the growth of metallic nanoparticles generated by catalyst material vapours quenched by the strong radial temperature gradients in the electric arcs. This technique in fact constitutes an early occurrence of the synthesis of nanoparticles in a thermal plasma environment. The idea of nucleating metallic nanoparticles, loading these with carbon and enabling the growth of nanotubes at lower temperatures was then further developed at McGill in a DC thermal plasma torch process by Harbec et al. [54,55]. The initial proof of concept used tungsten as the metal catalyst precursor, while the use of ferrocene to generate iron nanoparticles was used to shift the homogeneous nucleation of these iron nanoparticles in the downstream plasma jet of the DC torch, with a further downstream quench for the CNT growth on the iron nanoparticles [56]. The above studies showed that metallic nanoparticles smaller than roughly 30 nm needed to be generated to enable the CNT growth. These also enable the development of thermal plasma technologies and models for generating and tuning the growth of nanoparticles in the downstream jet of a thermal plasma. More recent techniques to generate CNTs include the chemical vapour deposition (CVD) of carbon over a bed of metallic catalyst nanoparticles most often generated by the thermal treatment of a very thin metallic

film [57]. Another CVD-based technique developed in the Plasma Processing Laboratory at McGill involved the growth of carbon nanotubes directly on the metallic surface (thereafter called the "direct growth method" in the literature). The use of mild acid treatment and/or heat treatment on stainless steel enabled this direct growth process, with acetylene acting as the carbon feedstock material in the thermal-CVD technique used [58–60].

5. Graphene and stacked-graphene

By definition, graphene corresponds to a single sheet of carbon sp2 forming an hexagonal pattern. In a way similar to the carbon nanotubes, the sp2 carbon configuration confers to graphene sheets outstanding strength and electrical conductivity. However, some major limitations prevent graphene from reaching widespread industrial applications. Indeed, graphene performance is related to its crystalline purity [61]. The techniques leading to the purest graphene sheets produce only a small amount of graphene, while the techniques producing industrial quantities of graphene result in samples having a lot of defects.

CVD is the technique leading to the purest sheets of graphene [62]. A carbon feedstock, such as methane is injected in a controlled atmosphere to be decomposed and adsorbed on a copper catalyst, where large defect-free graphene sheets can grow. Different methods exist to separate the graphene sheet from the copper catalyst. One of them consists of depositing a polymer layer on the graphene sheet, and then etching the copper catalyst on the other side [63]. This technique, by its low yield and numerous steps, cannot produce graphene in industrial quantities.

The technique used to produce large amounts of graphene is based on the reduction of graphene oxide [64]. Graphene oxide (GO) is obtained from graphite following a treatment with acid to incorporate oxygen functionalities in its structure and allow the sheets to be exfoliated in solution. Graphene oxide is then reduced by a heat treatment to remove the

oxygen functionalities from the sheets. The resulting product, called reduced graphene oxide (RGO), is not comparable to perfect graphene sheets. Indeed, the oxidation of graphite introduced a large amount of structural defects and the heat treatment does not allow a perfect recovery of the material [5]. Due to the defects in reduced graphene oxide, the theoretical values of strength and electrical conductivity cannot be reached in such products [65].

Graphene from CVD and reduction of graphene oxide techniques are usually found under the form of sheets stacked together because of the difficulty to synthesize single graphene sheets [66]. Stacked graphene can be considered between graphene and graphite for its properties. Some techniques describe the production of large quantities of stacked graphene showing good crystallinity [67].

In this context, graphene nanoflakes produced in the Plasma Processing Laboratory following the original procedure of Pristavita *et al.* exhibit high crystallinity based on a technique which can be scaled up [6]. The production of GNFs is based on the injection of methane in an argon thermal plasma. The molecules of methane are decomposed into carbon and hydrogen atoms under the high temperature. Cooling down the argon plasma leads to the homogeneous nucleation and growth of the nanoparticles. Detailed information on the formation of the GNFs in the thermal plasma reactor is given in Chapter 3. It can be noted that the GNFs do not need any catalyst to be grown, the process being based on homogeneous nucleation. Also, the GNFs synthesis is made in one single batch process contrary to graphene made by CVD or reduction of graphene oxide which require numerous steps before obtaining the final product.

Part III Applications for the functionalized nanoparticles

In this thesis, the target application for functionalized graphene nanoflakes aim the energy and transportation sectors, more particularly fuel cells. Two aspects are being studied, both being strongly related to the ability to modify the graphene structure with functional groups. The first relate to two methods for generating new low cost catalysts in replacement to platinum for the oxygen reduction reaction (Chapters 4 and 5). The second relates to our ability to generate an optimized dispersion of the graphene powders during fabrication of a fuel cell membrane through the generation of a stable nanofluid (Chapter 6). This section provides some background on these different applications.

1. Alkaline Fuel cells

Fuel cells are devices converting chemical energy into electricity and heat by the reaction between hydrogen and an oxidizing agent. In contrast to a battery, a fuel cell can work as long as fuel is provided. Although all fuel cells work on the same principle, different types of fuel cells exist, varying mostly by the type of electrolyte used. Typically, hydrogen is dissociated at the anode, and the protons are drawn through the electrolyte to the cathode. Electrons generate a direct electric current between the anode and the cathode through a circuit external to the fuel cell stack. At the cathode, the oxidizing agent, which is generally oxygen, is reduced by the protons to produce water. A catalyst is needed at the anode and cathode for the electrochemical reactions.

1.1. Fuel cell types

The different types of fuel cells are mostly distinguished by their electrolyte, and regrouped under the following types: phosphoric acid fuel cells, molten carbonate fuel cells, solid oxide fuel cells, polymer electrolyte membrane fuel cells, and alkaline fuel cells [68].

Phosphoric acid fuel cells (PAFCs) have concentrated phosphoric acid contained in a silicon carbide matrix as an electrolyte. PAFCs require temperature between 150°C and 220°C to be fully operational, and can reach up to 40% in electricity power generation efficiency [69]. The catalyst for both anode and cathode is a platinum based catalyst. This type of fuel cell has different disadvantages, such as the catalyst being degraded at the cathode, due to the highly corrosive environment. Other problems can also occur such as electrolyte migration, cell contamination and material corrosion. The catalyst can also be poisoned by carbon monoxide and dioxide, lowering the overall performance of the fuel cell [70].

Molten carbonate fuel cells (MCFCs) use molten carbonate salts in suspension in a ceramic matrix of alumina. MCFCs require high temperature between 600°C and 700°C to operate [71]. These high temperature of operation allow fuels to be converted into hydrogen inside the fuel cell, contrary to fuel cells operating at lower temperature and where hydrogen has to be produced prior being fed in the fuel cell. The high temperatures also allow non-noble metal catalysts to be used, such as nickel oxide, making MCFCs resistant to catalyst poisoning. However, MCFCs show major disadvantages due to the high corrosivity of their electrolyte, which dissolves relatively easily the catalyst [71]. Also, MCFCs display issues with high pressure and high temperature management.

Solid oxide fuel cells (SOFCs) have a solid oxide, or ceramic, as an electrolyte. Instead of conducting protons through the electrolyte to the cathode, it is the negative oxygen ions which travel through the electrolyte to the anode, to react with hydrogen or carbon monoxide. In order to allow the ion conductivity, SOFCs have to work at high temperatures, between 800°C and 1000°C [72]. In the same way as MCFCs, no platinum catalysts are required due to the high temperature of operation, making SOFCs resistant to carbon monoxide poisoning also. SOFCs typically have problems with durability due to the

exposition of the different materials to high temperatures [72]. Because of the high temperature of operation, SOFCs are not really suitable for the transportation sector but are rather aiming for stationary medium power generation.

Polymer electrolyte membrane fuel cells (PEMFCs) have a polymer membrane as an electrolyte which is insulating to electrons but conductive to protons. The polymer is generally a perfluorosulfonated acid polymer, NafionTM. The operating temperature of PEMFCs is one of the lower among fuel cells, and is between 60°C and 80°C [73]. At this temperature, a catalyst is needed at the anode and cathode, and is generally a platinum based catalyst, meaning the catalyst can be poisoned by carbon monoxide.

Alkaline fuel cells (AFCs) use potassium or sodium hydroxide as an electrolyte. The solution is contained in an asbestos matrix. AFCs can work at high temperature, around 250°C, where the electrolyte solution has to be highly concentrated (~85%), or more typically at temperatures lower than 120°C with electrolytes having also lower concentrations (~50%) [74]. At these temperatures a catalyst is required at the anode and the cathode. The oxygen reduction reaction is more favourable in alkaline electrolyte rather than an acid electrolyte, resulting in a larger range of catalysts which can be used, including platinum based catalyst, metal oxide, non-metal catalysts. The alkaline electrolyte being less corrosive than acidic electrolyte, AFCs have less issues with catalyst degradation. AFCs exhibit the highest efficiency among the other fuel cells, due to a higher voltage obtained at similar current densities.

1.2. Oxygen reduction reaction in AFCs

The oxygen reduction reaction (ORR) occurs at the cathode and generally requires a higher catalyst loading rather than the anode, where the hydrogen oxidation reaction occurs [75]. The oxygen can be transformed into hydroxide ions into a direct 4-electron pathway, or

through a 2-electron pathway where peroxide ions are an intermediate. The half-reactions of the ORR for the 4 and 2-electron pathways are the following:

$$O_2 + 2H_2O + 4e^- \leftrightarrow 4OH^- E^0 = 0.401 \ V \ vs \ SHE$$

$$O_2 + H_2O + 2e^- \leftrightarrow HO_2^- + OH^- E^0 = -0.076 \ V \ vs \ SHE$$

$$HO_2^- + H_2O + 2e^- \leftrightarrow +3OH^- E^0 = 0.878 \ V \ vs \ SHE$$

where SHE designates the Standard Hydrogen Electrode.

The 4-electron pathway is preferred compared to the 2-electron pathway. Indeed, the peroxide ion can be relatively stable, and stop the reaction, limiting the performance of the fuel cell [75].

The kinetics of the ORR reaction is faster in alkaline electrolyte than in acidic electrolyte, allowing the AFCs to potentially reach higher efficiencies (~50 to 70%) than the other fuel cells [76].

1.3. Platinum catalyst for the ORR

Platinum based catalysts offer the highest catalytic activity to reduce oxygen. The catalysis of oxygen on a platinum surface involves a multi-electron process with numerous elementary steps and reaction intermediates. However, the mechanism of the ORR on platinum is still not completely understood. Different mechanisms have already been proposed, including associative and dissociative mechanism [75]. In the dissociative mechanism, the oxygen molecule is dissociated into oxygen atoms on the surface of platinum before reacting with electrons and protons, or hydroxyl ions in the case of an alkaline electrolyte. In the associative mechanism, the oxygen molecule is adsorbed on the surface of the platinum catalyst, and the oxygen bond is broken during the successive reactions with the

electrons and protons or hydroxyl ions [75]. It can be noted that no hydrogen peroxide is generated in these proposed mechanisms.

Platinum is a noble, rare and expensive metal, varying between 900 and 1700 USD/oz during the last five years. At this price, more than 1000 US\$ of platinum would be needed for a fuel cell in automotive application. Extensive research has been done to reduce the amount of platinum loading in the catalyst in order to reduce the price for the same, if not higher, catalytic activity. In order to achieve this reduction, platinum nanoparticles are generally dispersed on activated carbon. The surface area of platinum increases when the size of the nanoparticles is decreased, offering potentially additional catalytic sites for the ORR to occur.

Despite its price, platinum catalysts can be poisoned by different products, inhibiting its catalytic activity. As seen previously, carbon monoxide is a common poison for platinum catalysts. Indeed, carbon monoxide, even in small traces down to 30 ppm, can be adsorbed on the platinum surface and block access of catalytic sites to the oxygen molecules [77]. Other poisons can alter platinum by covalent bonding on its surface, including molecules such as amines, sulfides, thiols and other metals.

1.4. Alternatives of platinum catalysts

Alternatives of platinum are studied to provide cheaper and more durable catalysts. These catalysts can be differentiated into non-noble metal catalysts, where the metal is under the form of oxide or in atomic dispersion, and non-metal catalysts, where the properties of doped graphene are used instead of metal.

Wu and al. described a catalyst made of iron (II,III) oxide (Fe₃O₄) dispersed on an aerogel of nitrogen doped graphene [78]. This non-noble metal catalyst showed a better durability than commercial platinum based catalyst. The catalyst results from the mixture of

graphene oxide, iron salts, and polypyrrole in solution which was heated and then dehydrated. Another study also described the same behaviour with cobalt (II,III) oxide nanoparticles on nitrogen doped graphene [79]. Different metal oxide are also good candidates for the oxygen reduction reaction in alkaline electrolyte, including titanium dioxide, vanadium oxide, perovskite-type oxide, and other.

The atomic dispersion of non-noble metal on a carbon matrix surface has drawn a lot of attention for generating non-noble metal catalysts for the oxygen reduction reaction. It started when Jasinski showed that iron and cobalt phthalocyanine molecules had a strong electrocatalytic activity for the ORR [80]. A metal phthalocyanine is a cyclic molecule where four pyrrolic nitrogen atoms are bonded to the metal in the centre, in a way similar to the porphyrin organic ring structure in hemoglobin. However, these molecules are not durable due to the corrosivity of the acidic or basic electrolyte. The idea to overcome this issue was to incorporate iron in catalytic sites mimicking the structure of the phthalocyanine on the surface of a corrosive resistant carbon based matrix [81], a possible catalytic site being represented on Figure 2-5.

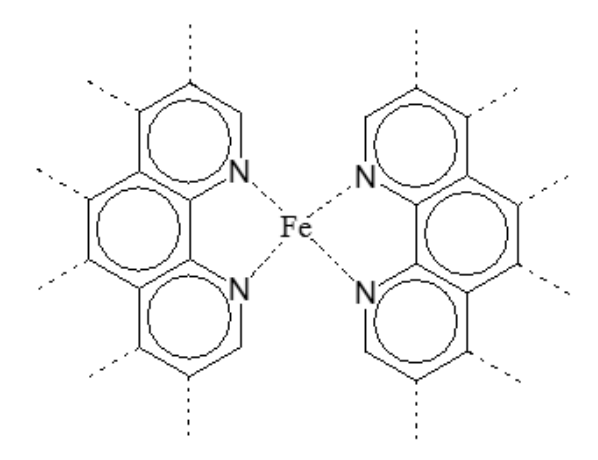


Figure 2-5: Structure of a possible catalytic site, inspired by [82].

Graphene naturally became one of the best candidate for supporting catalytic sites due to its outstanding properties. Numerous studies described methods to produce these iron

or cobalt based catalysts. Two major trends can be observed in the way to produce such catalyst. The first method implies to directly attach phthalocyanine molecules to graphene through pyrolysis [81], while the second method consists in building the catalytic sites with nitrogen doped graphene and various metal salts under a pyrolysis step. In this context, Dodelet's research group obtained interesting results on catalysts prepared based on the pyrolysis of iron acetate in the pores of carbon black, with current densities going up to 0.75 A.cm⁻² over 100-hour experiments [82]. Additionally, Kramm *et al.* calculated possible structures of active catalytic sites which could be incorporated on graphitic samples, and shown in Figure 2-6.

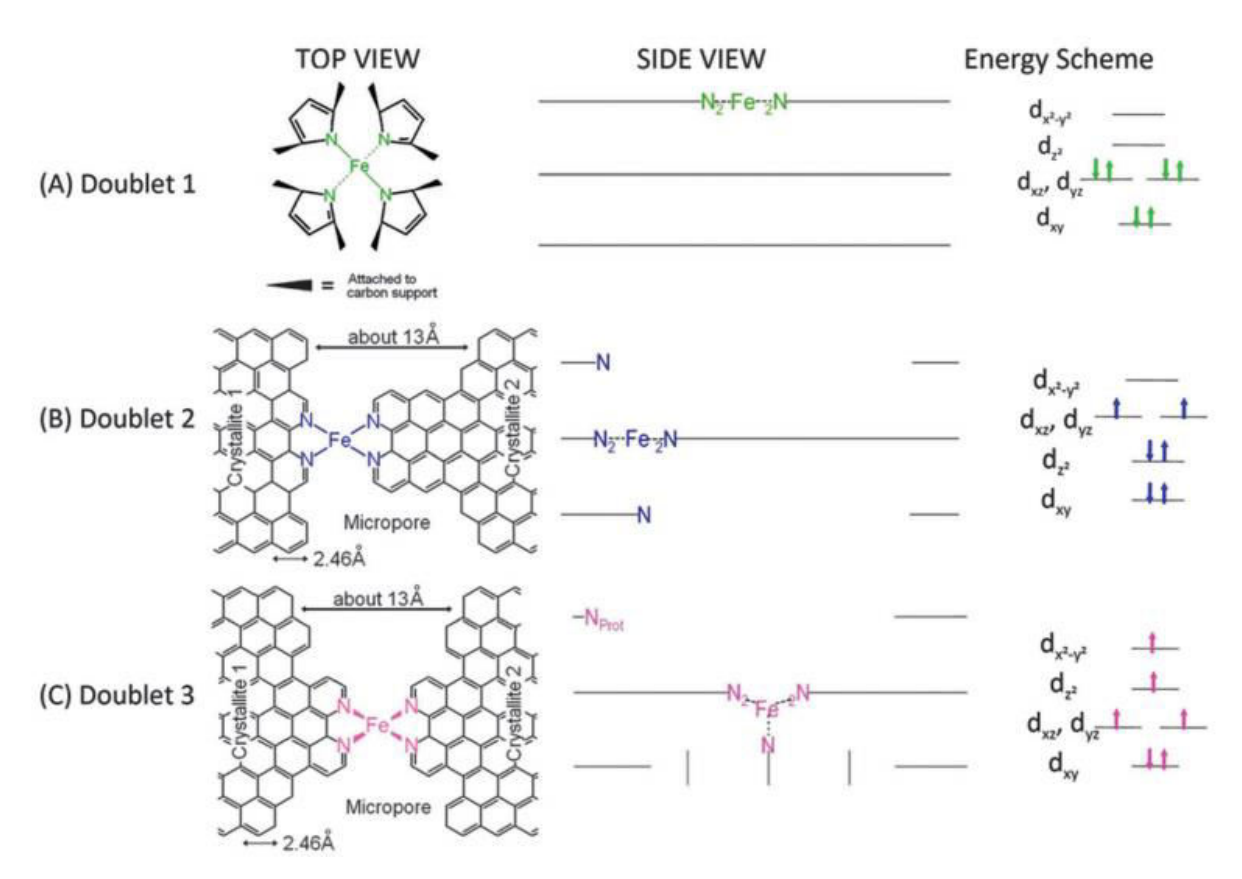


Figure 2-6: Possible structures of iron-based catalyst sites incorporated in graphene sheets proposed by Kramm *et al.* [83]. For each catalytic site, a top and side view is given, as well as the energy scheme and filling of the orbitals for the iron (II) ion. The three cases A, B and C are extracted from doublets obtained in a Mössbauer analysis.

The proposed structure for the catalytic sites in Figure 2-6 includes the phthalocyanine structure where the iron ion is contained around four nitrogen atoms in a same plane, but also new structures, where nitrogen atoms situated out of the phthalocyanine-structure plane could also contain the iron ion [83]. These structures could be found on the edges between two graphitic structures, but also in the defects on such graphitic structure [82]. Kramm *et al.* indicate that level d_{Z2} is compatible with the ORR, however only the (A) and (C) configurations are not saturated and seem to have empty sites that could be active. At this point, the exact structure of active catalytic sites is still debated. When studying a large number of carbon black structures, Dodelet's research group also proved that the level of crystallinity of the carbon structure supporting the catalytic sites had a direct impact on the electrocatalytic activity of these catalysts, the highest electrocatalytic activities being found for the samples exhibiting the highest crystallinity [84]. The level of crystallinity of the carbon black particles was found to be very important for the time stability of the catalyst produced.

Recently, non-metal catalysts for the ORR have been developed based on the addition of atoms on graphene. The atoms chosen for these catalysts are nitrogen, sulphur, phosphorus, boron, or combination of them [85–88]. The catalytic sites are directly due to the addition of functional groups on graphene surface. Studies also proposed that the addition of the atoms in the graphene structure locally changed the electronic charges distribution on the surface of the graphene and created catalytic sites [89].

2. Nanofluids

Nanofluids are, by definition, a stable dispersion of nanoparticles in a base fluid.

Many combinations of nanoparticles and fluids can be used to produce nanofluids. The

nanoparticles can be metals, metal oxide, polymer, quantum dots, carbon based nanoparticles, while common fluids include water, oils, ethylene glycol, and others [90].

Research on nanofluids has first generated a large interest because of the possible enhancement of the heat transfer coefficient from the nanoparticles. A large range of applications related to heat transfer were thus studied using nanofluids such as electronic, automotive, and nuclear cooling systems, solar absorption, and many others. Due to a lack of reproducibility in the enhancement of the heat transfer coefficient of nanofluids [91], research in these applications decreased in favor of other nanofluids properties. Indeed, nanofluids can be used as lubricants, the nanoparticles helping in the friction reduction, in magnetic sealing application with ferromagnetic fluids, in biomedical applications for their antibacterial activities or drug-delivery properties [92]. Contrary to heat transfer, mass transfer enhancement was found to be important and possible new applications should result in this field. Another important property particularly for carbon-based nanofluids is the strong radiation flux absorption from the particles within the bulk fluids [34]. This has generated a large interest in the passive solar energy sector [93] and in biomedical field for laser-based local treatment [94].

Generation of nanofluids can be done following two methods. The two step-methods involves the initial formation of the nanoparticles under the form of a dry powder, followed by their dispersion in a liquid. In order to break the interaction between the particles, different techniques can be employed, including mechanical agitation, ultrasonication, ball milling, high-shear mixing. Because of the large specific surface area of nanoparticles, agglomeration occurs easily in nanofluids. The one-step method tries to avoid agglomeration by synthesizing the nanoparticles and dispersing them in the base fluid in the same step. Various techniques can be used to achieve nanofluids with the one-step-method. These techniques include the physical vapour condensation of metal nanoparticles which are directly collected

in the fluid, reduction of metallic salts in solution under microwave irradiation, or phase-transfer method [95]. Even if the nanofluid stability is improved in the one-step method, this stability does not remain long enough to meet most industrial use criteria.

The stability of nanofluids can be improved by the addition of surfactants in the suspension. Surfactants are molecules which modify the surface tension between two surfaces. These molecules, once dispersed in the nanofluid, cover the surface of the nanoparticles and prevent their agglomeration. In most of the applications targeted by the nanofluids, the surfactants represent a disadvantage. For example, the temperature reached in heat transfer or radiation absorption applications can readily cause the degradation of the surfactant molecules, leading to the agglomeration of the nanoparticles on top of the added impurity in the fluid. Thus, the modification of the surface properties of nanoparticles by functionalization has a high importance in the field of nanofluids.

Chapter 3 EXPERIMENTAL EQUIPMENT AND MATERIAL

CHARACTERIZATION

Part I Thermal plasma reactor

This section aims to describe the experimental set-up used to synthesize and functionalize the graphene nanoflakes. The set-up consists in an all-in-one TEKNA Thermal Plasma System unit [96] presented on Figure 3-1.



Figure 3-1: Picture of the experimental set-up. (A) control console (B) RF generator (C) ICP torch in the Faraday cage (D) conical reactor (E) exhaust connected to the vacuum pump.

1. RF Generator

A radiofrequency (RF) Lepel generator is used to provide up to 60 kW of power. In this project, a TEKNA PL-35 ICP torch is used at a typical power between 20 and 25 kW. The frequency of the RF signal is comprised between 2 and 5 MHz. In the generator, an

oscillator tube transforms a DC signal into the RF signal. A variable grid coil controls the total current flow in the oscillator circuit. The RF signal is then sent to the plasma torch, in order to generate and sustain the plasma.

2. ICP torch

An inductively coupled plasma (ICP) torch is used, and represented in Figure 3-2. It consists in a water-cooled induction coil in which the RF signal is passed. The time-varying electrical field passing in the coil induces a time-varying magnetic field at the centre of the cylindrical coil. The plasma is generated by injecting argon gas in the central volume of the torch, where the magnetic field creates an electric field in the gas, leading to its ionization. The argon thermal plasma is generally ignited at a pressure lower than atmospheric pressure, typically at 13.8 kPa, before being maintained at the desired pressure. The generated argon plasma generally exits the ICP torch at a temperature in a range around 10,000 K, such temperature corresponding roughly to the low ionization equilibrium and necessary electrical conductivity needed to sustain the discharge in this thermal plasma [97]. The efficiency of an ICP torch for coupling the RF power into the plasma is generally close to 50%, the remaining being evacuated mainly in the form of heat. For this reason, as well as controlling the temperature in the torch body, the coil has to be water cooled. The ICP torch is placed in a Faraday cage to minimize the radiated RF emission to avoid the perturbation of other electronic devices as well as the safety for operators.

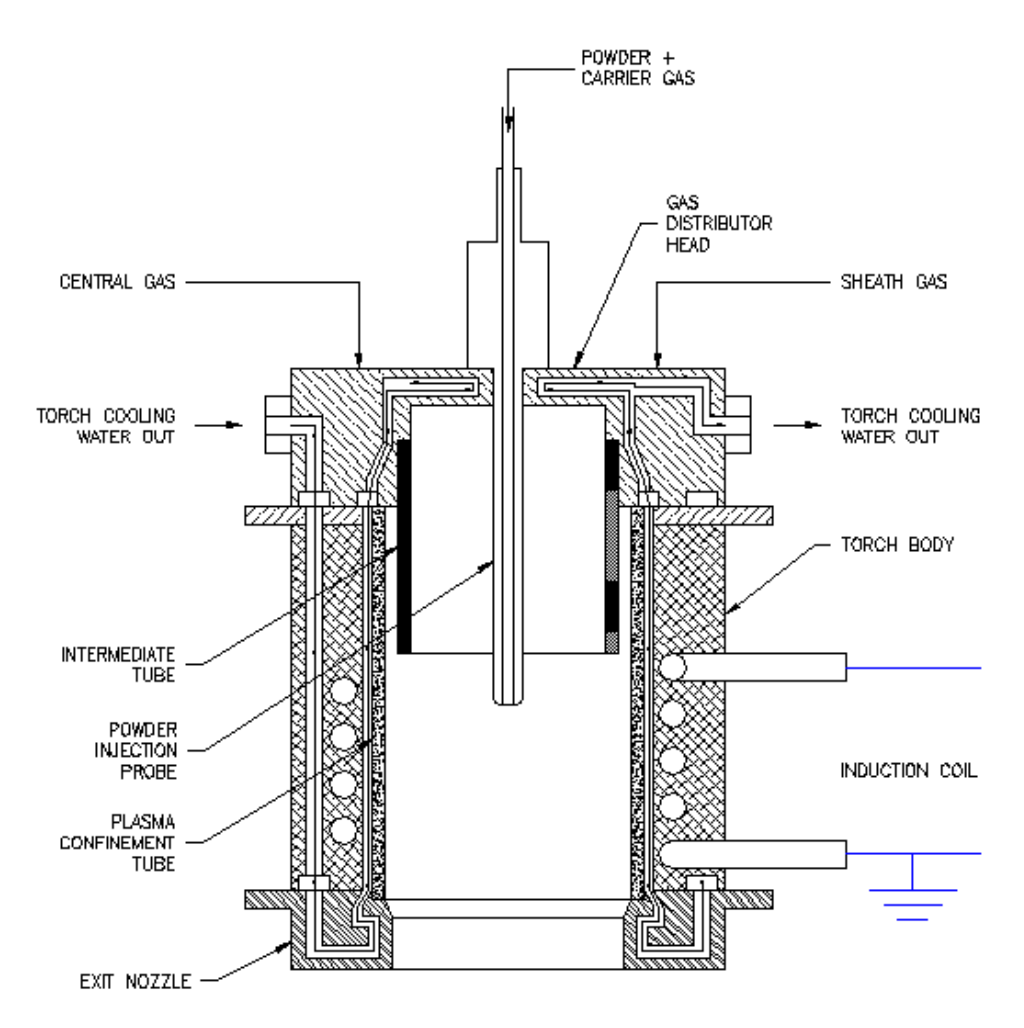


Figure 3-2: Schematic of an ICP torch (©TEKNA).

Argon gas comes from three distinct inlets to the ICP torch. The sheath gas is there to isolate the plasma from the walls and also provides cooling of the torch body. This sheath gas is injected between the plasma confinement tube and the intermediate tube of the torch (Figure 3-2). The central gas is the gas which composes the core of the plasma, it is injected within the intermediate tube of the torch. The sheath flow is generally larger than the central gas flow in order to confine the plasma. Finally, the central probe gas can be injected at various heights in the ICP torch and can act as a carrier gas for powders and liquids precursors. The probe gas is argon, but can also contain gaseous precursors to be decomposed directly in the ICP torch. The probe is used to inject carbon and nitrogen precursors during

the GNFs growth. The usual argon flow rates conditions to get a stable plasma are 45 slpm for the sheath gas, 13 slpm for the central gas and 4.5 slpm for the probe gas.

3. Water cooling system

Different parts of the plasma system have to be cooled down to avoid overheating and damages. It is the case of some parts in the RF generator (oscillator tube, capacitors and coils), the ICP torch, the plasma reactor walls and bottom plate, and the injection probe. Each water circuit is separated from each other. A water reservoir is contained in the TEKNA system, and filled with city water. This reservoir provides the water necessary to cool down the ICP torch, the reactor and the injection probe. Typically, water flow rates of 7, 25, and 34 slpm for respectively the injection probe, ICP torch and reactor are used for an optimal operation. The water is recirculated in the different circuits but is first cooled down with a heat exchanger. Using a separate cooling system, the RF generator needs around 85 slpm of water to cool down its different parts, which is also provided by the city water.

4. Vacuum system

The pressure in the thermal plasma reactor is controlled by a water ring vacuum pump. The pump is fed with approximately 35 slpm of water. The generation of the vacuum in the pump is based on the creation of a water ring under centrifugal force by a multi-blade impeller positioned eccentrically. The pressure inside the reactor chamber is partially controlled with a valve imposing the percentage of pumping in the reactor. Apart from this manual control, an electronic control allows to reach precise values of pressure inside the reactor chamber. This vacuum pump enables to reach a base pressure of 13 kPa, which corresponds to the pressure used to ignite the plasma.

5. Conical reactor

The reactor used to grow the GNFs has been designed in a specific conical geometry, with a total opening angle of 14°. The reactor is made of water-cooled stainless steel walls and bottom plate. The specific geometry has been studied through Computational Fluid Dynamics by Mendoza-Gonzalez *et al.* [28], and represented in Figure 3-3. It indicates that the plasma is generated at 10,600 K in the ICP torch and then cooled down to 300 K close to the water-cooled walls and a bottom plate. The plasma jet follows a laminar flow as indicated by the streamlines which do not yield turbulence and recirculation in the core of the reactor. It is also to be noted that the design of the reactor is totally axisymmetric and hence follows well the modelled flow pattern. Gas exit and pumping is made through the annular manifold in the bottom outside section of the reactor. This generates azimuthal symmetry and a stagnation-point radial exit flow geometry. Experimental evaluations of the particles generated in the reactor by Pristavita clearly confirmed this radial flow pattern from particle deposits observed [98].

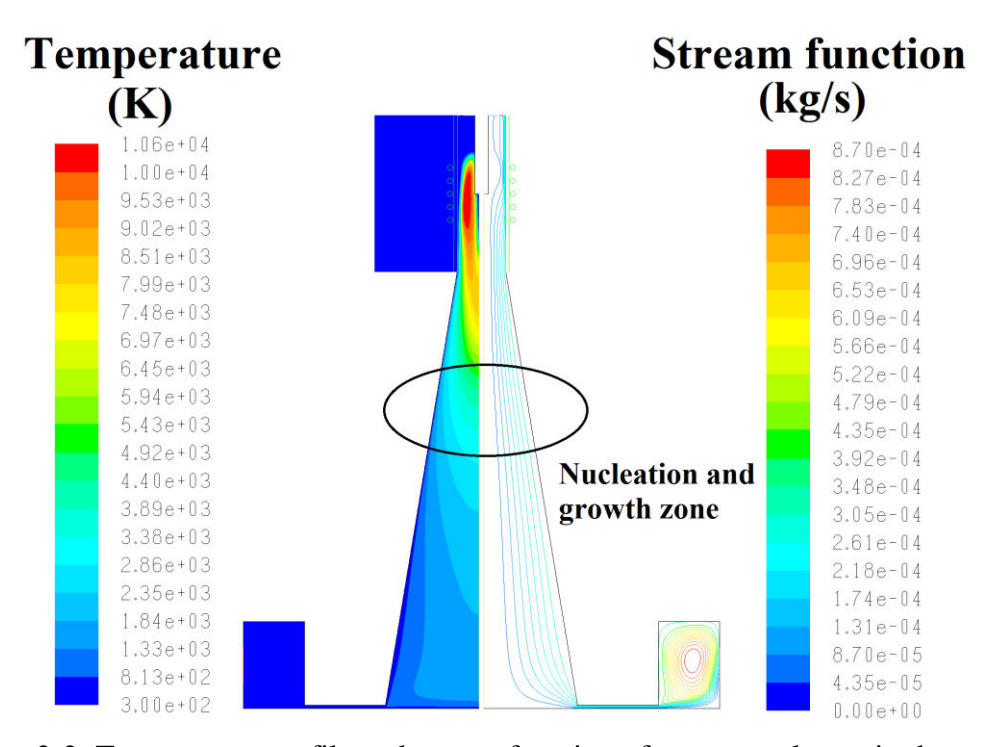


Figure 3-3: Temperature profile and stream function of an argon plasma in the conical reactor.

The study of the reactor through CFD gave insight of the phenomena occurring during the formation of the GNFs. It appears that the specific geometry and the absence of gas recirculation in the reactor promotes the growth of nanoparticles after the in-flight homogeneous nucleation, without any coagulation effects [28]. The coagulation effects generally happen when the forming particles collide with each other. In this reactor, this phenomenon cannot occur due to a diluted system, and the geometry expansion eliminating recirculation zones and uncontrolled thermal history of particle growth. The absence of gas recirculation is consequently related with the elimination of amorphous carbon and the high crystallinity of the resulting GNFs. The high crystallinity is in fact the result of much larger residence times in the homogeneous nucleation domain located well downstream within the reactor (Figure 3-4) compared to a sudden reactor expansion occurring at the exit of the nozzle. Modelling of this last case effectively showed the nucleation zone of carbon nanoparticles to occur in the high velocity and strong axial temperature gradient flow very close to the nozzle exit [98]. This being said, it can also be noted that the nucleation and growth of the nanoparticles in the conical reactor occur in a short window of temperatures, between 3,700 and 4,900 K, for a relatively short residence time estimated at a few milliseconds [28]. Thus, the GNFs exhibit a narrow particle size distribution. The absence of gas recirculation or turbulences makes the system really robust in terms of reproducibility between the different batches of functionalized and non-functionalized GNFs [98,99].

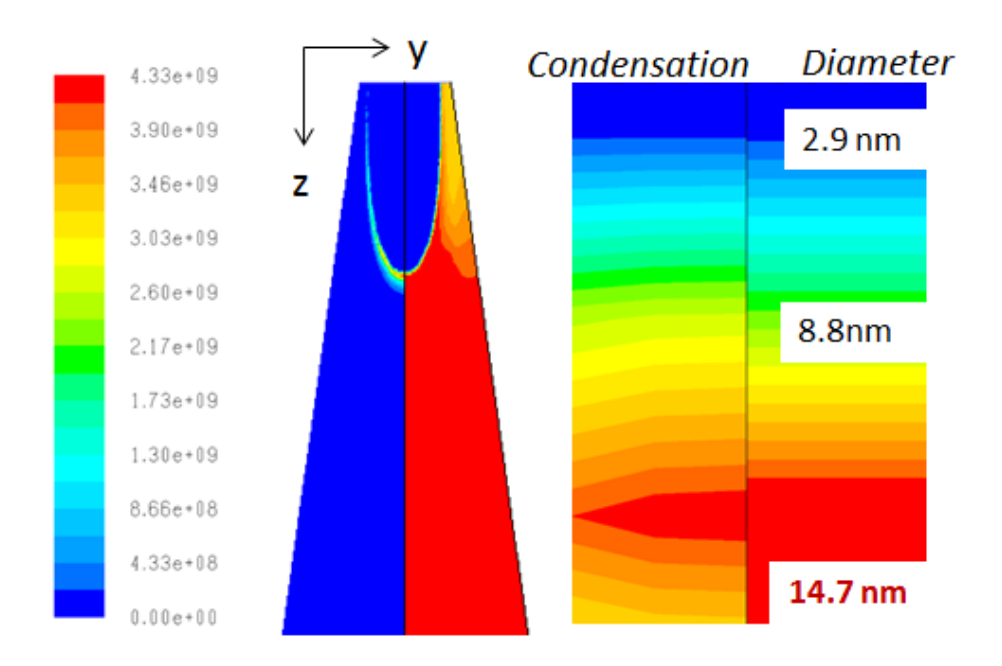


Figure 3-4: (Left) Mapping of the condensation coefficient for the GNFs in the argon thermal plasma. (Right) Zoom-in on the nucleation and growth region on the central axis [28].

6. Precursor and main gas feeding techniques

6.1. Gas feeding

Gas feeding in the thermal plasma can be separated in two parts. The first one being the main gas to generate the plasma, the second part being the different gaseous precursors fed to the reactor.

The main gas is generally argon (can also be nitrogen) which is stocked in liquefied gas tanks. These tanks have a capacity of 230 L of liquefied gas, equivalent to 194 m³ of gas in the case of argon. The argon tank provides a flow rate of 62.5 slpm of argon gas in the ICP torch, through the sheath, central and probe inlets.

Other gases can be injected to the reactor. In this thesis, the gases which have been used are methane, nitrogen and air. Gas cylinders are used for these gases, and the flow rates are controlled by mass flow controllers. A flash arrestor is added to the methane line by

precaution. All of these gases are fed directly to the injection probe in the ICP torch. Methane is used as a carbon precursor to grow the GNFs, while oxygen from air and nitrogen gases are used in different functionalization steps.

6.2. Liquid precursors

Liquids precursors can be injected in the thermal plasma reactor through the injection probe or by a viewport located on the reactor walls, 9 cm below the exit of the ICP torch nozzle. The liquid is fed by a stainless steel syringe (Chemyx 20 mL) where the liquid flow rate is controlled by an electronic push-syringe (Nexus 3000). The liquid injection system is shown in Figure 3-5. The liquid is then injected in the reactor with the help of a carrier gas.



Figure 3-5: The liquid injection system based on a stainless steel syringe and a push-syringe.

Different types of liquids are fed in the reactor. Iron salts and iron (II) phthalocyanine dispersed in water act as iron precursors for the functionalization of the GNFs. Carbon disulphide is used as a sulphur precursor to functionalize the GNFs.

6.3. Solid precursors

Solid precursors under the form of powders can also be injected in the thermal plasma reactor. In the same way as the liquid precursors, powders can be fed through the injection probe to be directly in contact of the plasma generated in the ICP torch, or through

the side viewport of the reactor. However, iron powders which are used in the functionalization of the GNFs have a tendency to agglomerate inside the injection probe under electrostatic effect. Injection through the side viewport is thus preferred.

A powder feeder PFV100-VM-NO from TEKNA is employed here and shown in Figure 3-6. The powder feeder is based on a vibrating bowl, whose vibration frequency is tuned for the powder nature, and the intensity of the vibration controls the mass flow rate of delivered powder.



Figure 3-6: The powder feeder.

Part II Characterization techniques

This section provides a background of the different characterization techniques used in this thesis. The specific use of these techniques for the functionalized graphene nanoflakes is briefly mentioned and is more detailed in the following chapters.

1. Scanning electron microscopy

Scanning electron microscopy (SEM) is based on the interaction between electrons and a sample surface to create a picture of the surface, with a resolution down to a few nanometers for the best microscopes. A SEM is generally composed of an electron column, where a vacuum of approximately 10⁻⁶ kPa is generated, a scanning system and detectors. The electron beam has energies in the range 1 to 40 keV and is generated by an electron gun having a tungsten filament cathode. The electron beam is then focused by electromagnetic lenses to create a small electron probe having a spot size lower than 10 nm on the surface of the sample to study. The electron beam passes through a pair of scanning coils, deviating the electrons in the x and y directions, making the electron probe scanning the studied area of the sample surface. The magnification is controlled by the voltage supplied to the scanning coils, and not the objective lens power.

The main electron beam interacts with the sample surface by emitting secondary electrons, backscattered electrons, and characteristic x-rays from the atoms of the surface. The secondary atoms are the ones whose detection lead to the formation of the picture. Secondary electrons are generated by the ionization of atoms after elastic collision with primary electrons from the probe. The secondary electrons are generated in the first micrometer of the sample surface. Due to their low energy (< 50 eV) most of the secondary

electrons are re-absorbed in the bulk of the sample, while only secondary electrons coming from the first nanometers of the sample surface can be detected.

The secondary electrons are accelerated through a typical potential of +400 V to attract them to the detector. The intensity of the secondary electrons is measured after being enhanced by a scintillator and a photomultiplier. The picture is created by the two-dimensional intensity distribution of the signal at the exit of the photomultiplier. The topographic contrast is obtained because "hollows" and "peaks" at the surface of the sample are not releasing the same quantity of secondary electrons. Electrons generated in "hollows" have higher chances to be re-absorbed by the sample around, releasing less secondary electrons to the detector, and leading to a darker area.

Some precautions have to be taken when selecting a sample to be analysed by SEM. First, the surface of the sample has to be conductive to avoid any charging effect. If not conductive, a sample can be covered with a few nanometres of gold or chromium. Also, a sample has to support the high vacuum of the electron column, eliminating biological samples, and more generally samples containing water. Powders have to be degassed prior to the SEM analysis in order to not modify the vacuum environment of the chamber.

SEM allows to get an overall view of the GNFs and information about the homogeneity of the sample. The presence of any characteristic material such as amorphous carbon, or polymers can be determined by SEM.

2. Transmission electron microscopy

Transmission electron microscopy (TEM) is similar to SEM in the use of an electron probe interacting with a sample surface. However, transmitted electrons are detected in this microscopy technique instead of secondary electrons. In order to detect transmitted electrons, the sample has to be thin enough, with at most hundreds of nanometers thick. The contrast in

TEM is created by the difference of thickness of the sample, where thicker areas lead to darker spots. The resolution of TEM can go down to distinguish atoms or line of atoms from each other. In order to improve the mean free path of the electrons, the pressure in TEM is lower than in SEM, with a vacuum of around 10^{-7} to 10^{-9} kPa.

In the case of crystalline samples, the diffraction pattern can be observed by adjusting the electromagnetic lenses. For monocrystalline samples, a pattern of dots is obtained while concentric rings appear for polycrystalline samples. The distance from the centre to the dots or the rings can be used to identify the crystalline structure of the sample.

On top of being thin enough, samples for TEM have to support a high vacuum, and also need a conductive surface to avoid any charging effect. The sample is generally mounted on a small copper grid containing an ultra-thin carbon film on its surface.

TEM allows a closer view of the GNFs compared to SEM. Thus, the number of graphitic planes can be elucidated. Also, the size and shape of additional nanoparticles in the sample can be determined.

3. Energy dispersive X-ray spectroscopy

Both SEM and TEM can be equipped with some energy dispersive x-ray spectroscopy (EDX) feature. EDX is based on the emission of x-ray after the excitation of the electron probe at the surface of the sample. When an electron hole is created in the inner shell of an atom, an electron with a higher energy can fill the hole and release the energy in the form of x-rays. The x-ray energy is specific to the element nature, and an elemental identification can be done from EDX. The analysis of the x-ray intensity can lead to an elemental composition of the sample surface. However, many elements have peaks overlapping on the energy range, making an EDX spectrum more difficult to analyse. Also, lighter elements, such as carbon, nitrogen or oxygen are not detected efficiently in EDX

compared to heavier elements such as iron or copper. It can be explained by the lower rate of x-ray emission for light elements, where Auger electron emission is preferential. It is preferred to use EDX as a qualitative analysis, and use other characterization technique to get a precise elemental composition.

EDX is used with the TEM when the GNFs are analysed. EDX indicates the composition of specific regions of interest to be compared. Thus, the presence of an element in a region of the sample can be deduced.

4. X-ray photoelectron spectroscopy

X-ray photoelectron spectroscopy (XPS) is used to determine the precise elemental composition at the surface of the studied samples. The samples are placed in an ultra-high vacuum chamber (10⁻⁹ to 10⁻¹⁰ kPa) and irradiated with monochromatic x-rays coming from aluminium or magnesium sources. These x-rays have enough energy to extract electrons from the core shells of atoms at the surface of the samples. The kinetic energy of the expulsed photoelectrons is measured by an energy electron analyser, and the binding energy of the photoelectron can be calculated by Einstein's equation:

$$E_B = h \cdot \nu - E_K$$

where E_B is the binding energy, h is the Planck constant, v is the frequency of the x-ray, and E_K is the kinetic energy of the photoelectron measured by the detector. The photoelectrons are typically coming from the first 10 nanometers of the sample thickness, but most of the signal actually comes from the first atomic layers of the surface.

A spectrum with the number of electrons for each binding energy is then produced. Photoelectron binding energy is specific for each element, and an elemental composition can be calculated based on the surface area of the different peaks. It has to be noted that

hydrogen, and also helium, are not detected by XPS, meaning the obtained composition actually exclude the amount of hydrogen in the sample. The detection limit for an element is around 0.1 at%.

XPS can also give information about the local bonding environment of the atoms at the surface of the sample, and identified as the chemical state of the element. Indeed, the binding energy of the detected elements is shifted depending on the nature, electronegativity, and type of bonding of the closest neighbours. XPS peaks can generally be deconvoluted to evaluate the contribution of each single chemical state for a given element. Symmetrical Voigt profiles are generally used for the deconvolution of most chemical states, where their position, intensity and width are varied for the fit of the experimental peak. However, some specific chemical states, such as the carbon sp2, exhibit asymmetrical properties which can be taken into account for the deconvolution.

The elemental composition of the GNFs is evaluated by XPS. By deconvolution of the different elemental peaks, some information can be found such as the amount of graphitic carbon, and the nature and relative amount of the functional groups attached to the GNFs.

5. Neutron activation analysis

Knowing the elemental composition at the surface of the sample by XPS can be insufficient for complex materials, and investigating specific elements content in the bulk of the sample can be done with neutron activation analysis (NAA). NAA is based on the irradiation of a sample with thermal neutrons, which are neutrons in thermal equilibrium with the room temperature. A small fraction of the atom nuclei present in the sample are capturing a thermal neutron, leading to the formation of an isotope. The resulting has to be a radioisotope, or in other words an unstable isotope which is going to decay. The decay of the radioisotope to a ground state comes with the emission of specific gamma rays, whose energy

depends on the nature of the element. The gamma rays are detected with a germanium semiconductor and a spectrum is made based on the gamma ray energies and intensity. Some elements (H, He, Li, Be, B, C, N, O) are not detected by NAA at all, for several reasons including a low activation level, an extremely short or very long half-life of the radioisotope, the absence of gamma ray emission. The limit of detection depends on each element, but can go from $10^{-7} \,\mu\text{g/kg}$ for the most sensitive elements to 30 $\,\mu\text{g/kg}$ for the less sensitive elements.

NAA needs a nuclear reactor immersed in a water pool, to mainly cool down the reactor and protect users from radiations. The thermal neutrons are produced by enriched uranium in the nuclear reactor. The samples do not need any particular preparation, and they can be activated by the neutrons in their normal state (liquid or solid).

NAA is used on the GNFs to determine the amount of iron contained in the GNFs, mostly when XPS failed to detect iron on the surface of the samples.

6. Raman spectroscopy

Raman spectroscopy is a vibrational spectroscopy method based on the existence of a frequency shifted spectrum in the scattered light by a sample irradiated by electromagnetic radiation. The radiation is monochromatic and comes from a laser, whose wavelength can be chosen to have the best sensitivity and spatial resolution. The choice for a laser wavelength is also based on the nature of the sample. For example, blue and green lasers are better for carbon based materials.

When photons from an incident beam arrive on a sample, they can be transmitted through the sample, absorbed, or scattered in every spatial directions. Scattered photons result in elastic or inelastic collision with atoms composing the samples. Most photons are scattered through elastic collision, known as Rayleigh scattering. Less than one millionth of the photons are scattered with inelastic collision, resulting in phonon generation in the crystalline

structure, which is known as Raman scattering. The scattered photon frequency can be higher (Stokes effect) or lower (anti-Stokes effect) than the initial frequency. Stokes effect is dominant at room temperature.

A Raman spectrum is based on a relative wavenumber, which is the difference between the Rayleigh wavenumber and the Raman wavenumber. The intensity and frequency associated with phonons is characteristic of a molecule or a crystalline structure. The nature and structural properties can be deduced from Raman spectroscopy.

Raman spectroscopy produces some peaks of interest in the case of carbonaceous materials. The study of these peaks can lead to information such as the quantity of graphitic carbon and defects, and so an evaluation of the crystallinity of the sample.

7. X-Ray Diffraction

X-rays can be diffracted by the 3D crystalline structure, due to the wavelength of the incident beam, which is close to the interspacing of the crystalline planes. This property is used in the X-ray diffraction (XRD) technique to analyse crystalline materials. X-rays are generated by a cathode ray tube, based on the interaction between electrons and a target made of materials such as tungsten or copper. The incident beam is then filtered to become monochromatic. X-rays are then focused and irradiate the sample to be studied. Constructive interferences are built when Bragg's Law is satisfied.

$$n\lambda = 2d \sin \theta$$

where λ is the wavelength of the incident x-ray beam, d is the interspacing of the crystalline planes and θ is the diffraction angle. The incident x-ray beam generally scans a range of 2θ angles, and the diffracted signal is collected. The identification of the crystalline phases in the sample can be deduced from the diffraction peaks and a database of existing crystalline

phases. The sample has to be under the form of a powder to be studied by XRD. If not, the sample has to be grounded to become a powder and be analysed.

The crystalline structure of the GNFs is already well-known, but XRD is useful to determine the structure of additional phases contained in the samples.

8. Thermogravimetric analysis

Thermogravimetric analysis (TGA) follows the mass change of a sample at a given temperature or temperature profile. A sample is placed in a heat-resistant platinum holder having its weight recorded with a high precision balance. The apparatus is placed in a programmable furnace generally going up to 2,000°C and having a high precision on the temperature, and the temperature change. The evolution of the mass under the profile of temperature can be done in inert (nitrogen, argon) or oxidizing (air, oxygen) atmosphere. TGA can provide information about the decomposition temperature of a material, and so its thermal stability under a range of temperature. For complex materials having different decomposition temperatures, it is possible to determine the weight percentage of each compound. For example, it is possible to determine the moisture content of a material by following the mass loss at 100°C.

TGA is used to determine the decomposition temperature of the non-functionalized GNFs, and also the content of functional groups, which are degraded at a lower temperature.

9. UV-visible spectroscopy

UV-visible spectroscopy is based on the absorption of photons in UV and visible range by molecules. In order to absorb these photons, the molecules need π -electrons or non-bonding electrons. The absorption wavelength depends on the energy required to excite the electrons to higher anti-bonding molecular orbitals. UV-visible spectroscopy can be used to

determine the nature of the absorbing species, based on the different peaks of absorbance in the spectrum, or the concentration of these absorbing species, based on the Beer-Lambert law.

$$A = log_{10}\left(\frac{I_0}{I}\right) = \varepsilon CL$$

where A is the absorbance, I_0 is the intensity of the incident beam, I is the intensity of the transmitted beam through the sample, ϵ is the extinction coefficient, specific for each absorbing species, C is the concentration of absorbing species in the sample and L is the sample length crossed by the UV-visible beam. The absorbing species that are studied by UV-visible spectroscopy can be dispersed or diluted in a solvent. The contribution of the solvent to the absorption has to be removed by doing a blank measurement with the solvent in the quartz cuvette.

UV-visible spectroscopy helps to determine the stability of GNF based nanofluids, by following the change in the absorbance of the nanofluids due to agglomeration of the nanoparticles.

10. Rotating disk electrode

Rotating disk electrode (RDE) is a three electrode system used to characterize the electrocatalytic activity of a sample. The sample is deposited on a conductive electrode, embedded in a polymer or resin and acts as a working electrode. A counter electrode generally made of a platinum wire and different reference electrodes (silver/silver chloride, saturated calomel, reversible hydrogen...) can be used with the working electrode. The three electrodes are immersed in a solution whose pH can be tuned for the study of the catalytic activity in different media. Gases such as oxygen or nitrogen can be bubbled in the solution in order to saturate it with dissolved oxygen or purge the solution of the dissolved oxygen.

The working electrode is rotated at various rotation rates, creating a constant laminar flow at the surface of the electrode. The steady-state current is consequently controlled by the solution flow rather than diffusion process. The potential of the working electrode can be varied linearly (linear sweep voltammetry) or cyclically (cyclic voltammetry) and the current density is measured. RDE allows the study of multi-electron transfer, kinetics of an electrochemical reaction and other electrochemical phenomena.

RDE is employed to evaluate the ORR performance of the GNFs which have been functionalized to be turned into active catalysts. RDE is used there as a screening technique to compare the samples between each other, and provides insight on the link between composition of the sample and resulting ORR performance.

Chapter 4 IRON FUNCTIONALIZATION OF THE GRAPHENE

NANOFLAKES FOR NON-NOBLE METAL CATALYST

APPLICATIONS

Part I Iron functionalization on graphene nanoflakes using iron powders and iron acetate as precursors

This section presents an article that has been published in the journal Applied Catalysis A, and whose full reference is:

U. Legrand, J.-L. Meunier, D. Berk, Iron functionalization on graphene nanoflakes using thermal plasma for catalyst applications, Applied Catalysis A, 528, 36-43, 2016.

The work has been conducted, analyzed and written by U. Legrand (Ph.D. candidate), while Dr. J.-L. Meunier and Dr. D. Berk provided supervision and reviewing to the manuscript. This article represents the first attempts to one of the main objective of this thesis, i.e. realizing the atomic dispersion of iron on nitrogen functionalized graphene nanoflakes for the generation of a non-noble metal catalyst. The iron precursors (iron powders and iron acetate solution) successfully generate iron vapour in the thermal plasma, but iron oxide nanoparticles nucleate and grow before being deposited on the GNFs, preventing the atomic dispersion of iron on the surface of the nanoparticles. The resulting samples still exhibit an improvement of their electrocatalytic activity toward the ORR thanks to the presence of the iron oxide nanoparticles. Even if the objective is not completely achieved, this study brings a better understanding on the iron functionalization of the GNFs.

Iron functionalization on graphene nanoflakes using thermal plasma for catalyst application

Ulrich Legrand, Jean-Luc Meunier, Dimitrios Berk

Plasma Processing Laboratory, Department of Chemical Engineering, McGill University

Abstract: Graphene nanoflakes (GNFs), a stack of 5 to 20 layers of graphene sheets, are generated here using methane decomposition in a thermal plasma followed by homogeneous nucleation of the 2-dimensional structures in the gas stream. The GNFs are functionalized with nitrogen and iron to improve their electrocatalytic activity. The iron functionalization step is carried out as a post-processing step within the same thermal plasma reactor used to grow the nanoparticles. Two different iron precursors are tested in the reactor, iron powder and iron (II) acetate solution. The iron source carried by a nitrogen flow is injected in the argon plasma, and parameters such as the plasma power, pressure, and the exposure time during functionalization are optimized for enhanced catalyst activity. Structure and composition of the resulting catalysts are characterized, and their electrocatalytic performances in terms of onset potential, half wave potential and current density show an increase compared to the non-functionalized GNFs. This study proves the ability to entirely produce a pure and highly crystalline graphene-based non-noble metal catalyst using a thermal plasma single batch process with simple precursors such as methane and nitrogen gas, and an iron powder or iron acetate solution.

1. Introduction

Fuel cells, and more particularly alkaline fuel cells (AFCs) form promising energy conversion devices already found in diverse applications, such as transport and portable electronic devices [100]. Based on the oxidation of hydrogen with oxygen or other oxidizing agents, they present the advantage of releasing water vapour as a product without any

pollutants. One key component in AFCs is the catalyst that enables the hydrogen oxidation, and more particularly the oxygen reduction to occur at the low temperature of the device, typically 80°C. Platinum still outperforms any other catalyst material, the drawbacks being price and availability [101]. Generally the oxygen reduction reaction (ORR) is the limiting factor in AFCs, and requires most of the overall catalyst loading. Decreasing the price of the catalyst is thus one of the major issues that needs to be addressed to allow AFCs to reach larger markets. This can be achieved by reducing the amount of platinum used or by replacing the platinum with a cost effective non-noble metal catalyst (NNMC) [102–107], which is resistant to corrosion.

The present research on NNMCs is mainly based on the enhancement of the electrocatalytic activity of nitrogen functionalized carbon-based matrices by the addition of iron. Iron atoms can first form catalytic sites when linked by four to six atoms of nitrogen to the carbon support; such active sites were studied by Jasinski more specifically for the activity of iron and cobalt phthalocyanine towards the ORR [80], while Kramm *et al* evaluated and proposed possible active configurations of the Fe/N/C sites [83]. Unfortunately, it is very difficult to identify with certainty the presence of such sites in catalysts material. Iron can also be found in the form of iron oxide nanoparticles, which also catalyses the ORR [78]. Whether atomically dispersed catalytic sites or iron oxide nanoparticles are the active elements in the catalysts, the carbon-based matrix has to be resistant to corrosion and electrically conductive. Graphene materials provide good conductivity as well as resistance to corrosion from their relatively small defect concentrations, and so form excellent structures to support nitrogen-iron based functionalities and/or iron oxide nanoparticles [108–110].

Highly crystalline graphene has been shown to be the best candidate for the ORR because of its resistance to both acidic and basic environments, and its high electrical

conductivity [9]. A common method to produce graphene is by the reduction of graphene oxide obtained by the exfoliation of graphite, resulting in a graphene containing a large number of defects in its crystalline structure [111]. Preparation of the graphene structure as a catalyst support material using for example the method developed by Proietti *et al* [112] also generates additional defects in the structure, defeating the purpose of getting a highly crystalline graphene.

The present work intends to introduce a new and original method for the synthesis of a complete non-noble metal catalyst using a high temperature thermal plasma reactor. Introduction of iron to nitrogen functionalized graphene nanoflakes (N-GNFs) for producing active ORR catalysts has been demonstrated by Pascone *et al* using a wet-chemical method as a post-production step [113]. One objective of the present paper is to take advantage of the high reactivity of the plasma environment in the GNFs synthesis phase and produce a ready-made iron catalyst in a single batch process. The reactor is first used to grow the graphene structure through homogeneous nucleation from the gas phase, as proposed by Pristavita *et al* [6,114] in the production of the GNFs. It has been shown that nitrogen can be added to GNFs within the thermal plasma system resulting in low (~2 at% using the GNF nucleation stage) and high (~25 at% using the downstream afterglow plasma) functionalization levels [8]. Up to 70% of the overall nitrogen was found to be attached through pyridinic or pyrrolic sites on graphene in a similar way to the phthalocyanine structure [8]. The GNFs maintained a good crystalline structure after the different functionalization steps with both low and high contents of nitrogen.

The present study mainly focusses on testing and optimizing a second *in situ* post-synthesis step, namely the addition of iron to the N-GNFs structures within the same plasma reactor. The optimal conditions used for GNFs growth and nitrogen functionalization steps are maintained as defined in previous work [6]. Two sources of iron are tested here following

the growth and the nitrogen functionalization of GNFs, these being (a) iron powder and (b) iron (II) acetate solution, both using nitrogen as a carrier gas. Experimental tests are performed under different operating conditions within the reactor in order to achieve both nitrogen and iron functionalization on the GNFs (N/Fe-GNFs) within a single overall batch process made without opening the reactor. The resulting materials are then characterized for the structure of the graphitic material, the atomic composition of the sample surface, and the activity in the ORR.

2. Experimental methods

2.1. Catalyst generation

The generation of GNFs following Pristavita *et al.*'s procedure [6] uses methane as a carbon source that is decomposed within an argon thermal plasma. The argon thermal plasma is generated by an inductively coupled plasma (TP-ICP) torch, with a power of 20 kW delivered to the torch while the pressure within the reactor is 55.3 kPa. GNFs are formed as small nuclei through homogeneous nucleation. Modelling studies provide indications that GNFs essentially grow laterally in a sheet-like geometry within a very narrow nucleation and growth temperature window of 3 700 – 4 900 K in the plasma decay zone [28]. The nanoparticles are deposited on the walls and at the end plate downstream of the reactor, these deposits being further functionalized in the plasma recombination zone. The experimental reactor is axisymmetric with respect to the flow pattern, including the exit flow that extends radially from the downstream endplate. This provides a very good match with the modelled 2-D geometry, and an experimental flow pattern having a true stagnation point flow geometry with no recirculation loops throughout the reactor [28]. A small amount of nitrogen is added during the growth, leading to nitrogen content up to 2 at% on the surface of the GNFs.

As indicated above, iron is added in two different forms by switching off the methane gas feeding and introducing the iron source without opening the reactor. The main tested parameters during the functionalization step are the type of iron source (powder or iron acetate solution), the pressure within the reactor, the power delivered to the ICP torch, and the exposure time to the iron vapour.

The first iron source is a mixture of two iron powders fed to the reactor using a PFV100-VM-NO powder feeder from TEKNA. A mixture is used because large iron particles with a size range between 10 and 300 µm are easy to feed continuously but difficult to vaporize while small iron particles between 1 and 10 µm are easy to vaporize but difficult to feed; mixing the powders takes advantage of both aspects, i.e. a continuous feeding and a good rate of vaporization. The optimized amount of small particles is 30 weight percent (wt%) of the total weight of iron powder injected within the reactor. A flow of 1 slpm of nitrogen has been chosen in order to carry the flow rate of 10 mg/min of iron particles from the powder feeder to the reactor and help the implementation of iron atoms on the GNFs surface. The iron particles are injected in the plasma zone, 9 cm downstream of the ICP torch nozzle using a side port on top of the reactor. This type of injection overcomes difficulties of particle transport within the injecting probe of the ICP torch.

The second source of iron is a ferrous acetate solution at a concentration of 1 mg/mL. The introduction of 10 mL of this solution is made using a 20 mL stainless steel syringe from Chemyx, using a Nexus 3000 pump, delivering the solution at a flow rate of 1 mL/min. The liquid is carried to the reactor using a flow rate of 1 slpm of nitrogen. In contrast to the iron particles, the ferrous acetate solution is fed through the injection probe of the ICP torch in the core of the plasma. It is expected that the difference in location of the iron source injection has a minor influence on the resulting vaporization, both streams being effectively injected within a relatively large volume having a temperature field range of 6 500

- 7 500 K occurring downstream of the torch nozzle [16]. In contrast, the physical state of the precursors in the form of a liquid solution or solid particles is dominant in controlling the quantity of iron vapour generated in the stream. Because of practical injection considerations generating different iron mass feeds, the amounts of iron vapour generated from the two sources are different. Also, it is expected that the level of iron functionalization is going to differ from one iron source to the other.

Two specific conditions for the power delivered to the ICP torch as well as the pressure within the reactor are chosen, namely 20 kW/ 55.3 kPa (8 psia) and 25 kW/ 13.8 kPa (2 psia). These were established through the theoretical modelling of the temperature and flow fields in the reactor showing that these two pairs of values presented similar temperature distribution profiles with the core of the plasma jet in the ICP torch reaching 10 000 K, and the walls of the reactor being cooled at 300 K [28]. The main difference between the two power/pressure conditions is in the velocity profiles. The maximum calculated velocity of the plasma, 160 m/s in the 13.8 kPa case, is four times greater than that in the 55.3 kPa case [115]. It is expected that the difference in the velocities and consequently in the residence time of the excited species in the plasma recombination zone would influence the iron functionalization of the GNFs. Also, the exposure time of the GNFs to the iron vapour is expected to be a key factor in the iron functionalization step. A short exposure time would lead to an insufficient amount of catalytic sites generated while a long exposure time could overload the samples with iron when considering the limited amount of the nitrogen-based host sites. The overall tested conditions are summarized in Table 4-1.

Table 4-1: Experimental conditions of the iron functionalization step.

Iron Source	Power/pressure	Exposure time (min)	Sample name
Iron powder	20 kW / 55.3 kPa	05	N/Fe-GNF1
		10	N/Fe-GNF2
	25 kW / 13.8 kPa	05	N/Fe-GNF3
		10	N/Fe-GNF4
Iron Acetate	20 kW / 55.3 kPa	05	N/Fe-GNF5
		10	N/Fe-GNF6
	25 kW / 13.8 kPa	05	N/Fe-GNF7
		10	N/Fe-GNF8

2.2. Physical characterization

The structure of the N/Fe-GNFs was studied using Scanning Electron Microscopy (SEM) on a FEI Inspect F-50 FE-SEM and Transmission Electron Microscopy (TEM) on a FEI Tecnai G2 F20 200 kV Cryo-STEM. Raman spectroscopy was used to give information on the graphitization of the samples, and was performed on an inVia Reflex confocal micro-Raman (Renishaw) with a laser emitting at a wavelength of 514.5 nm. X-ray Photoelectron Spectroscopy (XPS) was employed to investigate the chemical structure of the surface of the catalysts, using a Scientific K-Alpha XPS system from Thermo Scientific with an aluminium x-ray source on analysed surfaces of 400 µm spot size.

2.3. Electrochemical characterization

The activity of the resulting catalyst is studied using Rotating Disk Electrode (RDE) electrochemical analysis. The samples are prepared on 5 mm glassy carbon tips by drying a small volume (20 µL) of a catalyst ink made of N/Fe-GNFs, water, ethanol and Nafion[©], resulting in a loading of 0.1 mg/cm² of catalyst. The tests are performed in an alkaline medium made of a 0.1 M sodium hydroxide solution at room temperature, using a platinum wire counter electrode, and a saturated silver/silver chloride (Ag/AgCl) reference electrode. All tests are performed at a rotation speed of 2500 rpm. First, the catalysts go through a conditioning procedure consisting of repeated cycles between +1 and -1V, at a scan rate of 500 mV/s, under N₂ bubbling in the medium. This procedure removes the impurities at the surface, allowing an optimal catalyst utilization [116]. After that, a background correction is done with linear sweeps between +1 and -1V, at a scan rate of 20 mV/s, under N₂ bubbling. The background correction suppresses the contribution of capacitive current to the experimental ORR measurements [117]. Finally, the catalysts are tested when the medium is saturated by dissolved oxygen, through linear sweeps between +1 and -1V, at a scan rate of 20 mV/s. The eight prepared samples are compared to the non-functionalized GNFs. The potential is converted from the Ag/AgCl reference to the reversible hydrogen electrode (RHE). Equation 1 is used to convert the measured potential to RHE as follows:

$$E_{RHE} = E_{Ag/AgCl} + E_{Ag/AgCl}^{0} + 0.059 pH$$
 Equation 1

where $E_{Ag/AgCl}^{0}$ is the standard potential for Ag/AgCl electrode and equal to 0.1976 V. The pH of the sodium hydroxide solution has been measured at 13. The parameters used to compare the performances of the different candidates are the onset potential, the half-wave potential and the current density at 0.4 V.

3. Results and discussion

3.1. Structure of the N/Fe-GNFs

The structure of the catalysts was analysed by scanning and transmission electron microscopy (SEM, TEM). The SEM micrographs of two representative samples of both iron sources are shown in Figure 4-1. The functionalized GNFs have a homogeneous and fluffy appearance, typical of this material [6]. It is important to note that the addition of carbon from the acetate ion is not seen to generate amorphous carbon, which would be recognizable by a cauliflower-like structure, or other impurities in the observed samples [118].

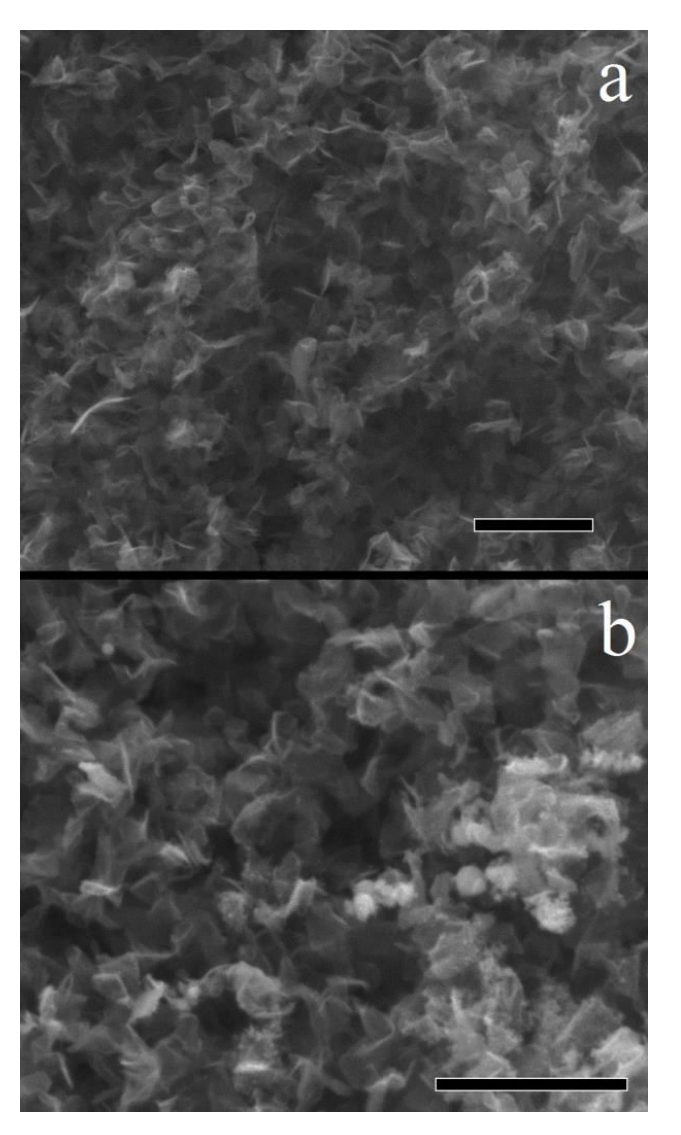


Figure 4-1. SEM picture of the samples a) N/Fe-GNF8 and b) N/Fe-GNF1 for a scale bar of 500 nm.

Micro-particles of iron which have not completely evaporated have been found in the samples obtained with the iron powder source. As expected from the iron particle feed based on a 2-peak particle size distribution, the vaporization of iron particles is not complete. Spherical nanoparticles have been observed in samples from both iron sources, with the greater amount in the case of the iron powder source. In order to determine the nature of these nanoparticles, the samples have been analysed by TEM, and a micrograph from the sample N/Fe-GNF5 is shown in Figure 4-2. Graphene nanoflakes are observed, and some of them appear to be covered by spherical nanoparticles. The size distribution of the spherical nanoparticles for the samples functionalized with iron acetate solution is 6.5 ± 2.2 nm, and 7.8 ± 2.6 nm when the iron source is iron powder. However, larger nanoparticles, up to 20 nm, have been observed with the iron powder source, such as the one depicted on Figure 4-3. It can be seen that the repartition of the nanoparticles is not uniform. Some regions contain a large amount of spherical nanoparticles, while others do not contain any nanoparticles on the GNFs.

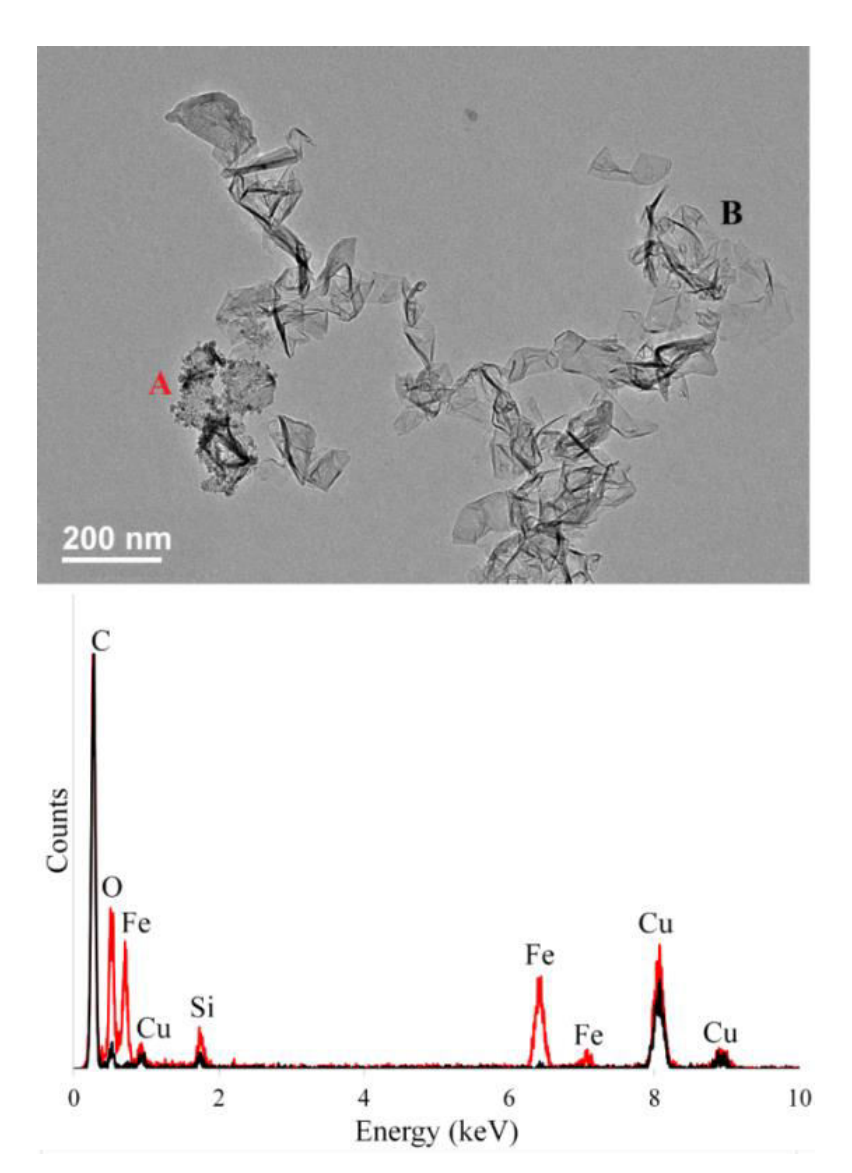


Figure 4-2. TEM picture of N/Fe-GNF5 with a scale bar of 200 nm, with EDX spectra of the zone A, containing iron oxide nanoparticles (in red) and the zone B, containing only GNFs (in black).

An energy dispersive X-ray (EDX) spectroscopy has been performed on the area containing the GNFs covered by the spherical nanoparticles, and compared to an area without presence of these nanoparticles. The EDX spectra reveal the presence of carbon, oxygen, iron, copper, and silicon. Carbon is the main component of the GNFs, and the carbon peak was used to normalize both spectra. The presence of copper is explained by the copper grid used to deposit the samples while the trace amounts of silicon are impurities originating from the silicon grease used to seal the plasma reactor. By comparing the two spectra, it can be

deduced that the spherical nanoparticles are made of iron oxide. Indeed, a small amount of oxygen is naturally present in the GNFs, but this amount drastically increases in the spherical nanoparticles area. The nature of the iron oxide has been determined by taking a closer look on the nanoparticles with the help of the high resolution TEM (HR-TEM) as seen on Figure 3. The measurement of the interspacing distances between paralleled planes gives a distance of 0.29 nm, identified as the (220) interspacing distance for γ -Fe₂O₃ [119]. The interspacing distance has also been measured on other samples, and the interspacing distances of the planes (220), as well as the planes (100) have been found. The nature of the iron oxide is later confirmed by the XPS analysis.

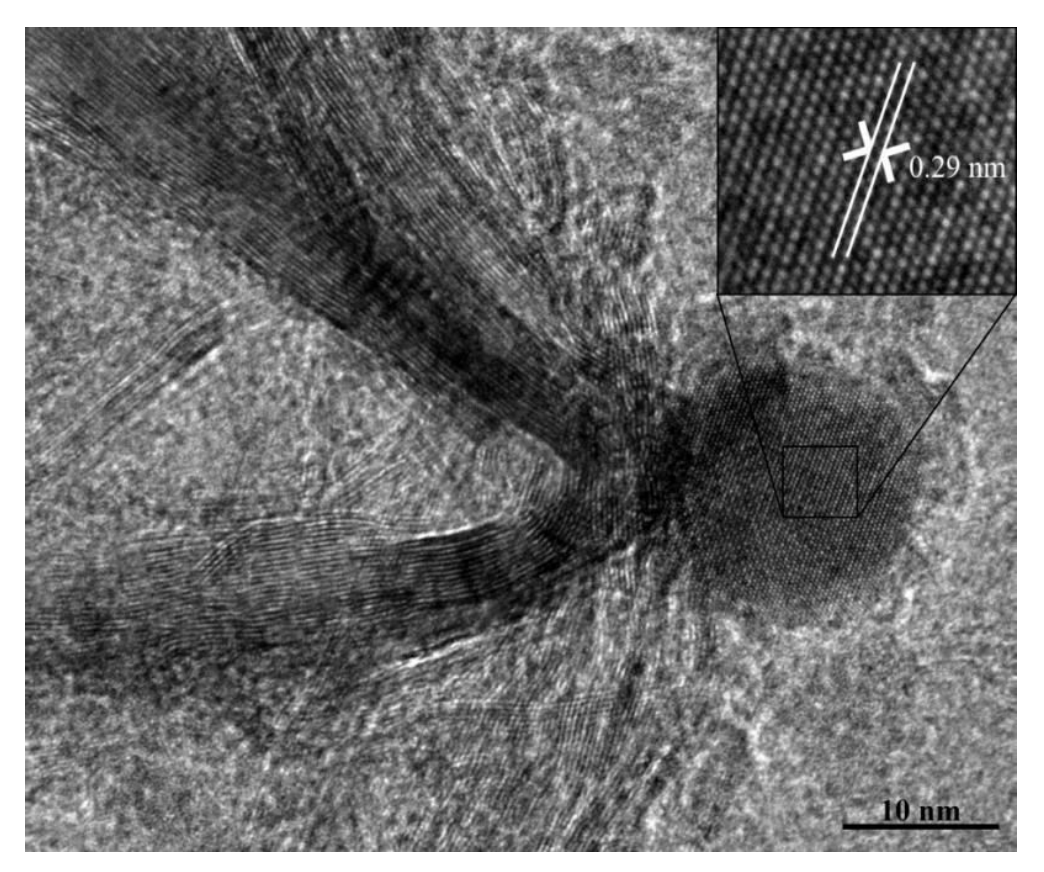


Figure 4-3. High resolution TEM picture of N/Fe-GNF1.

The effect of the functionalization on the samples graphitization was analysed by Raman spectroscopy. Raman spectra of functionalized and non-functionalized samples are shown in Figure 4-4, and exhibit several peaks of interest, typical of graphitic materials. The

D peak, located at 1350 cm⁻¹, is correlated with the amount of non-graphitized carbon in the graphitic structure, while the G peak, found at 1580 cm⁻¹, is associated with the graphitized carbon contained in the sample. The G' peak at 2700 cm⁻¹ sees its intensity and sharpness increased when the number of graphene sheets in the stack decreases. The quality of the graphitic material can be quantified by graphitic indices, such as the purity, the crystallite size (L_a) and the average length of graphene planes (L_{eq}), whose relations have been established by Larouche *et al.* [120], and are based on the intensity and underlying area of the D, G, and G' peaks. The crystallite size, L_a, represents the size of a defect-free area in the graphitic structure, while the average length of graphene planes can be represented by the total length of planar structures linked by curvature. The values of the graphitic indices for the functionalized and non-functionalized sampled are summarized in the Table 4-2.

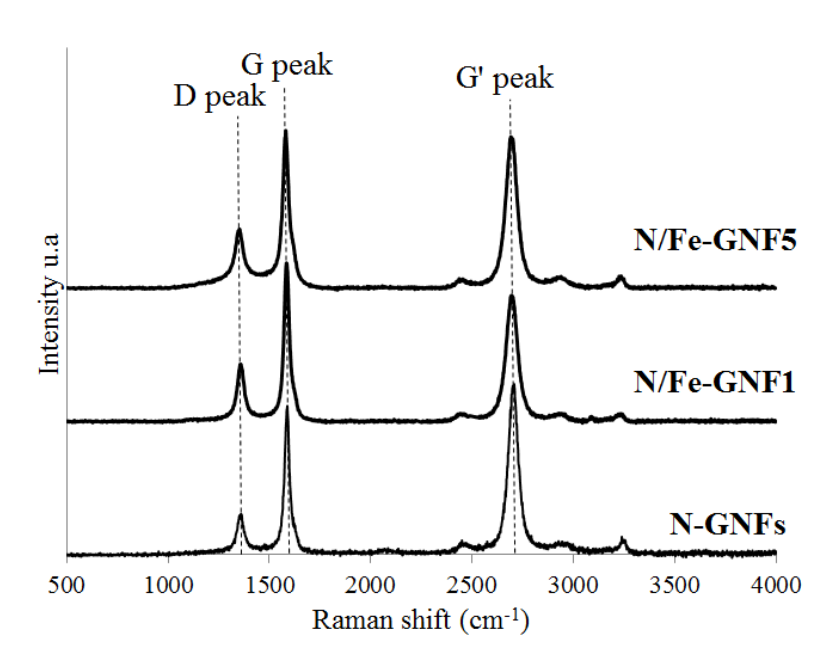


Figure 4-4: Raman spectra for non-functionalized and two functionalized samples (N/Fe-GNF1 and N/Fe-GNF5).

The values of the purity, as well as L_a and L_{eq} stay in the same range before and after functionalization, showing that the iron/nitrogen functionalization step seems to not deteriorate the graphitic structure of the GNFs by addition of defects. The purity, defined as

the ratio of the G to D peak is generally close or lower than 1 for materials such as graphene oxide and reduced graphene oxide, widely used in the preparation of non-noble metal catalysts [111]. The GNFs exhibit values between 2.3 and 3, denoting a large amount of graphitized carbon and showing the higher crystallinity of the samples produced here.

Table 4-2: Graphitic indices relations [120] and corresponding values for the GNFs samples.

Sample	Purity	L_{a}	$L_{ m eq}$
Sample	(± 0.2)	(± 0.3 nm)	(± 0.5 nm)
Relations	I_{G}/I_{D}	$4.4xA_G/A_D$	8.8xA _{G'} /A _D
N-GNFs	2.8	8.8	28.2
N-Fe/GNF1	2.8	9.2	26.6
N-Fe/GNF2	3.0	10.8	32.5
N-Fe/GNF3	2.6	8.8	30.2
N-Fe/GNF4	2.3	9.2	28.4
N-Fe/GNF5	2.7	8.6	26.2
N-Fe/GNF6	2.6	9.0	29.0
N-Fe/GNF7	2.6	8.9	24.4
N-Fe/GNF8	2.6	7.1	24.0

3.2. Chemical composition of the N/Fe-GNFs

XPS was used to determine the atomic composition of the N/Fe-GNFs surface. The surveys of two representative samples from both iron sources compared to the survey of N-GNFs are shown in Figure 4-5 while the composition of every single sample is given in Table 4-3.

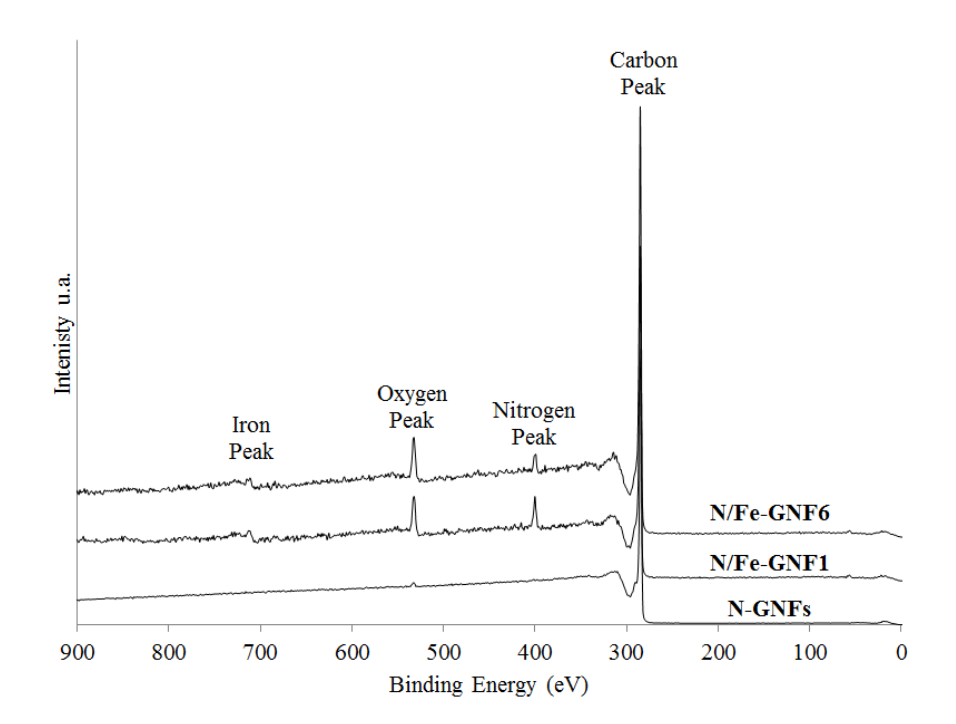


Figure 4-5: XPS survey scan of two samples (N/Fe-GNF1 and N/Fe-GNF6) compared to the N-GNFs.

Table 4-3. Atomic composition at the surface of the N/Fe-GNFs.

Sample	C (at%)	N (at%)	O (at%)	Fe (at%)
N-GNFs	98.07	0.56	1.37	-
N-Fe/GNF1	91.53	4.76	3.54	0.18
N-Fe/GNF2	93.49	1.09	4.94	0.48
N-Fe/GNF3	89.39	4.50	6.01	0.10
N-Fe/GNF4	86.49	5.69	7.75	0.08
N-Fe/GNF5	89.31	4.79	5.79	0.11
N-Fe/GNF6	92.36	3.55	3.94	0.15
N-Fe/GNF7	89.25	4.60	6.09	0.06
N-Fe/GNF8	81.93	8.47	9.52	0.07

From the atomic composition given in Table 4-3, the functionalization step improves drastically the level of nitrogen and oxygen present on the surface of the GNFs. On average, the level of attached oxygen is greater for the iron source being iron (II) acetate solution (N/Fe-GNF5,6,7,8). This can be explained by the large amount of oxygen contained in water and acetate ions, compared to the oxygen contained in the iron powder in the form of a surface oxide layer. Also, the levels of nitrogen and oxygen are greater when the functionalization step takes place at high-power/low-pressure values of 25 kW/13.8 kPa (N/Fe-GNF3,4,7,8). Previous studies on the addition of nitrogen and oxygen have already shown that the low pressure and high power conditions resulted in higher incorporated

amount of each element, these conditions causing much shorter transit times of the active species between the plasma and the GNF powders [8,115].

The exposure time during the functionalization step does not seem to correlate with the increasing level of oxygen or nitrogen in the GNFs. Indeed, the samples (N/Fe-GNF2,6) exposed to a functionalization step at 20 kW/55 kPa globally see their nitrogen and oxygen level decreasing when the exposure time is higher while the samples (N/Fe-GNF4,8) functionalized with a higher power and lower pressure have greater amounts of nitrogen and oxygen after a longer exposure time. The temperature fields being similar in both conditions, one may speculate that the higher thermal load expected in the low-power/high pressure condition may influence the loss of some nitrogen and oxygen functional groups on the N/Fe-GNFs structures.

The present results show the effect of the iron source on the iron functionalization. It appears that the iron powder source leads to more iron on the surface sample than the iron (II) acetate source. This difference may come from the different mass flow rates of iron between the two sources, ten times higher in the case of the iron powder. The amount of iron on the GNFs is also greater when the plasma conditions of the functionalization step are 20 kW/55 kPa, especially when the source is iron powder. This can be explained by the longer residence time of the powder in the hot regions of the plasma resulting in higher vaporization rates. The results on the amount of iron in the samples need however to be taken with precaution due to differences between the surface composition and the actual amount contained in the sample. For the iron powder as a source, 50 wt% of iron is actually present in the samples while the XPS results give values up to 0.48 at%, which would be equivalent to 2 wt% when considering the surface composition of the sample. The way iron oxide nanoparticles form and are deposited non-homogeneously on the GNFs as well as the presence of unevaporated

micro-particles in the case of the iron powder source induce the differences in the reading of the level of iron at the surface and the actual amount of iron.

The high resolution XPS peaks of carbon for each sample are depicted in Figure 4-6. The shape of the carbon peak, typical of a graphitic carbon, is similar before and after functionalization. Small differences can be detected in the region 285-289 eV, related to carbon-oxygen bonding. Indeed, the functional groups C-O, C=O and O-C=O are respectively associated with 285.5, 287.7 and 286.7 eV. The preservation of the carbon peak shape before and after functionalization indicates that most of the carbon from the samples remains in the sp² state, meaning that there is no transformation of graphitic carbon into amorphous carbon, confirming the observation of the Raman spectroscopy.

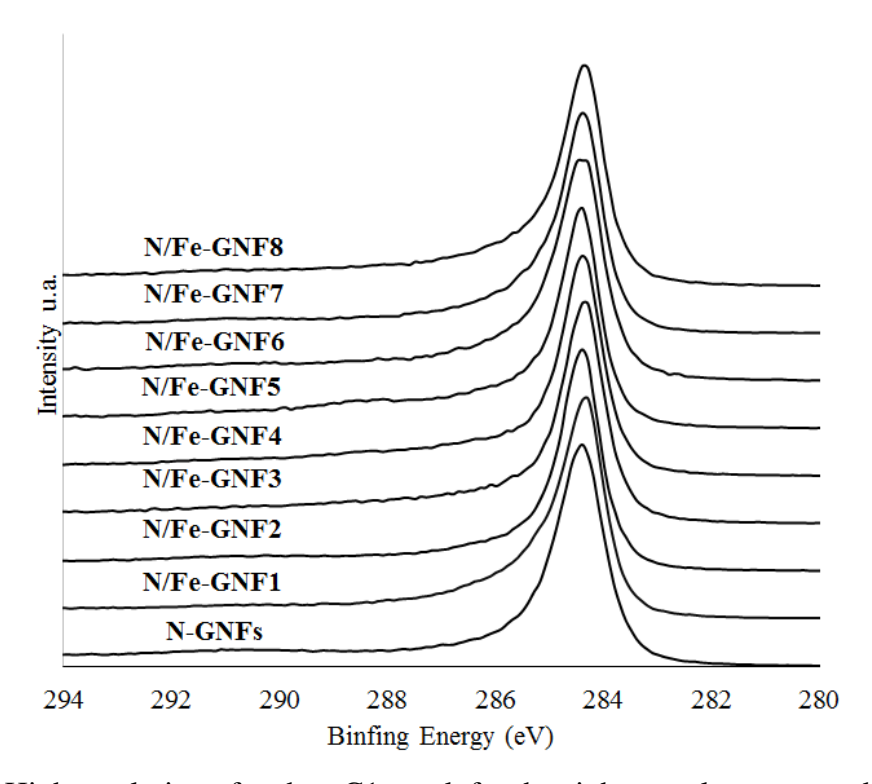


Figure 4-6: High resolution of carbon C1s peak for the eight samples compared to the non-functionalized GNFs.

The high resolution peaks of nitrogen for typical samples are represented in Figure 4-7. The peaks are deconvoluted based on elementary Gaussian-Lorentzian fitting. The main

binding energies used for the deconvolution are 398.9, 399.8 and 401.3 eV, respectively associated with pyridinic, pyrrolic, and graphitic nitrogen species. The ratios of the different type of nitrogen species for each functionalized samples are summarized in Table 4-4. No clear trend can correlate the experimental conditions to the resulting nitrogen species in the samples. The importance of each type of nitrogen for the ORR is still controversial in the literature, contradictory studies claiming pyridinic, pyrrolic or graphitic nitrogen is the specie responsible of the improvement of the electrocatalytic activity of the functionalized graphene sample [121].

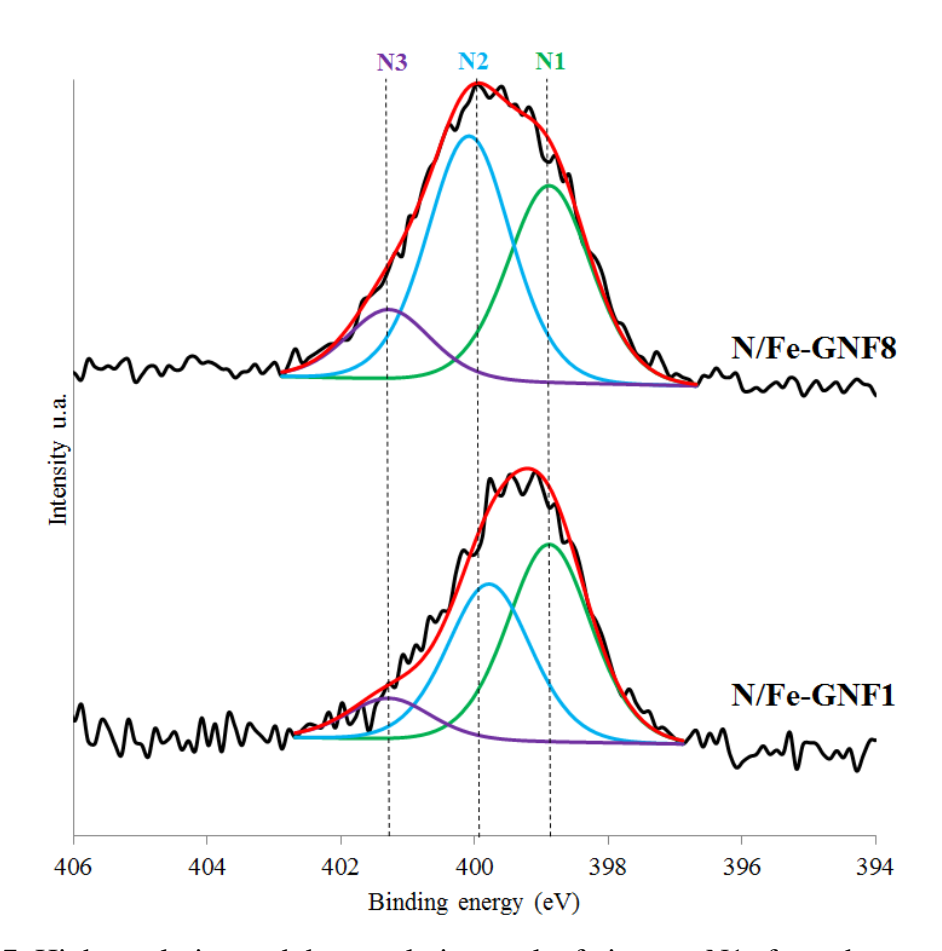


Figure 4-7: High resolution and deconvolution peak of nitrogen N1s from the samples N/Fe-GNF1 and N/Fe-GNF8. N1, N2 and N3 are respectively associated to pyridinic, pyrrolic and graphitic nitrogen.

Table 4-4: Repartition of pyridinic (N1), pyrrolic (N2) and graphitic (N3) nitrogen species for each N/Fe-GNFs sample.

Sample	N1 (%)	N2 (%)	N3 (%)
N-Fe/GNF1	50.0	39.8	10.2
N-Fe/GNF2	34.3	38.3	27.4
N-Fe/GNF3	36.6	52.8	10.6
N-Fe/GNF4	38.2	50.9	10.9
N-Fe/GNF5	42.2	52.6	5.2
N-Fe/GNF6	38.0	51.4	10.6
N-Fe/GNF7	36.6	46.6	16.8
N-Fe/GNF8	38.6	47.9	13.5

When the iron peak is intense enough to be clearly identified, for example with sample N/Fe-GNF2, the state of the iron can be analysed (Figure 4-8). The position of the 2p1/2 and 2p3/2 peaks, at 725 and 711 eV respectively, as well as their satellite position, located 8 eV higher than the main peaks, indicate that iron is in the oxidation state +III [122]. The absence of iron in the oxidation state +II confirms the nature of the iron oxide nanoparticles being Fe₂O₃. XPS analysis does not allow to discriminate iron atoms contained in iron oxide nanoparticles and iron surrounded by nitrogen atoms forming a catalytic site [123]. However, iron oxide nanoparticles are expected to participate in the electrocatalytic activity of the materials.

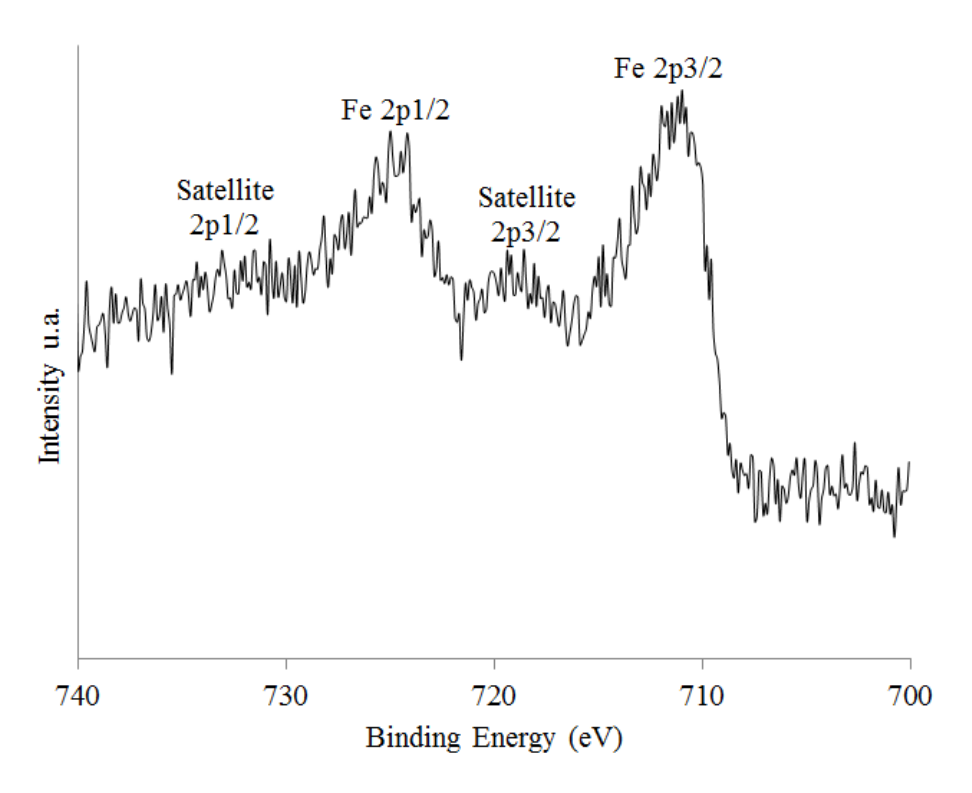


Figure 4-8: High resolution of iron XPS peak from the sample N/Fe-GNF2.

3.3. Activity of the catalysts

The activity of the catalysts is tested by RDE. The performances of all of the catalysts are listed in the Table 3, based on the onset potential, the half wave potential and the current density, at -0.4 V [75]. The onset potential is defined where the electrocatalytic current can be distinguished from 0. The onset potential of platinum based catalysts is around 0.8 V vs RHE, a value where catalysts are considered to have good performances [75]. The half-wave potential is the reported potential where the intensity of the current density is reaching half of its maximum, and represents how sharp the increase of the current density is. The sharpness of the curves is directly related to the kinetics of the reactions; the sharper the curve is, the fastest the reaction is. The current densities, calculated based on the geometric surface area of the RDE electrode, have negative values due to the cathodic nature of the reduction reaction, and are proportional to the rate of reduction of oxygen. Overall, the lowest values for the current density are related to the best catalytic performances. Taking into

account all these parameters, the results for the best samples respectively to both iron sources (N/Fe-GNF1 and N/Fe-GNF5) have been determined, and compared to the non-functionalized GNFs on Figure 4-9. It can be argued that the onset potential for the iron-based samples produced in this method is lower than the one for the platinum-based catalysts. However, the overall catalytic performances are improved after the plasma functionalization step.

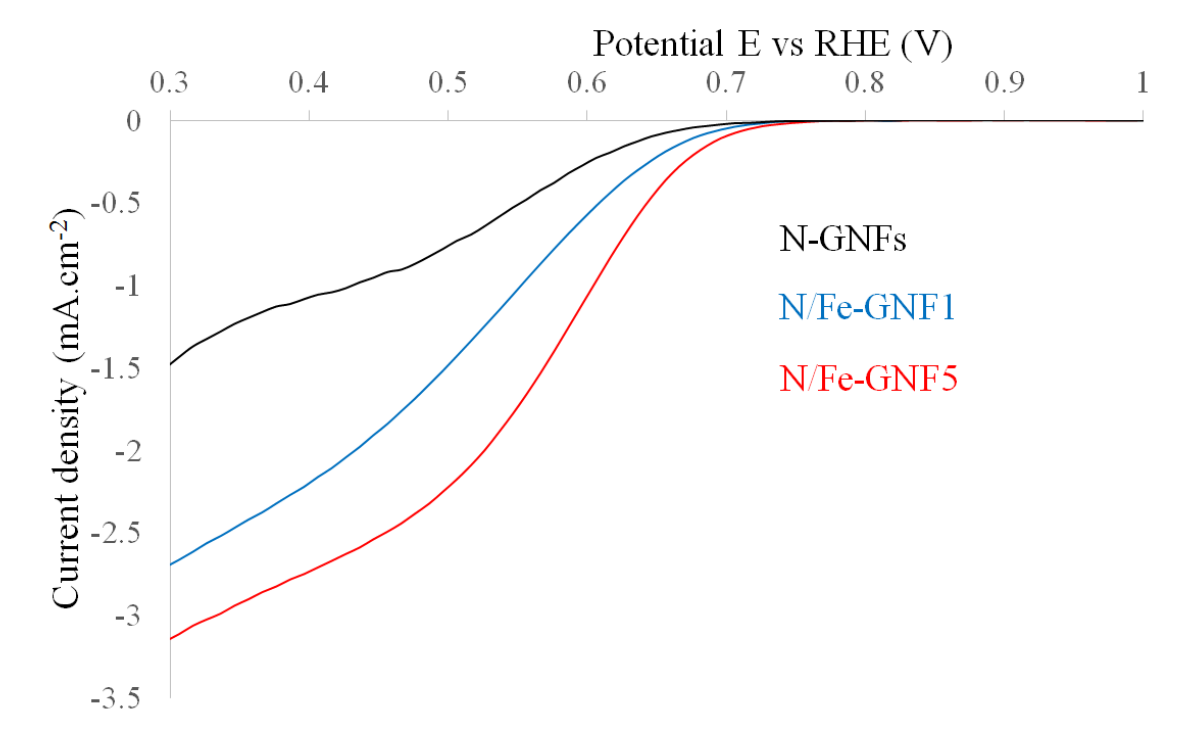


Figure 4-9. Linear sweep voltammetry of samples N/Fe-GNF1 (blue) and N/Fe-GNF5 (red) compared to the N-GNFs in O_2 saturated 0.1 M NaOH, at a scan rate of 20 mV/s, for a rotation speed of 2500 rpm.

Table 4-5: Performance of the catalysts compared to the non-functionalized GNFs.

Sample	Onset Potential (V vs RHE)	Half-wave Potential (V vs RHE)	Current Density @ 0.4 V vs RHE (mA/cm²)
N-GNFs	0.67	0.55	-1.06
N-Fe/GNF1	0.70	0.56	-2.16
N-Fe/GNF2	0.69	0.55	-1.87
N-Fe/GNF3	0.68	0.55	-1.38
N-Fe/GNF4	0.67	0.56	-1.06
N-Fe/GNF5	0.72	0.58	-2.71
N-Fe/GNF6	0.71	0.58	-2.21
N-Fe/GNF7	0.67	0.55	-1.11
N-Fe/GNF8	0.70	0.54	-1.65

3.4. Discussion

The catalytic performances as measured by RDE are in a close range; however the differences observed between the catalysts enables some analysis on the influence of the plasma conditions generating these catalysts. Generally it appears that the catalysts having iron (II) acetate perform better than those having iron powder as a source.

In the case of the catalyst having iron powder as a source, the best plasma conditions for the functionalization step are 20 kW/55.3 kPa, for an exposure time of 5 minutes,

kW/55.3 kPa conditions perform better than those treated by plasma conditions with a higher power and lower pressure. As mentioned previously, the 20 kW/55.3 kPa conditions allow a longer residence time of the injected iron particles in the hot zone of the thermal plasma, increasing their evaporation rate and generating in this way more iron vapour leading to higher iron content in the samples. However, a too long exposure time of the GNFs to the iron powder leads to lower electrocatalytic performances. It is recognized that an excessive amount of iron in the catalyst has tendency to decrease the activity, which could lead to the overall lower performances for this iron source [106].

In the case of iron (II) acetate solution, a similar behaviour seems to affect the activity of the catalyst, where the optimal couple of power and pressure for the functionalization step is 20 kW/55.3 kPa, with a time of exposure of 5 min. The presence of water injected to the plasma requires energy to be vaporized and eventually decomposed. A higher residence time for the iron acetate solution in the hot region of the reactor could lead to a higher generation of iron vapour, leading to a better functionalization rate of the samples, as shown in the XPS analysis.

Most of the catalysts synthesized based on the plasma functionalization step show an improvement of their electrocatalytic activity when compared to the non-functionalized sample. The origin of this improvement is still controversial in the literature. No clear evidence has been found in this study to highlight the presence of catalytic sites for the ORR based on atomic iron surrounded by nitrogen atoms as is the case for the heme-B structure of blood and phthalocyanine. Iron oxide nanoparticles have however been detected in the samples. Studies have been conducted proving that iron oxide nanoparticles are improving the electrocatalytic activity of non-precious metal catalysts [78,124], and often mislead on the comprehension of the involved phenomena. The growth of iron oxide nanoparticles is a

competitive process in the presented method due to the fact that the deposited GNFs are localized in cold areas of the thermal plasma reactor, where the temperature is below the melting temperature of iron (1811K), allowing the diluted iron vapour to condense into iron oxide nanoparticles before being deposited on the surface of the GNFs [125]. The production of iron oxide nanoparticles can also be found in other functionalization methods, such as wet chemistry, due to the precipitation of iron in solution, which is a common method to produce this type of nanoparticles [119].

4. Conclusion

Non-noble metal catalysts for the oxygen reduction reaction have been completely produced by an original method where the carbon matrix is grown and the iron functionalization step is performed in the same thermal plasma reactor by changing the feeding gas conditions. An improvement of the electrocatalytic activity has been noticed for different conditions, depending on the iron source employed. Even if the performances of the catalysts are lower than platinum based catalysts, this study represents the proof of concept on the generation of non-noble metal catalysts from nucleation to various functionalization steps within a thermal plasma reactor in a single batch process. The improvement of the electrocatalytic activity is currently under ongoing research to determine the role of the iron oxide, as well as the effective presence of atomic iron catalytic sites. Also, improvement of the iron functionalization step itself is still studied. Iron functionalization of GNFs in hotter areas of the thermal plasma reactor is considered to increase the chances of a direct contact between the GNFs and iron vapour. The addition of a higher amount of nitrogen functionalities would be another way to improve the electrocatalytic activity of the catalysts.

Part II Iron functionalization on graphene nanoflakes using iron

(II) phthalocyanine as precursor

This section presents an article that has to be submitted and having for reference:

U. Legrand, J.-L. Meunier, D. Berk, Addition of atomically dispersed iron on nitrogen functionalized graphene nanoflakes for catalyst application in alkaline medium, soon to be submitted.

The work has been conducted, analyzed and written by U. Legrand (Ph.D. candidate), while Dr. J.-L. Meunier and Dr. D. Berk provided supervision and reviewing of the manuscript.

This article is the continuation of the previous article whose aim was to achieve the atomic dispersion of iron on the surface of the functionalized GNFs. It has been shown previously that iron powders and iron acetate as precursors favored the formation of iron oxide nanoparticles. In order to prevent the formation of these iron oxide nanoparticles in this study, the precursor is changed to iron (II) phthalocyanine. Instead of trying to build the catalytic sites step by step with the addition of nitrogen followed by the incorporation of iron atoms on the GNFs, the use of iron (II) phthalocyanine aims to incorporate directly the desired structure for the catalyst sites on the surface of the GNFs. The challenge of this study is to preserve the molecular structure of the phthalocyanine in the thermal plasma to reach and functionalize the surface of the GNFs without forming any iron oxide nanoparticles. The results show the absence of any iron oxide nanoparticles in the samples resulting in an improved electrocatalytic activity toward the ORR.

Addition of atomically dispersed iron on nitrogen functionalized graphene nanoflakes for catalyst application in alkaline medium

Ulrich Legrand, Jean-Luc Meunier, Dimitrios Berk

Plasma Processing Laboratory, Department of Chemical Engineering, McGill University

Abstract: A thermal plasma reactor is used to grow graphene nanoflakes (GNFs), a stack of 5 to 20 graphene sheets, by the thermal decomposition of methane. The GNFs are then functionalized with a solution of iron (II) phthalocyanine in the same thermal plasma reactor, making the catalyst synthesis a batch process. Iron phthalocyanine molecules are incorporated at the surface of the GNFs in order to make an atomic dispersion of iron, and turn the GNFs into active catalysts for the Oxygen Reduction Reaction (ORR). The characterization of the samples shows that the addition of nitrogen on the surface of the GNFs is improved after functionalization, and the nitrogen found at the surface of the samples is mostly under the form of pyrrolic nitrogen. The iron content is estimated to go up to 0.46 wt%, but the optimal samples showing the highest ORR performance have an iron content at 0.15 wt%.

1. Introduction

Catalysts are a major part of fuel cells, these energy conversion devices consuming hydrogen and oxygen and producing water, heat and electricity. The catalyst facilitates mostly the oxygen reduction reaction (ORR) at the cathode. Platinum based catalysts have outstanding performances [126,127] but have drawbacks based on the nature of the metal. Platinum is indeed rare and expensive, preventing the fuel cells to reach a world-wide market [128]. Platinum based catalysts also have the drawback of being easily poisoned by carbon monoxide [129].

Alternatives are studied to replace platinum by non-noble metal catalysts, based on cheap and abundant materials. In 1964 Jasinski observed that iron phthalocyanine were highly active in the ORR [80]. Iron phthalocyanine is a molecule where an atom of iron is surrounded by nitrogen atoms in a polycyclic ring. This molecule is able to reduce the oxygen in fuel cells but has the drawback of not resisting acidic and basic environments. Studies showed the advantage of creating catalytic sites by incorporating the iron phthalocyanine molecule in various carbon-based matrices resistant to both acidic and basic conditions [81,130,131], including graphene sheets [110,132]. These studies however generally use graphene oxide which is functionalized by wet chemical methods and then reduced in a pyrolysis step [133–135]. Graphene oxide, even in its reduced form, presents a large number of structural defects which renders the label of graphene itself questionable.

Another form of graphene, namely the graphene nanoflakes (GNFs), are formed through very high temperature homogeneous nucleation in plasma-based processes which eliminate the problem of oxidation/reduction based synthesis and the associate structural and purity problems. The GNF powders consist of particles corresponding to a stack of 5 to 20 graphene sheets, measuring approximately 100 by 100 nm, and presenting a very good crystallinity. First described by Pristavita *et al.* [114], the GNFs were demonstrated to be good candidates to support iron as a non-noble metal catalyst [113,136]. Previous attempts to create an atomic dispersion of iron on the GNFs surface were made by adding a functionalization step in the same thermal plasma reactor used for the synthesis of the nanoparticles [137]. Iron precursors were based on the vaporization of either iron powder or a ferrous solution; however the iron vapour generated at high temperatures preferentially formed iron oxide nanoparticles downstream of the flow when reaching a temperature of 1,800 K before being deposited on the GNFs surface. The resulting materials showed some

electrocatalytic activity in alkaline medium, but the expected atomic dispersion of iron catalytic sited was not obtained.

The present work focuses on the direct addition of iron (II) phthalocyanine solution in the thermal plasma conditions as a functionalization step to add effectively the catalytic sites on the GNFs surface without forming any iron oxide nanoparticles. Under appropriate thermal history conditions, it is expected that the phthalocyanine structure would keep the iron atom in its central position, thus preventing the iron to form iron oxide nanoparticles. The phthalocyanine structure would remain available to react with the surface of the GNFs under the highly reactive plasma environment.

The generated catalysts, made of nitrogen and iron functionalized GNFs (N-Fe/GNFs) are fully characterized to prove the effectiveness of the iron addition without the formation of iron oxide nanoparticles. The electrocatalytic activity of the samples is finally tested in alkaline solution to show the N/Fe-GNFs can be used as active catalysts for the ORR in fuel cells.

2. Materials and methods

2.1. Catalyst synthesis

The GNFs are grown following Pristavita *et al.* procedure [6], whereby a carbon source, methane gas, is decomposed by the argon thermal plasma in an inductively coupled plasma (ICP) torch at a temperature of approximately 10,000 K. Carbon atoms form nuclei under homogeneous nucleation and grow into well-crystallized graphitic nanoparticles when the plasma is cooled down to 3700 to 4900 K [28]. The high crystallinity of the GNFs comes from the axisymmetric conical shape of the thermal plasma, preventing gas recirculation as well as the formation of amorphous carbon. Then, the GNFs are deposited on the walls and

the bottom plate by thermophoretic force. Nitrogen is added using a small flow rate (0.1 slpm) during the GNFs growth, leading to nitrogen content up to 2 at% at the surface of the nanoparticles.

The iron functionalization step is performed by changing the gas feeding conditions, where the methane and nitrogen gases are stopped, and an iron (II) phthalocyanine solution is introduced in the argon-based thermal plasma reactor. The solution is made with iron (II) phthalocyanine powders (Sigma Aldrich) and distilled water at a concentration of 5 mg/mL. The solution is injected through a side window of the thermal plasma reactor located 9 cm downstream of the ICP torch nozzle in a colder region of the conical reactor. The droplets are carried by nitrogen gas at a flow rate of 5 slpm and are fed using a 20 mL stainless steel syringe from Chemyx where the flow rate is controlled by an electronic push-syringe. The liquid flow rate is chosen to be 1 or 5 mL/min in order to vary the quench rate of the liquid feed and its influence on maintaining the phthalocyanine structure.

The total volume of iron (II) phthalocyanine solution injected during the functionalization step is also studied. The total volume injected can have an impact on the total amount of functionalities added to the surface of the nanoparticles, potentially resulting on higher ORR performances for the resulting catalysts.

The pressure in the reactor, as well as the power delivered to the ICP torch were adjusted using two sets of coupled conditions: 20 kW/55.3 kPa and 25 kW/13.8 kPa. Extensive modelling of the temperature and flow fields in the reactor [138] indicated that both conditions exhibit similar temperature profiles: the plasma (generated in the ICP torch) enters the conical reactor at approximately 10,000 K to be cooled down to 300 K in the vicinity of the water-cooled walls and the bottom collecting plate. However, the two coupled conditions differ in their velocity profile. The plasma at 25 kW/13.8 kPa reaching a maximum velocity of 160 m.s⁻¹ presents velocities four times greater than the 20 kW/55.3

kPa [138]. The difference in these velocities implies that the time where the solution is vaporized and the phthalocyanine molecule is potentially decomposed is shorter for the 25 kW/ 13.8 kPa condition. The experimental conditions are summarized in Table 4-6.

Table 4-6: Experimental conditions of the N-Fe/GNFs synthesis.

Sample Name	Liquid flow rate (mL/min)	Pressure/Power Conditions	Total volume injected (mL)
	(1112)	Conditions	injected (iniz)
N/Fe-GNF1	1	20 kW/55.3 kPa	
N/Fe-GNF2	5		05
N/Fe-GNF3	1	25 kW/ 13.8 kPa	
N/Fe-GNF4	5		
N/Fe-GNF5	1	20 kW/55.3 kPa	
N/Fe-GNF6	5		10
N/Fe-GNF7	1	25 kW/ 13.8 kPa	
N/Fe-GNF8	5		

2.2. Physical characterization

After synthesis, the powders are collected and analysed. The N-Fe/GNFs are observed by Scanning Electron Microscopy (SEM) on a FEI Inspect F-50 FE-SEM and by Transmission Electron Spectroscopy (TEM) on a FEI Tecnai G2 F20 200 kV Cryo-STEM. The elemental composition of the N-Fe/GNFs is determined by X-ray Photoelectron Spectroscopy (XPS) on a Scientific K-Alpha XPS from Thermo Scientific using an

aluminium x-ray source on 400 µm spot size area. The total amount of iron contained in the N-Fe/GNFs has been determined by Neutron Activation Analysis (NAA) on the SLOWPOKE nuclear reactor, an Ortec GEM30185-P germanium semiconductor gamma-ray detector, an ortec DSPEC ProTM multichannel analyser, a Sartorius precision balance and the EPAA analysis software [139]. The NAA has been conducted at the SLOWPOKE Laboratory of the Institute of Nuclear Engineering located at École Polytechnique de Montréal. Raman spectroscopy was used to determine the graphitization of the samples and performed on an inVia Reflex confocal micro-Raman (Renishaw) having a laser emitting at 514.5 nm.

2.3. Electrochemical characterization

The electrocatalytic activity of the N-Fe/GNFs is studied through Rotation Disk Electrode RDE) technique. The catalysts are suspended in an ink that consists of the powder, a solvent made of 70 wt% of isopropyl alcohol and 30 wt% water, and a 5 wt% Nafion[©] solution purchased at Sigma Aldrich. After sonication for 1h in an ice bath, the ink is then deposited on a 5 mm diameter glassy carbon electrode to obtain a thin and homogenous deposit of 0.1 mg·cm⁻² of catalyst. The alkaline solution consists in a 0.1 M KOH solution having a pH of 13. The electrode is immersed in the alkaline solution and rotated at 1600 rpm when Linear Sweep Voltammetry (LSV) is performed against a silver/silver chloride (Ag/AgCl) reference electrode and a platinum wire counter electrode. The catalysts pass first through a conditioning protocol based on loops between -1 and +1 V at a scan rate of 500 mV·s⁻¹ under N₂ bubbling until the LSVs do not shown any variation. The aim of this process is to remove any impurities from the electrode surface and allow the maximum utilization of the electrocatalytic area [116]. The LSVs are then recorded under O₂ bubbling between +1 and -1 V, cathodic sweep, at a scan rate of 20 mV·s⁻¹ to evaluate the ORR performance. The contribution of the capacitive current is subtracted from the measurements by recording LSVs

under N_2 bubbling with the same conditions. The potential is converted from Ag/AgCl to Reversible Hydrogen Electrode (RHE) using Equation 1.

$$E_{RHE} = E_{Ag/AgCl} + E_{Ag/AgCl}^{0} + 0.059 \text{ pH}$$
 Equation 1

where $E_{Ag/AgCl}^{0}$ is the standard potential for Ag/AgCl electrode and equal to 0.1976 V.

3. Results and discussion

3.1. Chemical composition of the N/Fe-GNFs

The surface of the samples was analysed by XPS. From the spectra shown on Figure 4-10, the samples appear to be composed of carbon, nitrogen and oxygen with respective amounts summarized in Table 4-7. The presence of iron is not confirmed by XPS, probably due to the low amount close to the detection limit, which is 0.1 at%.

A closer inspection of the high resolution peaks of carbon, nitrogen and oxygen gives some insight on the chemical bonding in the samples. Carbon is mostly in its sp2 form, characteristic of the asymmetric XPS peak at 284.4 eV. Functionalities of nitrogen and oxygen are attached to the carbon, at respectively 286.0 and 287.5 eV [140,141]. The oxygen functionalities are involving C-O and C=O bonds, at 531.6 and 532.9 eV [142]. Also, some nitric oxide functionalities are found at 534.2 eV. The oxygen functionalities originate mainly from the water based solution, where water molecules are decomposed by the thermal plasma and form species which react with the surface of the deposited GNFs. Four different types of nitrogen functionalities are found in the N/Fe-GNFs [85]. Oxidized nitrogen is found at 402.2 eV and confirms the observation based on the oxygen peak. Quaternary nitrogen at 400.9 eV corresponds to atoms of nitrogen substituting an atom of carbon in the graphitic structure. Pyrrolic nitrogen at 399.9 eV is the type of nitrogen found in the phthalocyanine molecule and represents between 35 and 50% of the total nitrogen for the samples. Pyridinic nitrogen is

found at 398.9 eV. Both pyridinic and pyrrolic nitrogen have the potential to form catalytic sites. The nitrogen functionalities originate from the phthalocyanine molecules themselves, but also from the nitrogen gas used to carry the injected solution during the functionalization step.

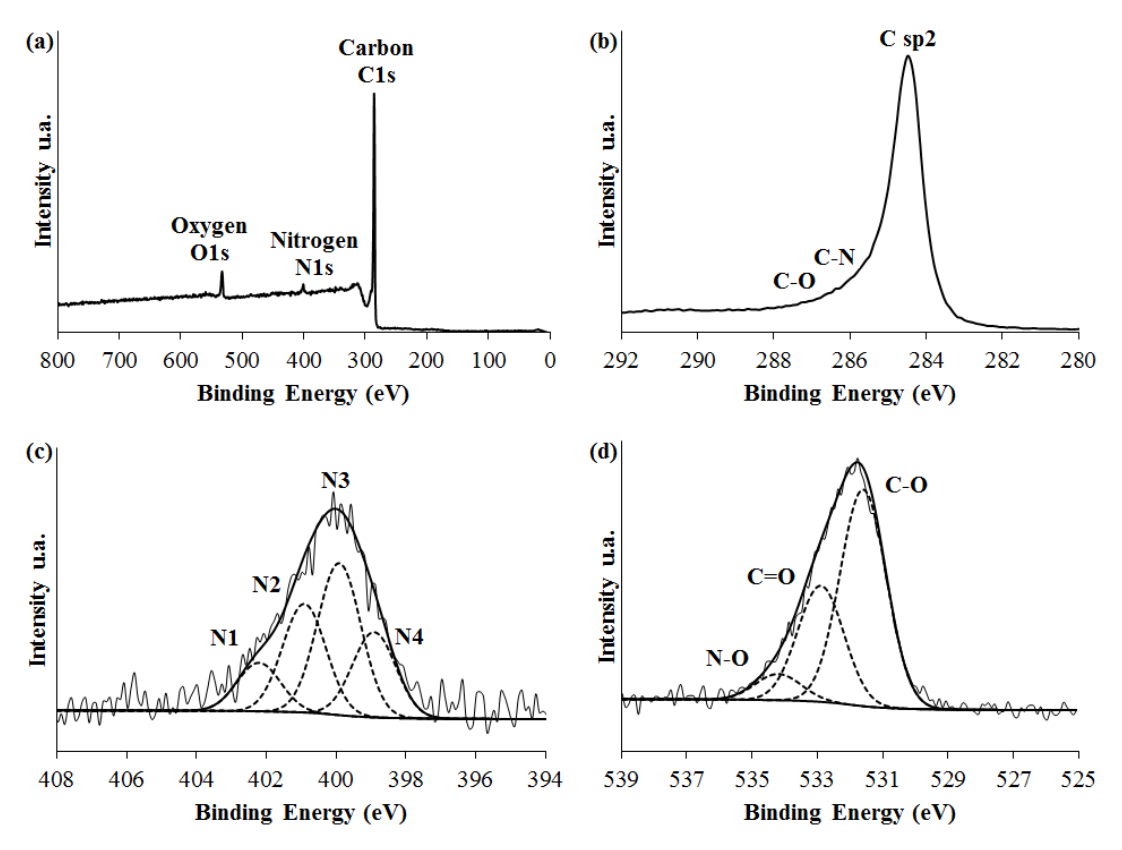


Figure 4-10: (a) Typical XPS survey obtained for N-Fe/GNF7. High resolution peaks of (b) carbon C1s, (c) nitrogen N1s, (d) oxygen O1s for the sample N-Fe/GNF7. N1, N2, N3 and N4 respectively correspond to oxidized, quaternary, pyrrolic, and pyridinic nitrogen.

By inspecting the elemental composition of the samples, it appears that the samples functionalized under the 25 kW/13.8 kPa conditions (N-Fe/GNF3,4,7,8) generally contain more nitrogen and oxygen functionalities than the samples functionalized with the 20 kW/55.3 kPa conditions (N-Fe/GNF1,2,5,6). This trend has been already confirmed by previous studies and come from the much shorter transit time of the flow stream between the higher temperature plasma region and the deposited GNFs of the 25kW/13.8 kPa conditions. This allows more reactive species to reach the deposited GNFs and then a higher

functionalization rate [138]. However, the elemental composition also shows that the samples functionalized with 10 mL of iron (II) phthalocyanine have smaller amounts of nitrogen and oxygen compared to the samples functionalized with 5 mL of solution. This observation contradicts the intuitive hypothesis that adding a higher volume of solution would increase the level of functionalization. It however goes along the influence of the temperature and flow profiles modifications generated by the phthalocyanine solution injected.

Table 4-7: Elemental composition of the N-Fe/GNFs surface.

Samples	Carbon (at%)	Nitrogen (at%)	Oxygen (at%)
N-Fe/GNF1	90.87	2.96	6.17
N-Fe/GNF2	89.96	4.71	5.33
N-Fe/GNF3	87.40	4.76	7.83
N-Fe/GNF4	90.55	4.29	5.16
N-Fe/GNF5	93.28	1.92	4.80
N-Fe/GNF6	96.12	1.13	2.75
N-Fe/GNF7	91.63	2.72	5.65
N-Fe/GNF8	90.17	4.30	5.53

The iron amount being too low to be detected by XPS, NAA has been used to determine the total weight of iron contained in the N-Fe/GNFs. Based on the previously established elemental composition, the iron concentration has been converted from wt% to at%. This conversion requires to assume the surface composition and the bulk composition are identical; this may not be completely true because functionalization occurs mostly on the surface of the nanoparticles. However, the depth of penetration of the x-rays used in the XPS

technique (~5-10 nm) being higher than the thickness of the GNFs and the small difference in molecular weight between carbon, nitrogen, and oxygen, the conversion is estimated to give acceptable values of iron concentration in at%. These values are lower than or equal to 0.1 at%, confirming the impossibility to detect iron by XPS. It has to be noted that the described process presents a low iron incorporation level. Indeed, the theoretical amount of iron which could be incorporated is 2.45 wt% for the samples N-Fe/GNF1,2,3,4 and 4.9 wt% for the samples N-Fe/GNF5,6,7,8 based on a usual batch of GNFs weighing 200 mg. Only 10 to 15 wt% of the injected iron is found in the final samples.

Table 4-8: Iron level in the N-Fe/GNFs and conversion to an elemental composition.

Samples	Fe concentration (wt%)	Converted concentration (at%)
N-Fe/GNF1	0.17	0.04
N-Fe/GNF2	0.14	0.03
N-Fe/GNF3	0.15	0.03
N-Fe/GNF4	0.39	0.09
N-Fe/GNF5	0.06	0.01
N-Fe/GNF6	0.16	0.04
N-Fe/GNF7	0.17	0.04
N-Fe/GNF8	0.46	0.10

3.2. Observation of the N/Fe-GNFs

The N-Fe/GNFs are observed using electron microscopy, and the sample containing the highest amount of iron, N-Fe/GNF8, is represented on Figure 4-11. The samples contain no amorphous carbon, which typically exhibits a cauliflower-like structure [118], this being confirmed by the shape of the carbon peak in XPS. Also, the absence of iron oxide nanoparticles has been confirmed in all of the observed samples, mostly by TEM. This observation confirms the hypothesis that the iron phthalocyanine molecule can be incorporated to the GNFs without being decomposed and forming sub-products such as amorphous carbon and iron oxide nanoparticles.

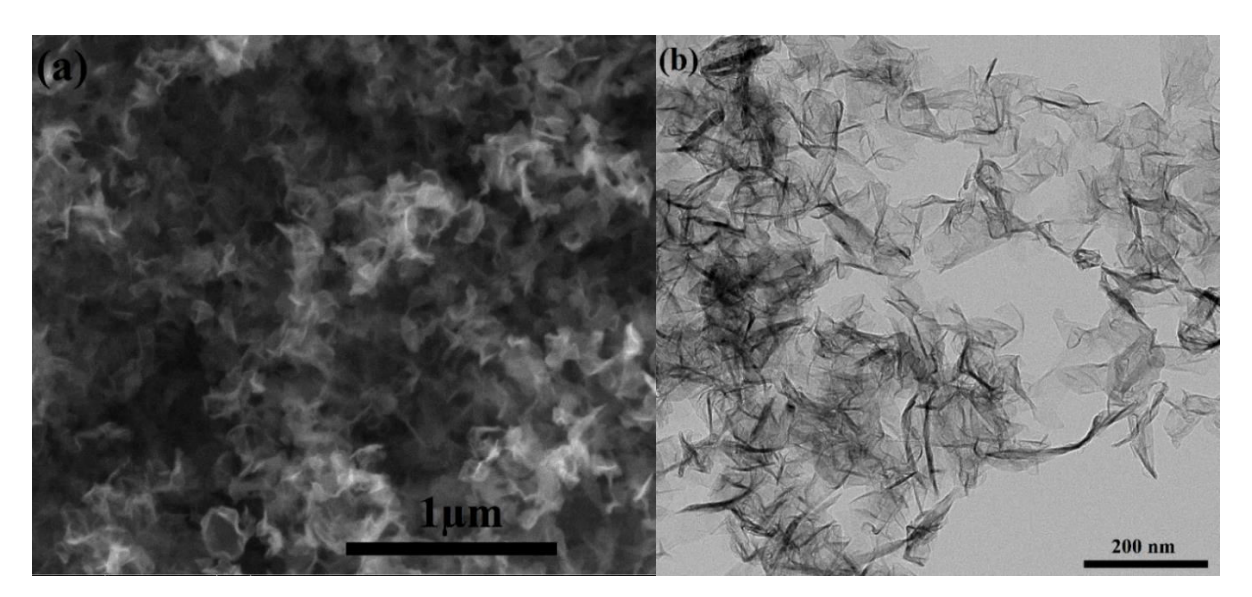


Figure 4-11: Observation of the sample N-Fe/GNF8 under (a) SEM with a bar scale of 1 μ m and (b) TEM with a bar scale of 200 nm.

3.3. Crystallinity of the samples

The crystallinity of the N-Fe/GNFs is evaluated by Raman spectroscopy. A typical Raman spectrum for the sample N-Fe/GNF3 is shown in Figure 4-12. There are three peaks of interest in the spectrum [143]: (i) the D peak at 1350 cm⁻¹ which denotes the amount of defects in the graphitic structure or the carbon in sp3 conformation, (ii) the G peak at 1570

cm⁻¹ which is related to the graphitized carbon in conformation sp2 and (iii) the G' peak at 2700 cm⁻¹ whose intensity and sharpness increases with increasing number of graphene sheets in the stack. In addition of these peaks, the D' peak can be observed at 1630 cm⁻¹, which is a shoulder of the G peak and is also related to the defects content of the graphitic structure. All samples display no signal at 1200 and 1500 cm⁻¹ corresponding to the I and D" peaks, respectively, related to hydrocarbons attached to the graphitic structure, distortions in planes, and amorphous sp2 carbon [144]. Thus the intensity and area under the D and G peak can directly be determined without the deconvolution of the D-G region.

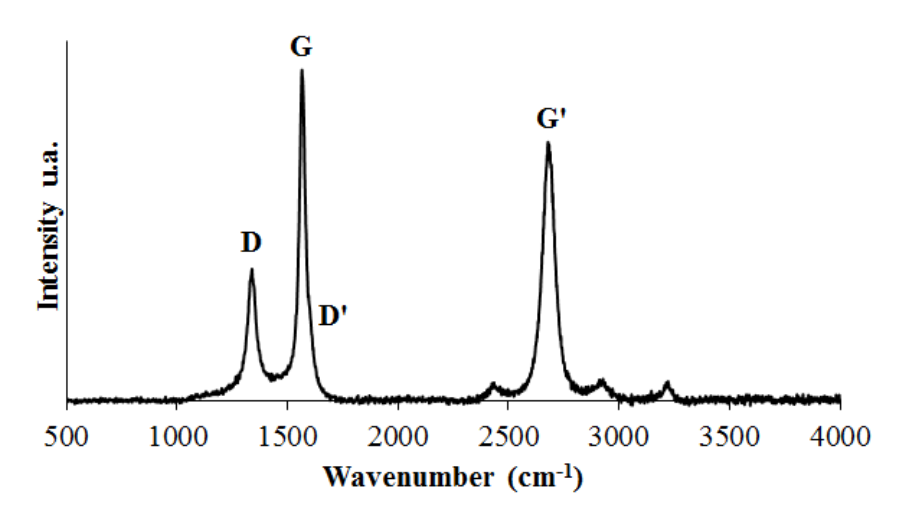


Figure 4-12: Raman spectrum of the sample N-Fe/GNF3.

The Raman spectra can give quantitative values to evaluate the graphitization of the samples. Established by Larouche *et al.* [120], the graphitic indices are calculated based on the intensity and area under the curve of the D, G and G' peaks. The purity of the samples is equivalent to the intensity ratio of the G to D peaks. A G to D ratio equal or higher than 1 denotes a material with a higher amount of graphitized carbon than defects. L_a is proportional to the ratio of the area under the G to D peaks and refers to the length of the smallest defect-free crystallite. L_{eq} is proportional to the ratio of the area under the G' to D peaks and

corresponds to the length of crystallites linked by curvature. The formulas and values of the graphitic indices are summarized in Table 4-9.

Table 4-9: Graphitic indices for the N-Fe/GNFs calculated from the Raman spectra. The formulas have been developed by Larouche *et al.* [120].

	Purity (± 0.2)	La (± 0.4 nm)	Leq (± 3.0 nm)
Formula	$I_{\rm G}/I_{\rm D}$	$4.4 \times A_G/A_D$	$8.8 \times A_G/A_D$
GNFs	2.8	8.8	28.2
N-Fe/GNF1	2.6	7.6	21.1
N-Fe/GNF2	2.5	7.4	19.9
N-Fe/GNF3	2.5	7.9	21.3
N-Fe/GNF4	2.5	7.8	20.5
N-Fe/GNF5	2.6	7.8	21.9
N-Fe/GNF6	2.5	8.2	22.6
N-Fe/GNF7	2.7	8.2	22.9
N-Fe/GNF8	2.5	7.6	20.6

After functionalization the N-Fe/GNFs have lower graphitic indices, indicating the addition of defects on the graphitic structure. These defects originate from the incorporation of the nitrogen and oxygen functionalities on the surface of the GNFs; however, the values of the purity, L_a and L_{eq} are in a close range for all of the N-Fe/GNFs, making difficult the correlation between experimental conditions and amount of functionalities added to the GNFs by Raman spectroscopy in this study. Even if the values of the graphitic indices decrease after the functionalization step, these values remain higher than most of different graphitic

materials tested by Larouche *et al.* [120], especially those based on graphene oxide and reduced graphene oxide. This result indicates that the GNFs, functionalized or not, are and remain well-crystallized due to the homogeneous nucleation method used to grow the structures and to add the functionalities from plasma activated species in the gas phase.

3.4. Electrocatalytic activity of the N/Fe-GNFs

The N-Fe/GNFs are tested through the RDE technique to evaluate their respective electrocatalytic activity, in terms of onset potential, half-wave potential and limiting current density, measured at 0.4 V vs RHE. The onset potential is the potential where the current density starts to decrease and is no longer equal to 0. The onset potential for platinum based catalysts is generally between 0.8 and 0.9 V vs RHE, while the onset potential of non-functionalized graphene nanoflakes is closer to 0.7 V vs RHE. The half-wave potential is the potential at which the current density is equal to half of the limiting current density and denotes the sharpness of the LSV, related to the kinetics of the ORR. The limiting current density is directly proportional to the rate of reduction of oxygen. The LSVs of some typical samples compared to non-functionalized GNFs are shown in Figure 4-13, while the numerical values of onset potential, half-wave potential and limiting current density are summarized in Table 4-10.

The overall ORR performances of the N-Fe/GNFs remain in a close range of values. The onset potential values of the N-Fe/GNFs are comprised between 0.73 and 0.74 V vs RHE, which shows an improvement compared to the non-functionalized GNFs. However, these values are still around 0.1 V lower than the onset potential of platinum based-catalyst. Due to close range of onset and half-wave potential, the best parameter to compare the ORR performances of the N-Fe/GNFs is the limiting current density. The sample showing the best performance is N-Fe/GNF3, with a limiting current density of -2.40 mA·cm⁻². From the

composition of the N-Fe/GNFs, this sample is containing one the highest amount of nitrogen with a particular strong proportion of pyrrolic nitrogen. Aside from the nitrogen level, N-Fe/GNF3 show a low level of iron (0.15 wt%), indicating that optimal iron content is not always the highest, as several studies suggest [106]. N-Fe/GNF3, and the other samples functionalized with the 25 kW/13.8 kPa have globally better performances than the one functionalized with the 20 kW/55.3 kPa and correspond to samples which have a higher amount of functionalities, as observed in the chemical composition section. The flow rate had no real impact on the composition of the samples, and the same observation can be done on the ORR performance of the catalysts. A lower volume of solution was related to higher functionalization rates, resulting in slightly better ORR performance for the samples N-Fe/GNF1,2,3,4.

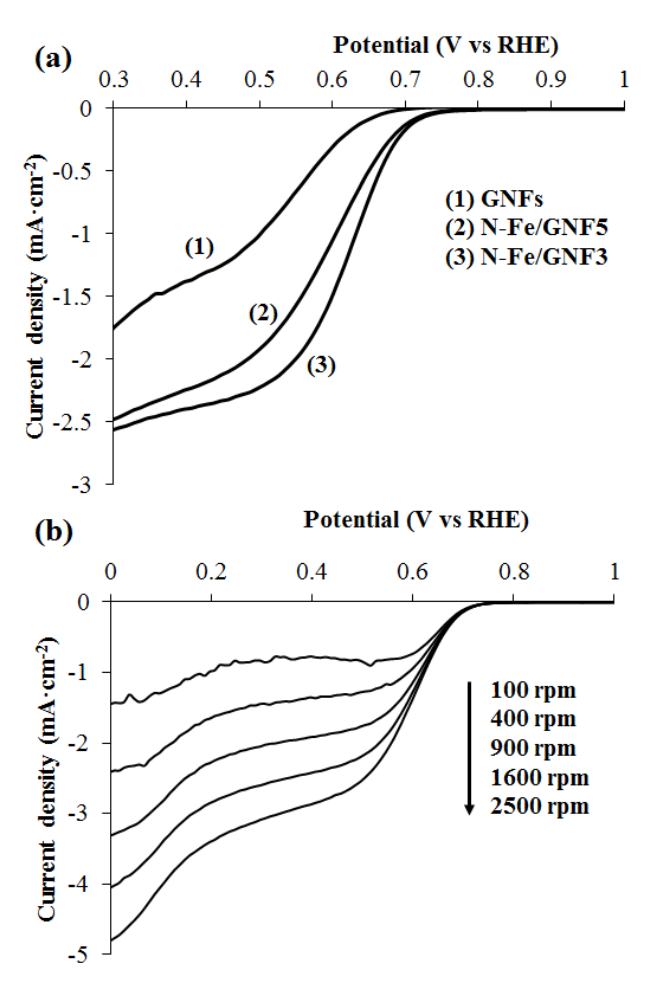


Figure 4-13: (a) LSV of two typical catalysts compared to the non-functionalized GNFs. (b) LSV at rotation rates between 100 and 2500 rpm for the sample N-Fe/GNF3.

Table 4-10: Quantitative evaluation of the electrocatalytic activity of N-Fe/GNFs through the

onset potential, the half-wave potential and the limiting current density.

Sample	Onset potential (V vs RHE)	Half-wave potential (V vs RHE)	Limiting current density @ 0.4 V (mA.cm-2)
GNFs	0.66	0.55	-1.38
N-Fe/GNF1	0.73	0.62	-2.35
N-Fe/GNF2	0.73	0.59	-2.31
N-Fe/GNF3	0.74	0.62	-2.40
N-Fe/GNF4	0.73	0.62	-2.27
N-Fe/GNF5	0.73	0.60	-2.25
N-Fe/GNF6	0.74	0.61	-2.34
N-Fe/GNF7	0.73	0.60	-2.38
N-Fe/GNF8	0.74	0.63	-2.23

For the sample showing the highest ORR performance, N-Fe-GNF3, the number of electron transferred to the ORR can be evaluated by varying the electrode rotation rate when recording the LSV under oxygen bubbling. The relation between the number of electrons transferred and electrode rotation rate is established following the Koutecky-Levich formula, shown in Equations 2 and 3:

$$\frac{1}{j} = \frac{1}{B\omega^{1/2}} + \frac{1}{j_K}$$
 Equation 2

$$B = 0.62 nFC_0 D_0^{2/3} v^{-1/6}$$
 Equation 3

where ω is the electrode rotation rate, j_K is the kinetic current, n is the number of electrons transferred to the ORR, F is the Faraday constant, C_0 is the bulk concentration of oxygen in solution, D_0 is the diffusion coefficient of oxygen and υ is the kinematic viscosity of the 0.1 M KOH solution. The values taken for the parameters of the Koutecky-Levich formula are typical from a 0.1 M KOH solution [145].

The number of electrons transferred to the ORR for N-Fe/GNF3 can be evaluated at different potentials. In the 0.2 to 0.4 V vs RHE, the number of electrons is equal to 2.4 while it is equal to 4.6 close to 0.0 V vs RHE. It indicates that N-Fe/GNF3 reduces the oxygen molecule mainly following a 2-electron path in the 0.2 to 0.4 V vs RHE, with hydrogen peroxide as an undesirable intermediate [146], while the 4-electron path occurs closer to 0.0 V vs RHE.

4. Conclusion

Graphene nanoflakes have been grown and functionalized with iron (II) phthalocyanine in a batch process in thermal plasma conditions. The phthalocyanine molecules have successfully been incorporated on the GNFs surface to create catalytic sites based on the atomic dispersion of iron. Previous attempts to atomically incorporate iron by thermal plasma lead to the formation of iron oxide nanoparticles, but the method used in the present study showed no presence of iron oxide nanoparticles. The effective presence of iron has been confirmed by NAA, at amounts lower than the detection limit of the XPS technique. All of the functionalized GNFs exhibit a very good crystallinity through the functionalization step. The resulting catalysts see their overall ORR performances increase after the addition of iron (II) phthalocyanine, the best results being observed for 0.15 wt% of iron in the sample.

Chapter 5 Sulphur functionalization of the Graphene Nanoflakes for non-metal catalyst applications

Part I Addition of sulphur to graphene nanoflakes using thermal plasma for oxygen reduction reaction in Alkaline Medium

This section presents an article that has been published in the journal *Plasma*Processing and Plasma Chemistry, having for reference:

U. Legrand, J.-L. Meunier, D. Berk, Addition of sulphur to graphene nanoflakes using thermal plasma for oxygen reduction reaction in alkaline medium, Plasma Chem. Plasma Process., 1-16, 2017.

The work has been conducted, analyzed and written by U. Legrand (Ph.D. candidate), while Dr. J.-L. Meunier and Dr. D. Berk provided supervision and reviewing of the manuscript. The GNFs have proven to be effective non-noble metal catalyst toward the ORR in alkaline medium after iron functionalization in the thermal plasma reactor. From that, it was natural to test the GNFs as non-metal catalyst toward the ORR. In order to achieve this objective, sulphur is injected in the thermal plasma during the functionalization step in the form of liquid carbon disulphide for the incorporation of sulphur functionalities at the surface of the GNFs. An unexpected result was that sulphur functionalities appears in the form of sulphur-based plasma polymer partially covering the GNFs, as well as atoms of sulphur incorporated to the graphitic structure and orthorhombic solid sulphur. Although, the functionalized GNFs have an improved electrocatalytic activity toward the ORR, they do not reach the performances of the iron based catalyst generated previously.

Addition of sulphur to graphene nanoflakes using thermal plasma for oxygen reduction reaction in Alkaline Medium

Ulrich Legrand, Jean-Luc Meunier, Dimitrios Berk

Plasma Processing Laboratory, Department of Chemical Engineering, McGill University

Abstract: A batch process is developed to generate sulphur functionalized graphene nanoflakes (S-GNFs), corresponding to nanoparticles of stacked graphene. The growth and functionalization of the catalysts are done in a single thermal plasma reactor. The GNFs are first grown through the decomposition of methane in the thermal plasma volume followed by homogeneous nucleation of the nanoparticles in the well-controlled recombining plasma stream allowing the 2-dimensional evolution of the nanoparticle morphology. The precursor feeding conditions are then changed to liquid carbon disulphide in order to generate sulphurbased functional groups on the nanoparticles. The plasma conditions and carbon disulphide injection are varied, and samples with tuneable amount of sulphur between 4 and 28 at% are obtained. The functional groups generated include polythiophene plasma polymer partly covering the GNFs, sulphur functionalities implemented directly on the graphitic structure, and traces of orthorhombic sulphur. The S-GNFs exhibit higher electrocatalytic activity toward the oxygen reduction reaction in alkaline medium for the samples containing the highest amounts of sulphur.

1. Introduction

Fuel cells are energy conversion devices based on the reversed hydrolysis of water through which hydrogen and oxygen are consumed to produce heat, electricity and water. One of the most efficient fuel cells is the alkaline fuel cell (AFC) which potentially has a conversion rate up to 70% [74]. The major limiting factor of the fuel cells are the slow kinetics of the oxygen reduction reaction (ORR) at the cathode [75]. Platinum and platinum-alloys based catalysts exhibit the best performances in reducing the oxygen, but they show

major disadvantages due to high cost, low availability, and poisoning by carbon monoxide [147,148]. One current research trend is to reduce the amount of platinum needed in the catalyst while providing similar performance. Alternatives for new types of catalysts are also being investigated with the objective of lowering the price while achieving similar or better performances. Great advances have been made on non-noble metal catalysts, where platinum is being replaced by a cheaper metal which is either dispersed at the atomic level or as metal oxide nanoparticles [78,103,105,106].

Metal-free catalysts also exhibit interesting properties for the ORR. They are typically generated through the functionalization of graphene sheets with elements such as phosphorus, boron, nitrogen, or sulphur [86–88,149]. The addition of these elements in the form of functional groups on the graphene structure aims to modify the electronic charge distribution and create local catalytic sites favourable to the ORR [89]. The sulphur functionalization is generally achieved by adding thiophene structures to the graphene, where thiophene is a heterocyclic compound with one atom of sulphur and four atoms of carbon [150].

Graphene materials are good candidates to support catalytic sites in both non-noble metal and metal free catalysts because of their high electrical conductivity and resistance to both acidic and basic environments. However, most of the studies use graphene oxide as a starting material, which is functionalized and reduced [86,87,151]. Graphene oxide, even in its reduced form, shows very high amounts of defects, questioning the label of graphene itself. The present study employs a high purity material, the graphene nanoflakes (GNFs) developed in 2011 by Pristavita *et al.* [6]. GNFs are the product of the methane decomposition by an argon thermal plasma in an axisymmetric conical reactor and are described as a stack of 5 to 20 graphene sheets measuring approximately 100 by 100 nm. The geometry of the reactor prevents gas recirculation which typically leads to uncontrolled

particle nucleation and growth history, as well as the formation of amorphous carbon [114]. Key aspects of the graphene formation besides a rigorous control of the fluid dynamics is a control of longer residence times in the homogeneous nucleation window allowing the crystalline critical cluster to grow in a 2-dimensional pattern. Nucleation and growth modelling of the carbon clusters correlate very well with nucleation and growth dynamics following a crystalline critical cluster that fixes the thickness of the graphene (typically around 10 atomic layers), followed by 2-D growth of this cluster from carbon diffusion generating typically 100 nm sheet length scales [28]. Experimental powders collected follow very well these modelling evaluations, while the purity of the powders both in chemistry and morphology correlates well with the constant thermal history achieved in the reactor whatever the flow streamline being followed. The GNF powders generated are depositing on the walls as a very open and porous structure where they remain available for functionalization. Such chemical functionalization is achieved in the same reactor and batch process through a change of the plasma chemistry by varying the precursor being fed. Also of importance is a proper use of the thermal plasma recombination time scales allowing the availability of exited species within the GNF powder bed [138]

GNFs have already been successfully functionalized with tuneable amounts of oxygen, nitrogen and iron in previous studies. The addition of oxygen between 0 and 14 at% has led to the control of the hydrophilicity of the GNFs [138] while the addition of nitrogen and iron showed that GNFs are an appropriate material to support catalytic sites for the ORR in the case of a non-noble metal catalyst [9,113]. In the present paper, the addition of sulphur groups to the GNFs is first demonstrated using the same thermal plasma route. We also show these functionalized GNFs can act as effective metal-free catalyst for the ORR. The sulphur functionalization step is done by injecting liquid carbon disulphide in the argon thermal plasma to generate reactive species which should interact with the deposited GNFs.

The present paper describes in detail the operating conditions for getting the sulphur functionalized GNFs (S-GNFs). A study based on thermodynamic considerations is first conducted to evaluate the feasibility of the method. The structure and elemental composition of the resulting material are characterized. Finally, the ORR performance of the S-GNFs is also tested through the electrocatalytic activity and the number of electrons transferred during the ORR.

2. Experimental methods

2.1. Catalyst synthesis

GNFs are produced following Pristavita et al's procedure [6] using methane as a carbon source which is decomposed within an argon thermal plasma. The argon plasma is generated by an inductively coupled plasma (ICP) torch from TEKNA (TEKNA PL35-ICP) with a constant plate power of 20 kW. The ICP torch is connected to a water-cooled conical reactor as shown in Figure 5-1. The conical expansion has an opening angle of 14°, an axial length of 50 cm, and an internal pressure of 55.3 kPa. An annular manifold is used for exit gas pumping in order to maintain a 2-dimensional symmetry of the flow pattern as well as minimizing recirculating fluxes. This 2D stagnation-point flow geometry also enables very good correlation between the experimental system and computer fluid dynamics modelling of the reactor. Such modelling is also shown in Figure 5-1 with typical temperature profiles during the GNF nucleation step, and the mapping of the GNF homogeneous nucleation field. As one can see in Figure 5-1, the conditions indicated above generate an argon plasma reaching high temperatures, up to 10,000 K in the plasma core, and high enthalpies, between 10³ and 10⁵ kJ/kg. During the GNF nucleation phase, 1 slpm of methane is injected in the core of the plasma with an injection probe, and the molecules are instantaneously decomposed into carbon and hydrogen atoms when entering the thermal plasma. Carbon

atoms form small nuclei and grow into the GNFs in a narrow temperature window found through modelling to start at roughly 4,900 K and end around 4,200 K [28]. The fully grown nanoparticles are then deposited on the walls and the bottom plate of the reactor, driven by thermophoretic force.

The addition of sulphur to the graphitic structure is done as a post-processing step in the same reactor by changing gas feeding conditions. Methane is switched off and pure carbon disulphide (CS₂) is fed through the injection probe of the ICP torch, carried by the argon probe flow (4.5 slpm). The injection of liquid CS₂ is performed using a stainless steel syringe from Chemyx, the flow rate being controlled by a Nexus 3000 pump. Carbon disulphide was chosen over hydrogen sulphide (H₂S) and other sulphur compounds because it is not corrosive and it is very volatile. Also, the CS₂ molecule containing only carbon and sulphur atoms does not introduce other impurities during the functionalization step towards a final catalyst.

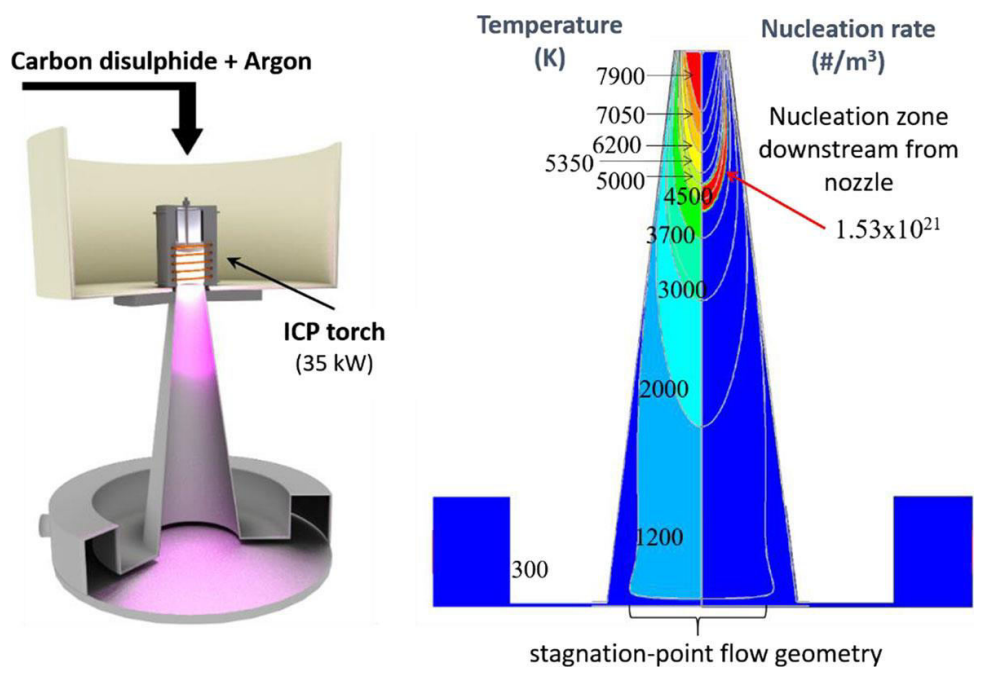


Figure 5-1: Left: Overall ICP thermal plasma reactor geometry using a conical expansion for controlling the flow patterns and the location of the nanoparticle nucleation zones, and a pumping manifold for axial gas exhaust in a stagnation-point flow geometry. Right: Modelling results of typical temperature profiles (left side) and the narrow zone of graphene nucleation (right side, red mapping) [28].

Various parameters are evaluated during the functionalization step. Two combined conditions are tested for the power delivered to the ICP torch and the pressure in the reactor: 20 kW/ 55.3 kPa and 25 kW/ 13.8 kPa. These two pairs of power-pressure have been studied through modelling evaluation of temperature profiles and flow fields in the geometry of the reactor. The temperature profiles are quite similar for the two conditions, going from 10,000 K within the ICP torch to 300 K close to the water-cooled walls and bottom plate of the reactor. However, the main difference of these conditions remains in the velocity profiles, and the resulting residence times in hot regions. Indeed, the 20 kW/ 55.3 kPa case leads to velocities up to 40 m/s while the maximum velocities are four times greater in the 25 kW/ 13.8 kPa case, going up to 160 m/s [138]. The change in the velocity profiles is believed to make a difference in the generation and more importantly the transport of reactive species, and so the functionalization of the GNFs itself. The other parameters which have been varied are the flow rate of injection of CS₂, as well as the exposure time of the GNFs to the sulphur based reactive species. The overall tested conditions for the sulphur functionalization step are summarized in Table 5-1.

Table 5-1: Experimental conditions of the sulphur functionalization step.

Sample		CS ₂ flow	Exposure	Total volume injected
name	Power/pressure	(mL/min)	time (min)	(mL)
S-GNF1	20 kW / 55.3 kPa	1.0	5	5
S-GNF2	25 kW / 13.8 kPa		J	
S-GNF3	20 kW / 55.3 kPa	0.5	10	5
S-GNF4	25 kW / 13.8 kPa			
S-GNF5	20 kW / 55.3 kPa	0.2	10	2
S-GNF6	25 kW / 13.8 kPa	3		_
S-GNF7	20 kW / 55.3 kPa	0.2	2	0.4
S-GNF8	25 kW / 13.8 kPa			

2.2. Physical characterization

The S-GNFs powders have been characterized to investigate structural properties and elemental composition of the nanoparticles. Scanning Electron Microscopy (SEM) was performed on a FEI Inspect F-50 FE-SEM as a qualitative analysis on the appearance of the samples. The graphitization level of the graphitic structure was measured by Raman spectroscopy on an inVia Reflex confocal micro-Raman (Renishaw) with a laser emitting at 514.5 nm. X-Ray Photoelectron Spectroscopy (XPS) was made on a Scientific K-Alpha XPS system from Thermo Scientific using an aluminium X-ray source on analysed areas of 400

 μ m spot size. X-Ray Diffraction (XRD) was performed on a Brucker D8 Discovery X-Ray Diffractometer, with a VANTEC detector, and having a copper K α source.

2.3. Electrochemical characterization

The electrocatalytic activity of the S-GNFs in the ORR is tested using Rotating Disk Electrode (RDE) technique. The electrodes are prepared by drying 19.6 μL of a catalyst ink made of water, ethanol, 5wt% Nafion[©] solution and the tested sample on a 5 mm glassy carbon tips. The catalyst loading on the electrode tips is kept constant at 0.1 mg·cm⁻². The medium is a 0.1 M potassium hydroxide solution (KOH) at room temperature for a pH of 13. The set-up consists in three electrodes immerged into the alkaline solution and connected to a potentiostat, the electrodes being the working electrode, where the catalysts are deposited, a platinum wire counter electrode and a saturated silver/silver chloride (Ag/AgCl) reference electrode.

Linear sweep voltammetry (LSV) is performed under O_2 bubbling, saturating the electrolyte with dissolved oxygen, from +1 to -1V, at a scan rate of 20 mV·s⁻¹ cathodic sweep. The contribution of capacitive current to the ORR is suppressed to the final measurement through the recording of LSV under N_2 bubbling at the same conditions. Initially, the deposited samples go through a conditioning procedure by applying repeated cycles between +1 and -1V, at a scan rate of 500 mV·s⁻¹ under N_2 bubbling until the LSV do not vary from one to the other. The potential is converted from the Ag/AgCl reference to the reversible hydrogen electrode (RHE) using Equation 1.

$$E_{RHE} = E_{Ag/AgCl} + E_{Ag/AgCl}^{0} + 0.059 \text{ pH} \qquad \qquad \text{Equation 1}$$

where $E^0_{Ag/AgCl}$ is the standard potential for Ag/AgCl electrode and equal to 0.1976 V.

3. Results and discussion

3.1. Thermodynamic considerations

The feasibility of the sulphur functionalization of the GNFs has been initially studied through equilibrium thermodynamic considerations. The software Factsage has been used to model the decomposition of the CS₂ molecule when introduced in the core of the argon thermal plasma and some resulting species have been tracked through the cooling of the system down to room temperature. The temperature range goes from 300 to 10,000 K, with the nature and amount of the different species being indicated in Figure 5-2.

As expected, the carbon disulphide molecule is mostly decomposed to carbon and sulphur atoms at 10,000 K. As the temperature decreases, the carbon atoms form larger molecules (C₃, C₄, C₅), which can be attributed to the formation of nuclei and leading to the growth of graphitic material similar to the GNFs. Atomic sulphur, as well as CS, S₂, and CS₂ molecules have relatively high concentrations at lower temperature (~2 000 K), suggesting the possibility that these reactive species reach the GNFs in order to functionalize the nanoparticles. Also, it appears that sulphur atoms form clusters at low temperature (~1 000 K) resulting in orthorhombic sulphur, which could compete with the functionalization of the GNFs.

300 4300 5300 8300 9300 1300 2300 3300 6300 7300 1.E+00 1.E-01 S C 1.E-02 1.E-03 Amount (mol) 1.E-04 1.E-05 1.E**-**06 1.E-07 CS $\mathbf{C_2}$ 1.E-08 $\mathbf{S_2}^{-}$ 1.E-09 1.E-10 S(ortho) C(graphite) C_5 C_4 CS_2 C_3

Temperature (K)

Figure 5-2: Equilibrium thermodynamic evaluation of the nature and amount of species generated from the decomposition and recombination of carbon disulphide in an argon thermal plasma as a function of temperature (0.017 moles of CS₂ in 2.54 moles of Ar).

The validity of such equilibrium thermodynamic model can be questioned when considering the particularly reactive environment of a thermal plasma generating both excited and ionic species. However, this model gives an insight that sulphur-based excited species can effectively be present in the plasma recombination zone located roughly at temperatures below 4000 K, and possibly remain active downstream to the GNF powders for some efficient functionalization by sulphur. The equilibrium model also provides information on the possible presence of additional graphitic material as well as solid sulphur at the end of the functionalization step.

3.2. Elemental composition of the S-GNFs

The S-GNFs are characterized by XPS to determine the elemental composition at the surface of the samples, typical results being shown on Figure 5-3. All of the samples are made of carbon, sulphur and oxygen in various atomic percentages, as seen in Table 5-2. For all of the samples, the oxygen level is between 1 and 2.5 at%, these amounts being also found in the non-functionalized GNFs and correspond to powder oxidation following the contact with air. The overall elemental composition of the S-GNFs depends on the experimental conditions used to synthesize the samples. Indeed, the amount of atomic sulphur reaches values between 23 and 28 at% when the total volume of carbon disulphide injected during the functionalization step is 10 mL, while 0.4 mL of injected liquid leads to an amount of 4 at%. This suggests that the amount of sulphur contained in the samples can be tuned using the total amount of CS₂ injected. Also, the samples functionalized under the power/pressure conditions of 13.8 kPa/25 kW (S-GNF2,4,6,8) have a lower content of sulphur than the one treated under the 55.3 kPa/20 kW conditions (S-GNF1,3,5,8).

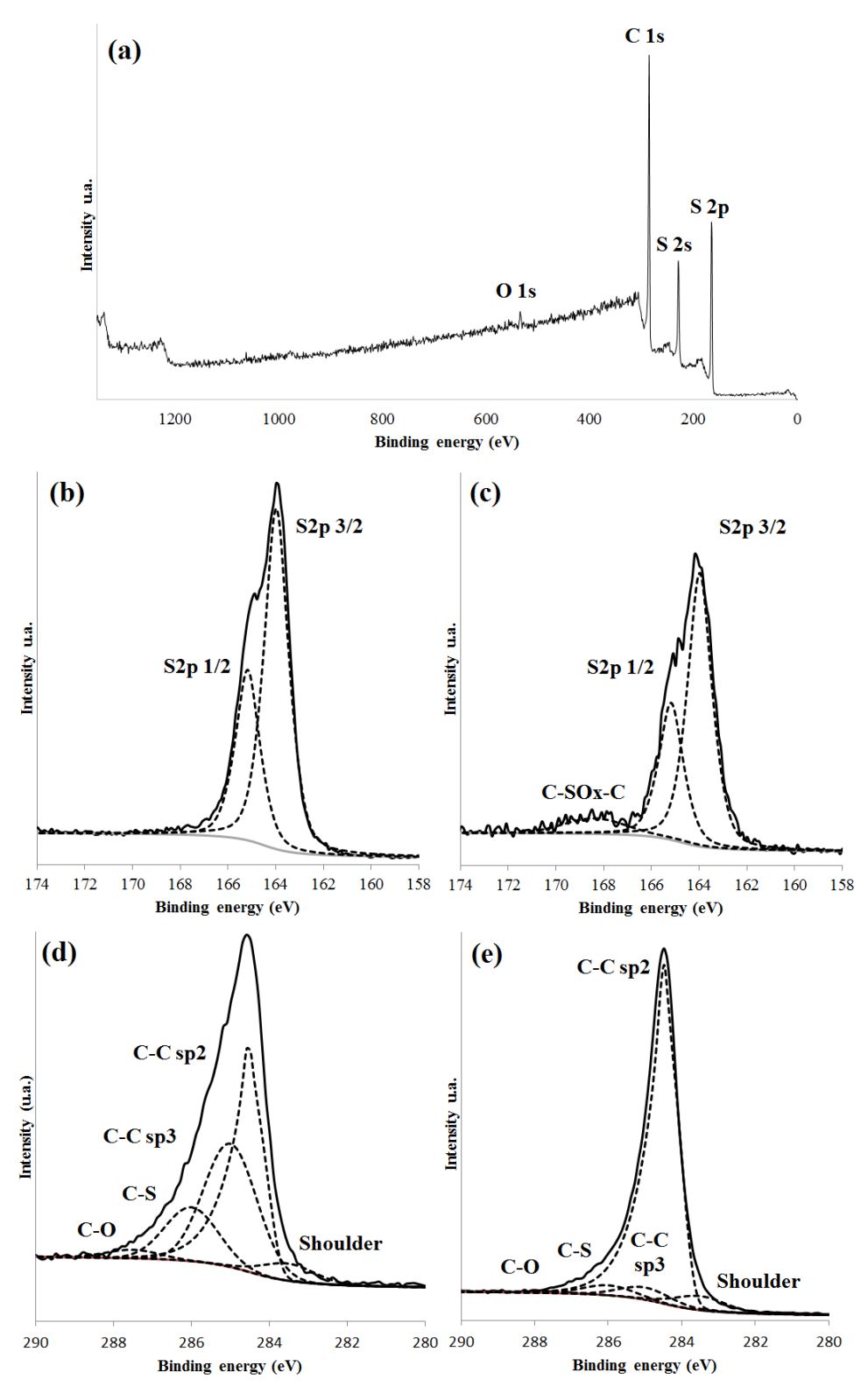


Figure 5-3: XPS spectrum of the S-GNFs. (a) Survey of the sample S-GNF1. High resolution sulphur S2p peak of (b) S-GNF1 and (c) S-GNF7. High resolution peak of carbon C1s of (d) S-GNF1 and (e) S-GNF7.

Table 5-2: Elemental composition of the S-GNFs.

Sample	At% C	At% S	At% O
S-GNF 1	74.07	23.96	1.97
S-GNF 2	74.48	23.40	2.11
S-GNF 3	69.61	28.45	1.94
S-GNF 4	74.94	23.22	1.84
S-GNF 5	81.00	16.59	2.41
S-GNF 6	86.98	11.91	1.11
S-GNF 7	93.57	4.79	1.65
S-GNF 8	93.99	4.63	1.38

A closer look is given to the high resolution peaks of carbon C1s and sulphur S2p. The sulphur peak S2p is a doublet, where S2p 1/2 is generally located 1.2 eV further than S2p 3/2. Also, the area of S2p 1/2 is equal to the half of the area of S2p 3/2. All of the analysed samples contain doublet peaks located at 164.0 and 165.2 eV, corresponding to the binding energy of thiophene groups, and orthorhombic sulphur. It is not possible to dissociate the binding energies of these two compounds by XPS due to the low electronegativity difference between the atoms of carbon and sulphur. Thiophene relates to a five atoms ring, where an atom of carbon is substituted by an atom of sulphur. Thiophene can be found in its polymeric form, the polythiophene, or implemented in the graphitic structure. Polythiophene can be plasma polymerized from thiophene monomers but this has never been achieved from carbon

disulphide precursor in plasma environment. The sample S-GNF7 is the only one containing traces of oxidized sulphur, located at 168 eV. It is recognized in the literature that the thiophene structure is preferential to promote the ORR [86].

The high resolution peak of carbon C1s is deconvoluted by using five peaks. The main peak for graphitic materials is located at ~284.5 eV and is related to the carbon in the sp2 conformation. An asymmetric pseudo-Voigt profile developed by Schmid *et al.* [152] and employed in this study provides a better fit of the sp2 contribution than usual symmetrical peaks. The parameters of the asymmetric pseudo-Voigt profile correspond to pure graphite. Symmetrical peaks are used for the sp3 contribution (~285.0 eV), the carbon linked to sulphur (~286.0 eV), the oxidized form of carbon (~287.9 eV) and the shoulder of the sp2 carbon (~283.5 eV). The relative amounts of carbon C sp2, C sp3, and linked to sulphur are listed in Table 5-3.

Table 5-3: Relative amounts of carbon sp2, sp3, and C-S in the S-GNFs.

Sample	% C sp2	% C sp3	% C-S
S-GNF 1	49.61	31.07	10.84
S-GNF 2	58.75	28.16	7.07
S-GNF 3	46.26	38.04	11.11
S-GNF 4	62.90	22.29	8.47
S-GNF 5	64.97	22.25	7.16
S-GNF 6	81.15	7.10	6.41
S-GNF 7	79.41	6.33	4.68
S-GNF 8	82.26	5.54	4.24

Similarly to what is observed for the sulphur level in the S-GNFs, the amount of carbon in sp3 conformation and the amount of carbon-sulphur bonds are linked to the experimental conditions. Decreasing the volume of injected carbon disulphide during the functionalization step leads to lower amounts of sp3 carbon and C-S bonds in the samples. Also, the 13.8 kPa/25 kW condition appear to bring less sp3 carbon and C-S bonds than the 55.3 kPa/20 kW condition when compared with the same liquid flow rate and exposure time.

The mass of S-GNFs was measured after collection of the different batches. A batch of non-functionalized GNFs results in a production weight of \sim 250 mg for a growing time of 12 min. The weight of collected S-GNFs is dependent on the injected volume of CS₂ during the functionalization step. An injected volume of 0.4 mL leads to a weight value similar to a

normal batch after collection, while 10 mL of injected CS₂ leads to weights of S-GNFs up to 600 mg. The additional mass found at the end of the functionalization as well as the analysis of the high resolution peaks of carbon and sulphur suggest that some carbonaceous material is also synthesized during the functionalization step, identified as polythiophene. The carbon sp3 can be related to the polythiophene plasma polymer, while the C-S content can be correlated to both polythiophene and sulphur functionalities implemented on the nanoparticles.

3.3. Structure of the S-GNFs

The eight samples of S-GNFs are analysed by Raman spectroscopy in order to study the graphitization of the carbon, and represented on Figure 5-4 for representative samples. The three main peaks in a Raman spectrum are studied for carbon-based materials: the D peak, at ~1350 cm⁻¹ relates to the amount of sp3 carbon and corresponds to defects in the graphitic structure, the G peak at ~1570 cm⁻¹ relates to the amount of graphitized carbon, and the G' peak at ~2700 cm⁻¹ shows increasing intensity and sharpness when the number of stacked graphene sheets decreases [153]. Additional relevant peaks in this study are found in the region of the D and G peaks [144]. The I peak, at ~1200 cm⁻¹, is a broad low frequency shoulder of the D peak that can be assigned to hydrocarbons connected to the graphitic structure. The D' peak, at ~1630 cm⁻¹, is a shoulder of the G peak. Finally, the D" peak, at ~1500 cm⁻¹ is a broad peak putting into evidence the presence of amorphous sp2 carbon. A weak signal is also observed at ~470 cm⁻¹ on the samples containing the highest amounts of sulphur (S-GNF1,2,3,4) and could correspond to traces of orthorhombic sulphur [154].

The region from 1000 to 1700 cm⁻¹ is deconvoluted following the five peaks I, D, D", G, and D' in order to separate the contribution of each peak. Lorentzian profiles are chosen to represent the D, G and D' peaks, while Gaussian profiles are used for the broad

peaks, I and D". It can be seen that the contribution of the I and D" peaks to the overall area are higher for the samples S-GNF1,2,3,4, which received the highest injected volume of CS₂ during the functionalization step. The non-negligible presence of I and D" peaks confirms the formation of carbon-based material containing amorphous sp2 carbon and bonded to the graphitic structure, confirming the presence of polythiophene. It has to be noted that the contribution of the D' peak is quasi-constant for all of the samples (~5%).

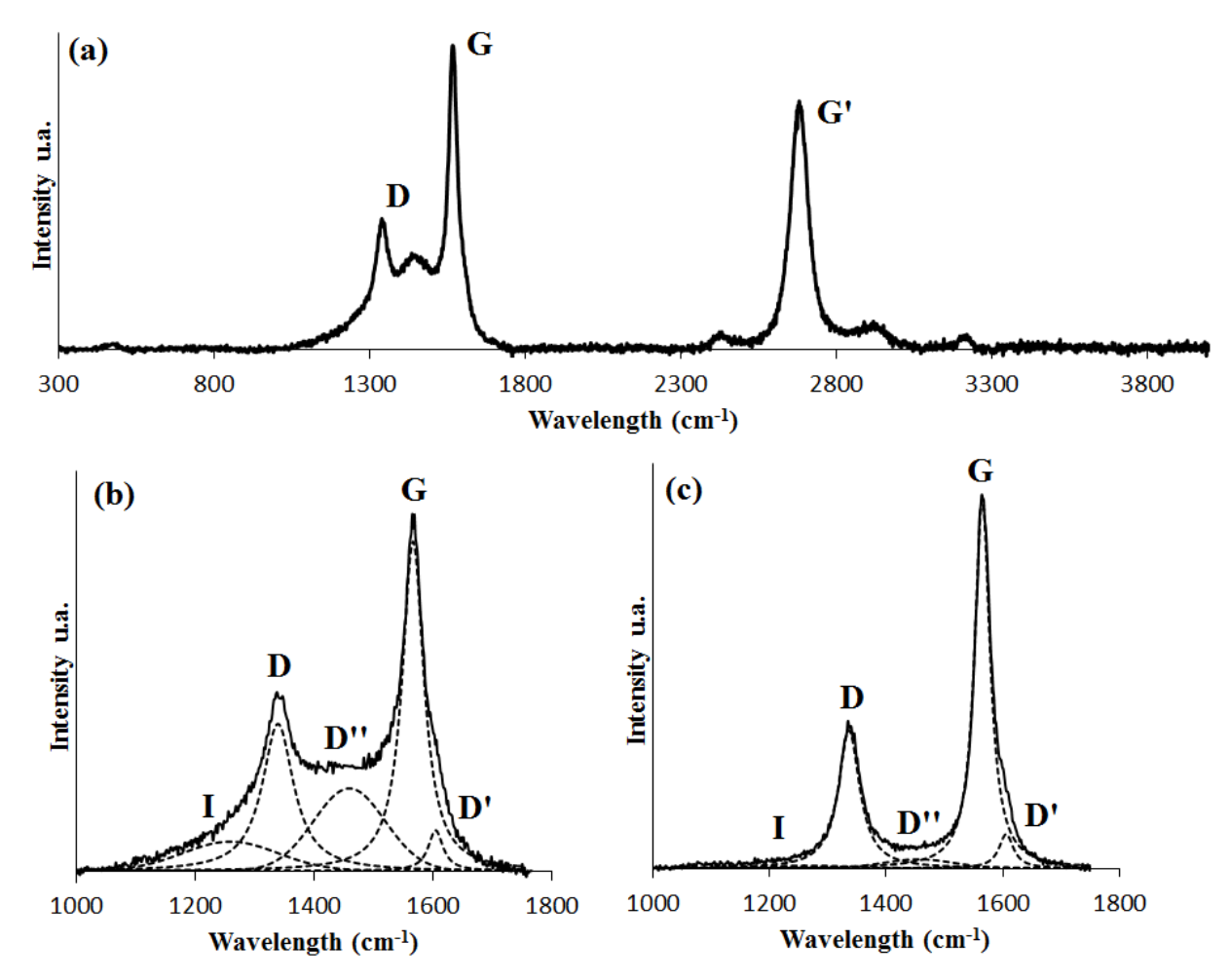


Figure 5-4: (a) Raman spectrum of S-GNF1. Deconvolution of the D-G peaks of (b) S-GNF1 and (c) S-GNF8.

The intensity and area under the curve of the D and G peaks can be extracted after deconvolution and used to determine several graphitic indices, giving an idea on the structural quality of the graphitic material. The intensity ratio of the G to D peak gives an

estimation of the purity of the sample. A ratio close or lower than 1 denotes poor quality materials, such as graphene oxide or reduced graphene oxide. The G to D ratio for the S-GNFs is comprised between 2.4 and 2.9, showing the high purity of the graphene nanoflakes even after functionalization. Two other graphitic indices can be deduced from the area under the D, G, and G' peaks. These indices, developed by Larouche *et al* [120], are L_a, the length of the smallest defect-free in-plane area, and L_{eq}, is the total length of crystallites linked by curvature. The formulas and values of the different graphitic indices are given in Table 5-4.

Table 5-4: Graphitic indices calculated from Raman spectra. The Formula values follow the study of Larouche *et al* [120].

	Purity	La (nm)	Leq (nm)
Formula	$I_{\mathrm{G}}/I_{\mathrm{D}}$	4.4·A _G /A _D	8.8·A _G :/A _D
S-GNF 1	2.47	6.67	17.64
S-GNF 2	2.39	7.63	19.74
S-GNF 3	2.52	6.89	19.27
S-GNF 4	2.65	7.20	22.13
S-GNF 5	2.52	8.15	23.77
S-GNF 6	2.78	8.64	27.49
S-GNF 7	2.74	8.08	24.39
S-GNF 8	2.91	8.50	26.10

The highest values for the different graphitic indices are found for the samples containing the lowest amounts of sulphur, confirming that functionalization efficiently occurs

on the GNFs and causes the purity and crystallinity of the samples to decrease with an increased volume of injected CS₂. Nevertheless, the values of the graphitic indices, even the lowest one, are still representative of high quality graphitic material.

Different samples of S-GNFs are analysed by XRD, and the samples S-GNF3 and 8, containing a high and a low amount of sulphur, respectively, are represented on Figure 5-5. Both samples contain the typical peaks of the graphene nanoflakes, a broad peak at 26.3°, with sharp peaks at 37.8°, 44.0°, 64.5°, and 78.1°. Samples containing a high amount of sulphur also show a large band centred between 20 and 24° corresponding to some amorphous material, and identified here as polythiophene. Several characteristic peaks of orthorhombic sulphur appear at 23.3°, 28.3°, 29.4° and 31.9°, the other peaks being too weak or contained in more intense peaks to appear on the diffractogram.

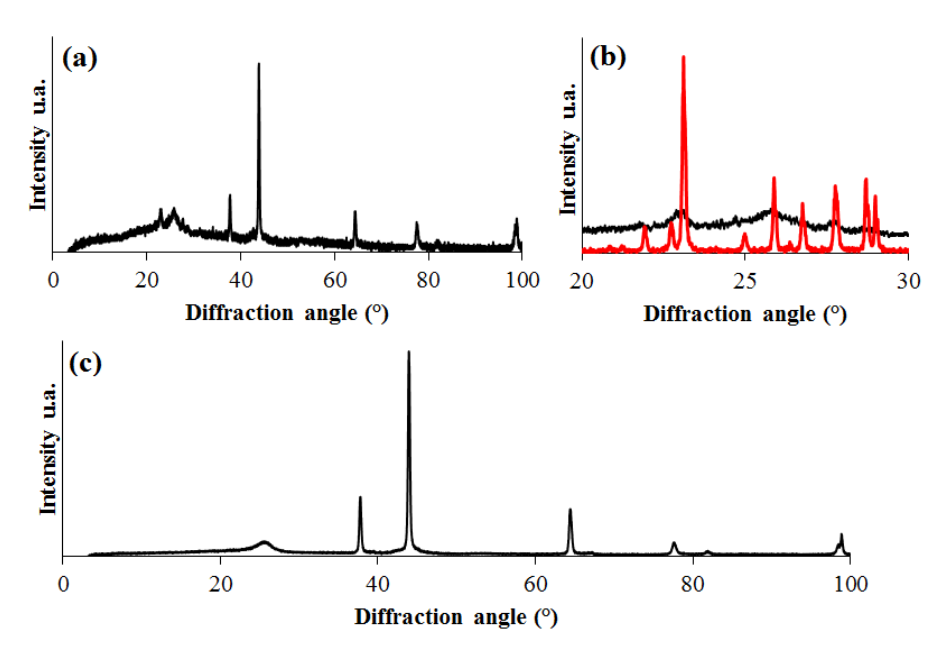


Figure 5-5: (a) X-ray diffractogram of S-GNF3, (b) Comparison between S-GNF3 (in black) and orthorhombic sulphur (in red) taken from RRUFF database [155], (c) X-ray diffractogram of S-GNF8.

The samples are also observed under SEM to study their overall appearance, as seen in Figure 5-6. The micrographs of the S-GNFs reveal that samples containing low amounts of

sulphur look like the non-functionalized GNFs. The S-GNFs containing a high amount of sulphur present a mixture of graphene nanoflakes and an amorphous material having a high porosity, considered as a plasma polymer having thiophene as repeating unit. No traces of solid sulphur detected by XRD have been observed with the SEM, suggesting a really low amount of orthorhombic sulphur in the samples.

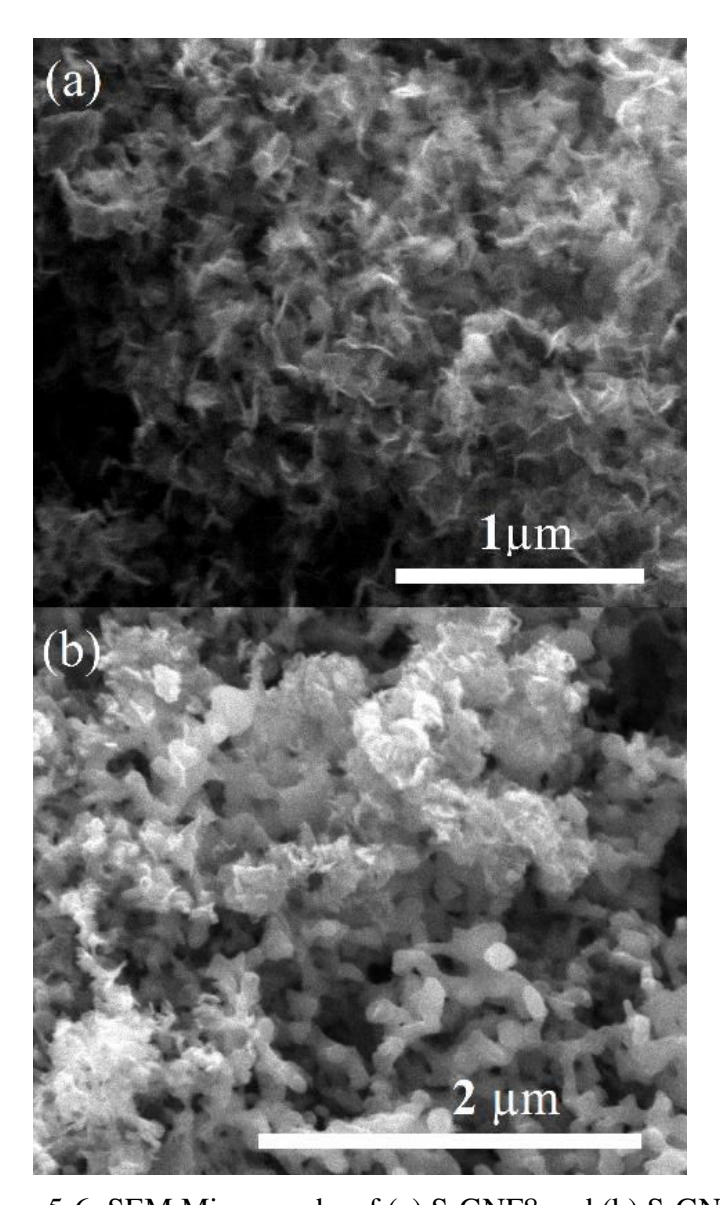


Figure 5-6: SEM Micrographs of (a) S-GNF8 and (b) S-GNF4.

3.4. Electrocatalytic activity of the S-GNFs

The ORR performance of the different S-GNFs samples is tested through RDE analysis and compared on the base of the onset potential, the limiting current density, the half wave potential, and the number of electrons transferred during the electrochemical reaction. The onset potential is defined when the current density is no longer equal to zero. Platinum based catalysts generally have an onset potential between 0.8 and 0.9 V, depending on the catalyst preparation method [75]. The half-wave potential is the reported potential where the intensity of the current density reaches half of the value of the limiting current density. Close values of onset potential and half-wave potential result in a sharp curve which is directly related to the kinetics of the reaction. The LSVs of the S-GNFs exhibit features which can be correlated to their composition. Indeed, the onset potential of S-GNFs is the same for all of the samples, and equal to 0.7 V, which is only 0.1 V lower than the platinum based catalysts. The half-wave potential for the samples is also similar, and at around 0.56 V, indicating a relatively sharp decrease of the current density for the S-GNFs. The main difference between the samples comes from the amplitude of the limiting current density, related to the rate of the ORR. The S-GNFs containing the highest amount of sulphur see the amplitude of their limiting current density higher than the ones containing lower sulphur amounts. The ORR performance of the S-GNFs suggest the addition of sulphur to the GNFs promotes the ORR with a greater improvement with a higher sulphur content. The typical data obtained for the S-GNFs are on Figure 5-7, while the overall performances for all of the samples are summarized in the Table 5-5. The number of electrons transferred to the ORR is calculated by the Koutecky-Levich formula, described in Equation 2 and 3.

$$\frac{1}{j} = \frac{1}{B\omega^{1/2}} + \frac{1}{j_K}$$
 Equation 2

$$B = 0.62 \text{nFC}_0 D_0^{2/3} v^{-1/6}$$
 Equation 3

where j_k is the kinetic current, n is the number of electrons transferred to the ORR, F is the Faraday constant (96485 C.mol⁻¹), C_0 is the bulk concentration of oxygen in the alkaline medium (1.2·10⁻⁶ mol.L⁻¹), D_0 is the diffusion coefficient of oxygen (1.9·10⁻⁵ cm².s⁻¹)

and ν is the kinematic viscosity of the 0.1M KOH solution (1.0·10⁻² cm²·s⁻¹) [145]. LSVs are recorded when the working electrode is at different rotational speed ω , from 100 to 2500 rpm, and the number of electrons transferred to the ORR is found using the slope of the j⁻¹ vs ω ^{-1/2} plotted for different potentials.

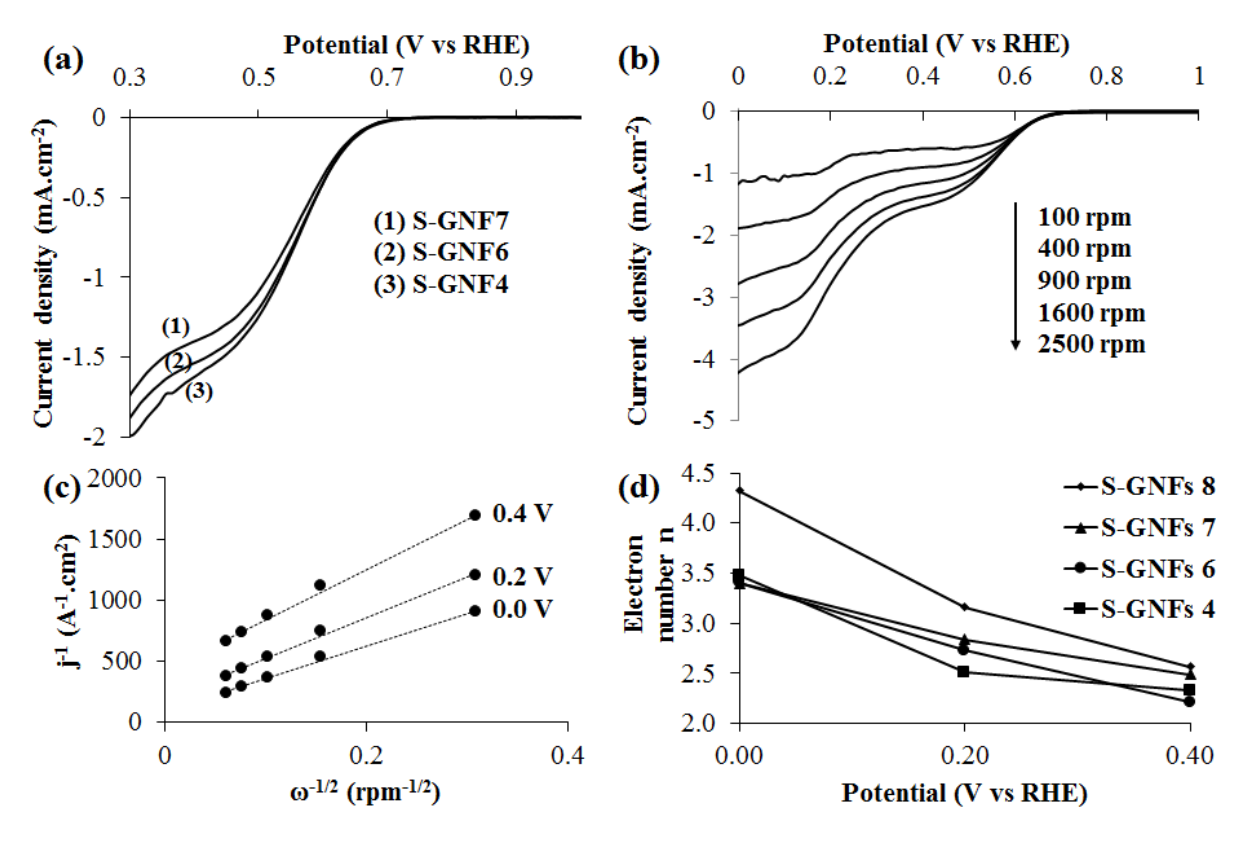


Figure 5-7: (a) LSV of some representative S-GNFs samples, (b) LSV for S-GNF6 for rotation rate from 100 to 2500 rpm, (c) Koutecky-Levich Plot for S-GNF6 at 0.0, 0.2 and 0.4 V, (d) Number of electrons transferred to the ORR for some representative S-GNFs samples at different potentials.

The number of electrons transferred to the ORR is higher for the samples with lower amounts of sulphur. For the S-GNF7 and 8 samples, the ORR is performed close to a four-

electron path at a potential of 0.0V while the number of electrons transferred to the ORR is closer to two at higher potentials. It indicates that the samples containing low amounts of sulphur perform the ORR with less efficiency in terms of current density, but with a higher number of electron transferred.

Table 5-5: Values for the ORR performance of the S-GNFs.

	Onset Potential	Half-wave Potential	Current density @
	(V vs RHE)	(V vs RHE)	0.4V (mA.cm ⁻²)
S-GNF 1	0.70	0.56	1.31
S-GNF 2	0.70	0.55	1.57
S-GNF 3	0.71	0.56	1.56
S-GNF 4	0.71	0.56	1.63
S-GNF 5	0.71	0.56	1.57
S-GNF 6	0.72	0.56	1.54
S-GNF 7	0.71	0.56	1.40
S-GNF 8	0.71	0.56	1.51

3.5. Discussion

The thermal plasma route employed in this study for the addition of sulphur to the graphene nanoflakes lead to GNFs with the implementation of sulphur functionalities on the nanoparticles surface. Also, the S-GNFs are covered by polythiophene plasma polymer and contain traces of orthorhombic sulphur. The formation of orthorhombic sulphur was predicted

by the thermodynamic modelling of the plasma system contrary to the formation of polythiophene. This study is to our knowledge the first describing the formation of polythiophene by carbon disulphide plasma decomposition, and its deposition on a graphene material. Other studies already mentioned the polymerization of thiophene monomers by the plasma route, with glow-discharge apparatuses [156].

The plasma conditions during the functionalization step are influencing the resulting composition, and generating differences in the catalyst performance. The 13.8 kPa/ 25 kW conditions used for the functionalization step are generally correlated to purest samples containing less sulphur than the 55.3 kPa/ 20 kW conditions. This result mainly comes from the residence time differences these conditions generate in the recombination zone between the thermal plasma environment and the powders. The gas velocities at 13.8 kPa/ 25 kW are four times higher than those at 55.3 kPa/ 20 kW, this lower residence time allowing less time for additional material such as the polythiophene plasma polymer or orthorhombic sulphur to be produced.

The parameter generating the larger changes in the composition of the S-GNFs is the total volume of carbon disulphide injected during the functionalization step. This parameter can be chosen to tune the total amount of sulphur at the end of the synthesis process. For an identical volume of injected CS₂, lower flow rates globally lead to higher amounts of sulphur, and so lower purity and crystallinity of the samples. The sulphur content is related here to the ORR performance of the samples, where higher amounts of sulphur globally promote the ORR.

4. Conclusion

This study showed that sulphur-rich graphene nanoflakes can be grown and functionalized through a single batch thermal plasma process by changing the feeding

conditions. The resulting material contains graphene nanoflakes with both polythiophene plasma polymer covering the S-GNFs and sulphur implemented in the graphitic structure, and exhibiting electrocatalytic activity toward the ORR. The samples produced have tuneable amounts of sulphur between roughly 4 and 28 at%S. This sulphur content can easily be controlled by changing the injected volume of carbon disulphide during the functionalization step. Traces of orthorhombic sulphur have been found, but are known to not participate to the ORR. The S-GNFs have a potential to be used in various applications, such as Li-ion batteries and supercapacitors [157], or sensors based on the variable content of sulphur [158].

Part II Additional information on the sulphur functionalization (non-published): TEM analysis

Some samples of S-GNFs have been analysed through TEM on a FEI Tecnai G2 F20 200 kV Cryo-STEM in complement of the study presented in the last part. Results for the sample S-GNF4 are presented in this section, and tend to confirm the observations made previously.

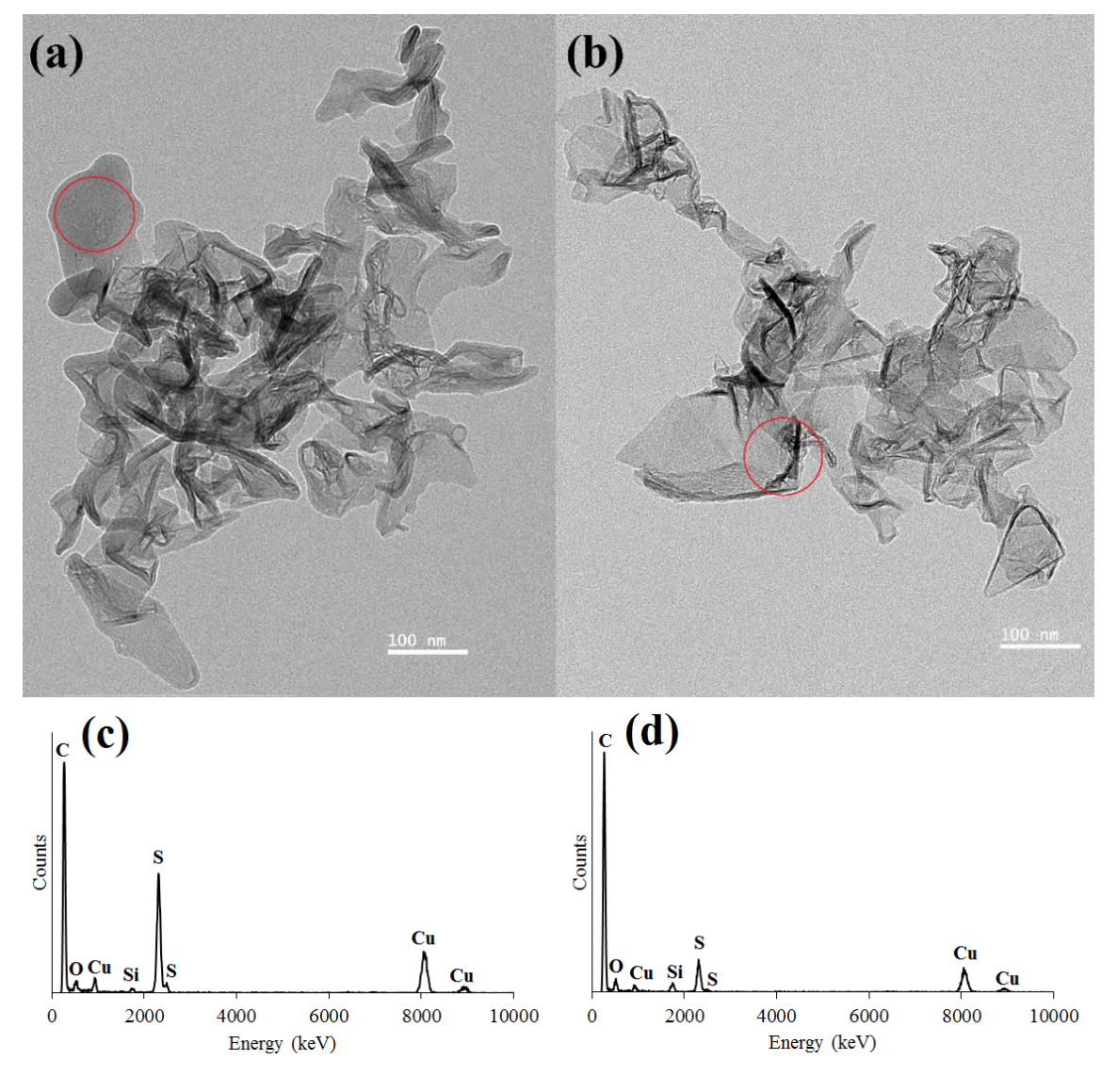


Figure 5-8: TEM micrographs of the sample S-GNFs showing areas with (a) presence of polymer (b) absence of polymer. The red circle represents the area where the respective EDX spectra have been recorded in (c) and (d).

As seen in Figure 5-8, the S-GNFs present areas with a large amount of plasma polymer and other areas devoid of polymer. The plasma polymer can be recognized by its amorphous structure while the GNFs exhibit the typical graphitic structure, with graphene sheets discernible from each other. In the areas containing the sulphur polymer, it appears that the polymer partially covers the GNFs (Figure 5-9). An area containing mostly plasma polymer has been analysed with EDX and shows the presence of carbon, sulphur and traces of oxygen. The presence of copper and silicon is due to the grid supporting the sample to be analysed. EDX spectrum is also taken in an area with no polymer. The EDX also gives a composition of carbon, oxygen and sulphur, but with a smaller amount of sulphur compared to the area with polymer. EDX cannot provide a precise elemental composition for reasons advanced in the Chapter 4. However, it can be deduced from the analysis of the spectra that sulphur in the S-GNFs is mostly found in the form of plasma polymer, but are also incorporated in the graphitic structure of the GNFs in lower quantities. The results done by TEM and EDX confirm the observation made in the previous part, even if no traces of solid sulphur have been found by TEM.

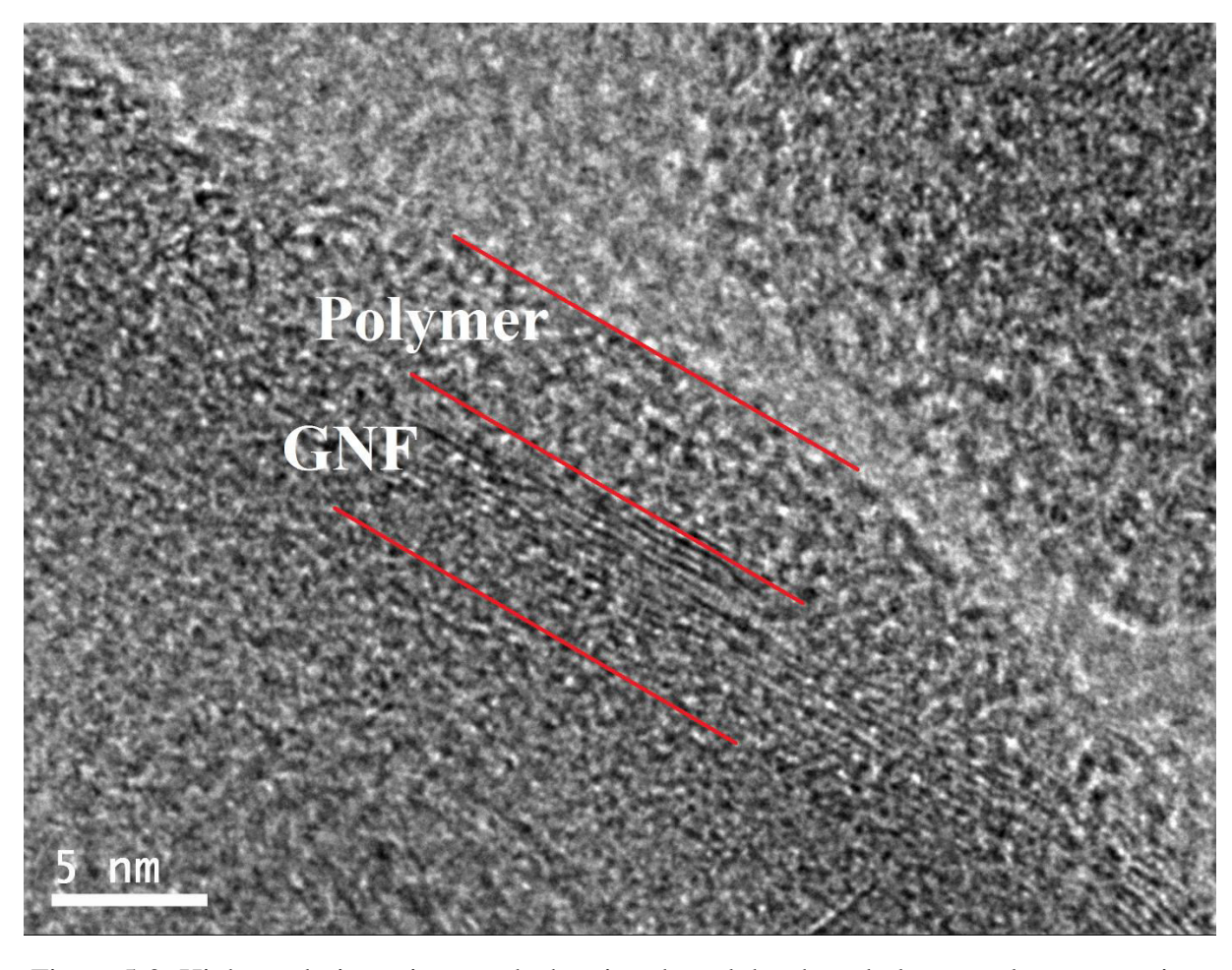


Figure 5-9: High resolution micrograph showing the sulphur based plasma polymer covering GNFs.

Chapter 6 OXYGEN FUNCTIONALIZATION OF THE GRAPHENE

NANOFLAKES FOR NANOFLUID APPLICATIONS

Part I Synthesis and in-situ oxygen functionalization of deposited graphene nanoflakes for nanofluid generation

This section presents an article that has been published in the journal *Carbon*, having for reference:

U. Legrand, N.-Y. Mendoza Gonzalez, P. Pascone, J.-L. Meunier, D. Berk, Synthesis and insitu oxygen functionalization of deposited graphene nanoflakes for nanofluid generation, Carbon, 102, 216-223, 2016.

The work has been conducted, analyzed and written by U. Legrand (Ph.D. candidate). N.Y. Mendoza Gonzalez provided the modelling of the reactor and its analysis. P. Pascone realized the Raman measurements on the different samples and their analysis. Dr. J.-L. Meunier and Dr. D. Berk provided supervision and reviewing of the manuscript.

This project started from the observation that the GNFs are naturally hydrophobic, making more difficult the preparation of catalyst inks for a fuel cell membrane. The generation of reactive species in the thermal plasma and then the addition of oxygen functionalities on the surface of the GNFs is expected to make them hydrophilic. Thus, the dispersion of the GNFs can be facilitated, without the use of any surfactant around these nanoparticles. The resulting samples exhibit outstanding properties in terms of dispersion in fluids such as water and ethanol for over 6 weeks.

This work also led to the filing of a patent:

J.-L. Meunier, D. Berk, U. Legrand, N.-Y. Mendoza Gonzalez, P. Pascone, Oxygen functionalized graphene nanoflakes, a stable and surfactant-free graphene nanofluid and method from making same, United States Patent Application 20160376153.

Synthesis and in-situ oxygen functionalization of deposited graphene nanoflakes for nanofluid generation

Ulrich Legrand, Norma Mendoza Gonzalez, Pierre Pascone, Jean-Luc Meunier, Dimitrios Berk

Plasma Processing Laboratory, Department of Chemical Engineering, McGill University

Abstract: Graphene nanoflakes (GNFs) are a stack of 5 to 20 layers of highly crystalline graphene sheets having a planar size of approximatively 100 by 100 nm and low defect concentration. They are produced here through homogeneous nucleation following the plasma decomposition of a carbon source in an inductively coupled thermal plasma reactor. Following synthesis within the plasma reactor, the GNFs are functionalized downstream in the plasma recombination zone with the addition of oxygen to the main plasma stream. Tunable oxygen functionalization is obtained and values up to 14.2 atomic percent are reached on the surface of the particles. While the non-functionalized GNFs are hydrophobic, the oxygen-functionalized GNFs (O-GNFs) show full stability of all the produced powders when directly dispersed in water or ethanol without any surfactant. The O-GNFs keep their structural integrity even after the implementation of the hydrophilic groups on the surface of the nanoparticles, and maintain their dispersion stability in water and ethanol over a long period of time.

1. Introduction

Presently graphene is one of the most promising materials. Because of the high electrical and thermal conductivity characteristics, graphene has potential applications in a wide variety of fields such as the energy, electronics, biomedical, sensors, and materials sectors [2][159]. Some of the main factors limiting the implementation of technologies based on graphene are the current limitations in the production methods for generating this material, and very often the relatively poor quality of the graphene structures being generated in some

of the widely used methods. Many applications also require the graphene to be hydrophilic in order to be dispersed in a solvent or a matrix. The production techniques of hydrophilic graphene sheets found in the literature follow a 2-step process: first the generation of graphene followed by a functionalization step. The graphene generation can be separated in bottom-up and top-down methods. One important bottom-up method for producing graphene is the Chemical Vapour Deposition (CVD) of decomposed carbon species on a metallic surface such as copper or nickel [63]. The CVD method produces high purity graphene on large surface areas of the substrate, and from monolayers to a few graphene layers in thickness [160]. The CVD method produces low quantities of graphene sheets, limiting the range of applications. The top-down approaches are based on the separation of graphene sheets from graphitic structures, these methods typically yielding much larger quantities of graphene powders [161]. The graphite can be directly exfoliated by sonication [162], or be first oxidized into graphite oxide, facilitating the separation of the graphene sheets by sonication [163]. The graphene oxide (GO) can be used as is in some applications [164], or reduced to form reduced graphene oxide (RGO) powders.

Different methods exist in order to functionalize graphene with oxygen. A common method is to generate active oxygen species by injecting oxygen gas in an argon plasma, these active species later reacting with graphene to produce the hydrophilic material [165]. Several types of low power plasma systems have been used such as microwave plasmas [166], electron-beam generated plasmas [167] operating at low pressure or even in ultra-high vacuum, for an exposure time during a couple of seconds [168] to several hours [169]. The resulting materials are exhibiting hydrophilic properties, but present a high number of defects in their crystalline structure. In fact, the disorder level in many of these structures is so high that the graphene label itself can be questioned. Associated to the disorder of these structures is the lower purity of the RGO structures [111]. The strong disorder or low crystallinity, and

the lower purity of RGO are responsible for a large fraction of performance limitations of these materials when compared to what could be expected from crystalline graphene structures [170].

In response of these constraints, a bottom-up method to produce highly crystalline carbon powders in the shape of graphene flakes was developed by Pristavita using homogeneous nucleation following the thermal plasma decomposition of methane [114]. Modelling and experimental optimization enabled the production of pure, homogeneous, and well crystalized powders having between 5-20 graphene layers and in-plane dimensions of roughly 100 by 100 nm. The graphene nanoflake (GNF) structure optimizes the crystallinity and minimizes the impurity content when compared to RGO.

In the present work, fully hydrophilic GNFs are produced by adding and tuning the level of oxygen functionalities on the nanomaterial through a change of the gas feed directly within the plasma reactor, rendering the produced powder hydrophilic with a high stability. The advantage of this method is that it uses a single processing step for the growth and functionalization of the graphene powders in one reactor, reducing time and manipulation while generating a fully dispersed and stable graphene nanofluids. The new material is characterized and compared to hydrophobic GNFs to determine differences in the chemical structure.

2. Methods

The method presented here describes a two-stage process where the GNFs are grown and deposited as a first stage, and functionalized with oxygen as a second stage by changing the feeding gas conditions without opening the reactor. GNFs are grown following the procedure of Pristavita *et al.* in which a carbon source, typically methane, is decomposed using an argon thermal plasma having very well controlled fluid dynamics [114]. In this so

called first stage of the process, GNFs are generated through homogeneous nucleation with growth taking place in a very diluted system. The nucleation and growth occur within a temperature window of roughly 3700-4900K arising from controlled flow lines of the plasma downstream of the ICP plasma torch [28]. A fraction of the nanoparticles is deposited by thermophoresis on the side walls of the reactor. The bulk of the powder is deposited on the downstream collecting plate of the reactor set in an axisymmetric stagnation point flow geometry pattern. Immediately after this nucleation step, a second step of the process is set by changing the nucleation gas feed (methane/nitrogen) to a chemical functionalization feed made of 1 slpm of air (79% nitrogen and 21% oxygen), argon being maintained as the main plasma gas. The oxygen from the air forms active species which interact with the surface of the nanoparticles to produce hydrophilic groups. The thickness of the GNF deposit during 10 minutes of operation varies from 1 to 5 µm and forms a highly porous layer. The expanding flow geometry in this zone of thermal plasma recombination is expected to maintain some active oxygen species able to diffuse through the porous layer and functionalize the nanoparticles [99]. This two-stage process is favoured over a one-stage process with air injected simultaneously with the carbon source; experimental observations and equilibrium thermodynamic calculations showed that the oxygen from the air consumes the carbon and produces carbon monoxide and carbon dioxide instead of GNFs.

The power delivered to the ICP torch, the pressure in the reactor and the duration of the functionalization step are the tested conditions to see the influence on the level of functionalities added to the GNF structures and on the dispersion quality. The power and pressure conditions control the plasma composition and flow fields in the recombination zone, and hence affect the production and transport of active oxygen species that could be involved in the functionalization process. The duration of the functionalization step is expected to affect the amount of implemented oxygen species onto the GNFs. The effect of

the pressure and plasma torch power on the flow field formed in the argon-air thermal plasma was initially analyzed through Computational Fluid Dynamics (CFD). The modelling study focused on two power/pressure couples: 20 kW/55.2 kPa (8 psia), which correspond to the conditions of GNF growth, and 25 kW/13.8 kPa (2 psia). Previous studies showed that lower pressures coupled with higher plasma power leads to greater nitrogen functionalities added on the GNFs in the same configuration [8].

The modeling conditions are similar to previous modeling work reported on this reactor [114]. These include a two-dimensional axisymmetric, steady state and standard kepsilon RNG model. This model considers an argon-air mixture, with the assumption of a non-reacting system since the objective at this stage is mainly to tune the flow and temperature fields and not the reacting and excited species. The transport and thermodynamic properties of the argon and air plasma were taken from Boulos [97] and the mixture properties were mass weighted based on the mass fraction with constant species diffusion. The boundary conditions for the flow streams are Q_1 = 4.5 slpm (Ar) + 1 slpm (air), Q_2 =13 slpm and Q_3 =45 slpm which are respectively for the precursor, plasma and sheath gas injection. The temperature distributions in the reactor, as well as the velocity profiles are represented in Figure 6-1.

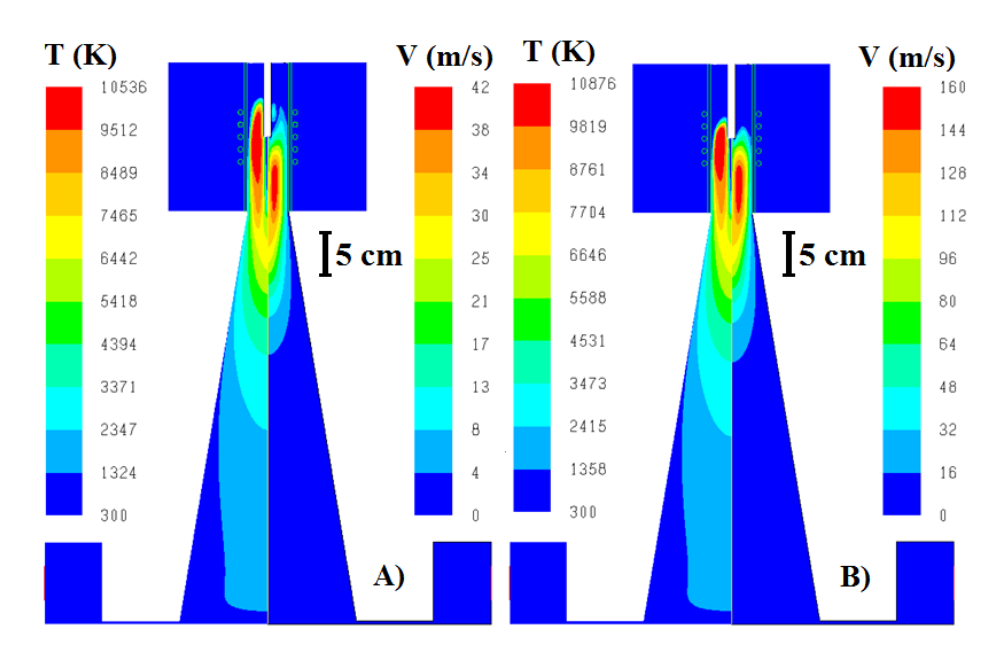


Figure 6-1: Temperature and velocity profiles for tested conditions: A) 55.2 kPa / 20 kW and B) 13.8 kPa / 25 kW for a length scale bar of 5cm. Note the velocity fields are higher by a factor 4 in the (B) case.

The temperature profiles are similar for both pressure and power conditions, with the temperatures obtained for the 13.8 kPa / 25 kW case only slightly higher in the highest temperature zone within and at the outlet of the ICP torch. The main difference is observed for the gas velocities. The lower pressure of 13.8 kPa in the reactor induces plasma and gas velocities that are four times higher at the bottom of the reactor compared to 55.8 kPa pressure. For example, on-axis velocities at a distance of 32 cm from the bottom plate are 4 m/s at 55.8 kPa, while they reach 16 m/s at 13.8 kPa. The difference in velocities between the two cases can lead to different oxygen functionalization rates depending on the lifetime and residence time of the excited oxygen species. After being decomposed at high temperature, atomic oxygen is recombined downstream upon jet cooling. Equilibrium thermodynamic calculations indicate however that atomic oxygen still represents 1% of the overall oxygen species at a temperature of 2500K [97]. From this 2500K isotherm in our reactor, flow dynamics calculations indicate the oxygen species have a relatively short traveling time of 0.07 s before reaching the bottom plate in the 13.8 kPa / 25 kW case. This time scale can

potentially maintain some atomic oxygen concentration for providing functionalities to the GNFs. In comparison, this transport time is much longer at 0.29 s in the 55.8 kPa / 20 kW case.

The total duration of the oxygen functionalization step needs to be optimized since short functionalization times produce low oxygen content on the nanoparticles, while longer times allow oxygen to consume a fraction of the deposited GNFs. The results of the equilibrium CFD model, the residence time evaluations and considerations on the functionalization step duration provided the guidelines for the choice of experimental conditions. The conditions used throughout the functionalization step are listed in Table 6-1, knowing that the growth step is performed at 55.2 kPa / 20 kW for 10 min.

Table 6-1: Conditions for the samples preparation.

Samples	Pressure/Power conditions	Duration of the functionalization	
A	55.2 kPa / 20 kW	10 min	
В	55.2 kPa / 20 kW	20 min	
С	13.8 kPa / 25 kW	10 min	
D	13.8 kPa / 25 kW	5 min	

The powders deposited on the collecting plate are weighed to obtain the yield of both non-functionalized GNFs and oxygen functionalized GNFs (O-GNFs), a batch of pure GNFs from the initial nucleation step in the present experiments yielding approximatively 200 mg GNFs.

Dispersion tests are realized in water and ethanol. The tests are conducted using 5 mg of powder from the different tested conditions and 8 mL of solvent. The stability of the dispersion in water was evaluated from the zeta potential using a Zetasizer Nano ZS from Malvern, while the stability in ethanol was observed visually.

The chemical structure characterization by X-ray photoelectron spectroscopy (XPS) was made using a VG Scientific ESCALAB MK II operating at a pressure of 1.3x10⁻¹⁰ kPa (10⁻⁹ torr) and using an aluminium X-ray source. Scanning Electron Microscopy (SEM) was performed on a FEI Inspect F-50 FE-SEM and Transmission Electron Microscopy (TEM) on a FEI Tecnai G2 F20 200 kV Cryo-STEM. The Raman instrument used was an inVia Reflex confocal micro-Raman (Renishaw) with a laser emitting at a wavelength of 514.5 nm. The mass and purity of the GNFs was examined by Thermal Gravimetric Analysis (TGA) on a TA Q500, with a constant heating rate of 20 °C/min applied from ambient temperature to 900 °C in air.

3. Results and discussion

3.1. Oxygen content

The atomic composition of the O-GNFs surface is determined using XPS. This non-destructive technique gives information on the elemental composition of the first few nanometres of the sample. As the GNFs are oriented in all directions and form a relatively porous layer, XPS is expected to yield a relatively good estimation of the atomic composition over their surface and edges. However no discrimination is possible using XPS for an evaluation of the spatial distribution of the oxygen over the GNFs surfaces and/or edges. The XPS survey scan of the functionalized GNFs in a 13.8 kPa/25 kW argon plasma during 10 min shows the carbon and oxygen peaks with some traces of nitrogen (Figure 6-2).

Under the experimental conditions shown in Table 6-1, the oxygen content is found to go as high as 14.2 at.%O. This is well above the typical oxygen content on GNFs of approximately 1 to 2 at.%O which originates from contamination in air. The oxygen contents and the yields for the four conditions of Table 6-1 are summarized in Table 6-2. The yield values are representative of the loss of GNFs during functionalization. The samples having the highest oxygen contents, 13.9 and 14.2 at%O respectively, showed important losses in GNF mass at the end of the oxygen functionalization step by amounts of 74 and 44% losses based on a typical batch of approximately 200 ± 10 mg of GNFs produced in the initial nucleation phase of the process. This mass loss can be attributed to a combustion process of the GNFs by oxygen. The A and D samples having the lowest oxygen content of 1.3 and 6.4 at%O respectively, did not reveal any significant weight loss during the functionalization step. The weight loss is directly linked to the oxidation of GNFs after either a long time exposure to the air plasma, or exposure to the reactive species particularly at the lower pressure of 13.8 kPa. This highlights the importance of the total transport of reactive oxygen species to the GNF layer.

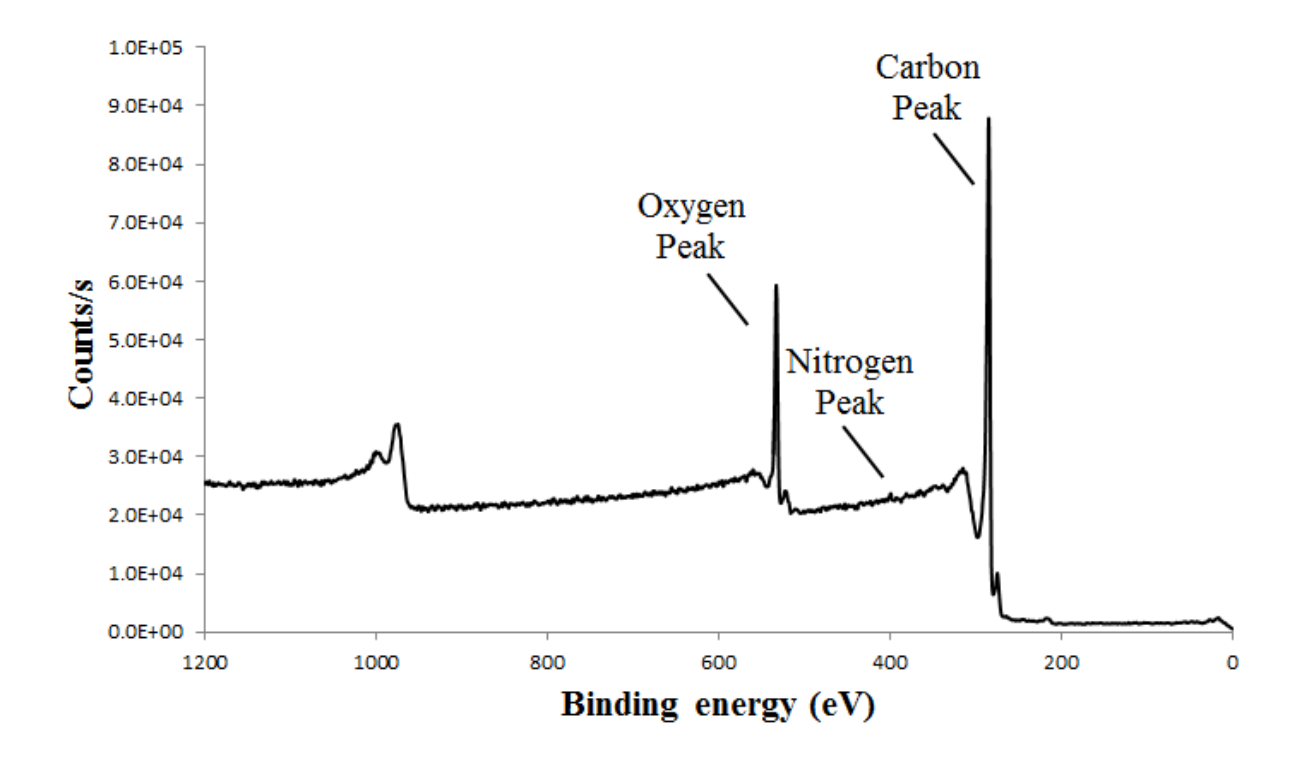


Figure 6-2: XPS survey scan of O-GNFs (sample C).

Table 6-2: Yields and atomic composition after oxygen functionalization.

Sample	A	В	C	D
Yield (mg)	196.6	52.5	111.7	205
C at%	98.1	85.3	84.9	92.8
N at%	0.6	0.8	0.9	0.8
O at%	1.3	13.9	14.2	6.4

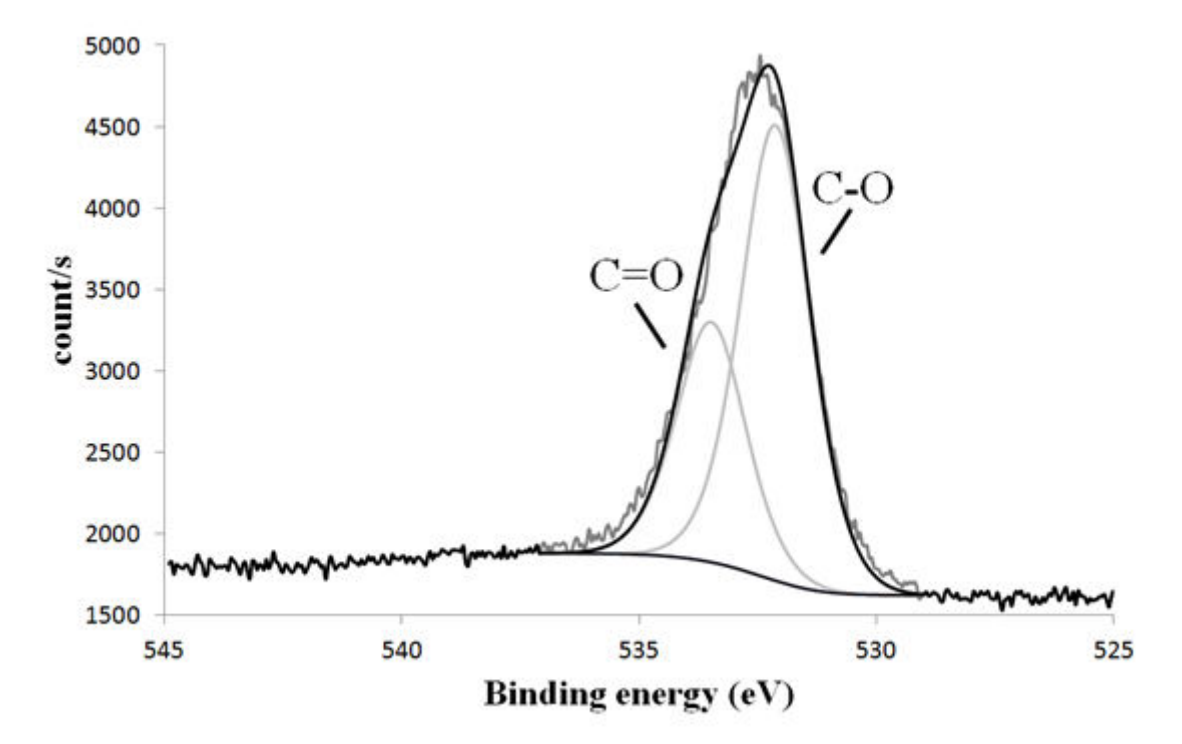


Figure 6-3: High resolution and deconvolution of oxygen peak and deconvolution for O-GNFs (sample C).

The oxygen and carbon peaks were studied in more detail through a deconvolution based on Gaussian-Lorentzian fitting. This analysis extracts the state(s) of the element, and

the functional groups formed with that element can be retrieved. The deconvolution of oxygen and carbon peaks is presented here for sample C giving the best combined result in terms of oxygen content and yield. In Figure 6-3, showing the deconvolution of the oxygen peak, the main binding energies involved are 532.1 and 533.3 eV. The highest binding energies are mainly associated with oxygen double-bonded to carbon, while the lowest binding energies correspond to single-bonded oxygen with carbon. Different hydrophilic groups are involving C-O and C=O bonds, such as esters, carboxylic groups, anhydrides, hydroxyls and ether oxide [171]. XPS analysis gives only the nature of the elements and the type of bonds involved; the nature of the hydrophilic groups cannot be inferred from these. The deconvolution of the carbon peak (Figure 6-4) confirms the presence of the hydrophilic groups with peaks at 285.5, 287.7, and 286.7 eV corresponding respectively with C-O, C=O, and O=C-O bonds. The deconvolution of the carbon peak also gives the C-C bond close to 284.5 eV, related to graphitic carbon.

One should recall here that the location of the GNFs within the reactor on the water-cooled bottom plate corresponds to a low temperature region for which equilibrium thermodynamic would indicate no presence of strongly reactive oxygen species. Our ability to functionalize with oxygen following Figures 6-3 and 6-4 indicate that the downstream recombination zone of a thermal plasma can provide, under proper pressure and mass transport conditions, the active oxygen species for functionalization.

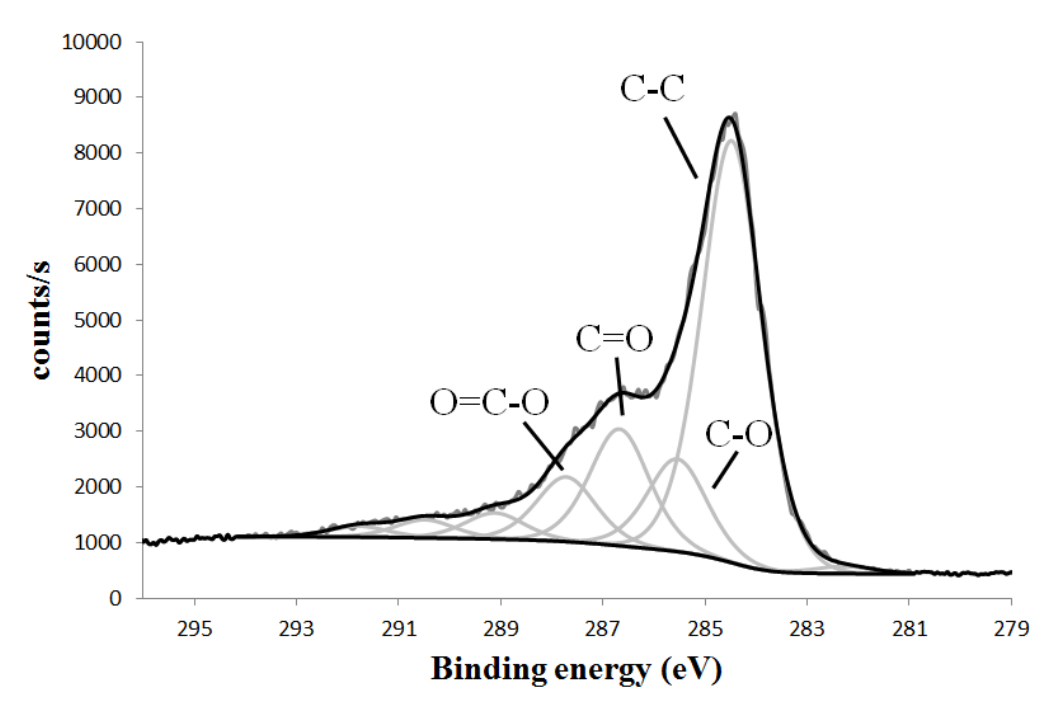


Figure 6-4: High resolution and deconvolution of carbon peak for O-GNFs from sample C.

3.2. Homogeneity and crystallinity

The samples functionalized at the different conditions were analysed by SEM and compared to non-functionalized GNFs (Figure 6-5). The O-GNF samples showed the same appearance as the non-treated GNFs. The only observed difference between the samples is slightly more charging effect being observed on the O-GNF in the SEM. It is important to note the absence of any noticeable amorphous carbon or polymer in the samples; this again highlights the purity of the O-GNFs.

A closer view is obtained using TEM showing isolated oxygen-functionalized nanoflake edges from Sample C having 14.2 at%O compared to the non-functionalized GNFs (Figure 6-6). Once again, GNFs and O-GNFs look very similar with 5 to 20 graphene sheets counted through the different pictures. The electron diffraction pattern for both materials clearly show the very high crystallinity of the GNF structures with set of parallel lattice planes scattering electrons into the distinctive rings, while the crystallites are orientated in all

directions. The diffraction pattern is associated, as expected, with graphitic structure for both GNFs and O-GNFs with the crystallographic planes associated with the rings in Figure 6-7 coming from the theoretical diffraction pattern of graphitic materials [172]. One can note also that the oxygen functionalized graphene material observed under TEM and SEM does not reveal the appearance of new defects associated with the functionalization process.

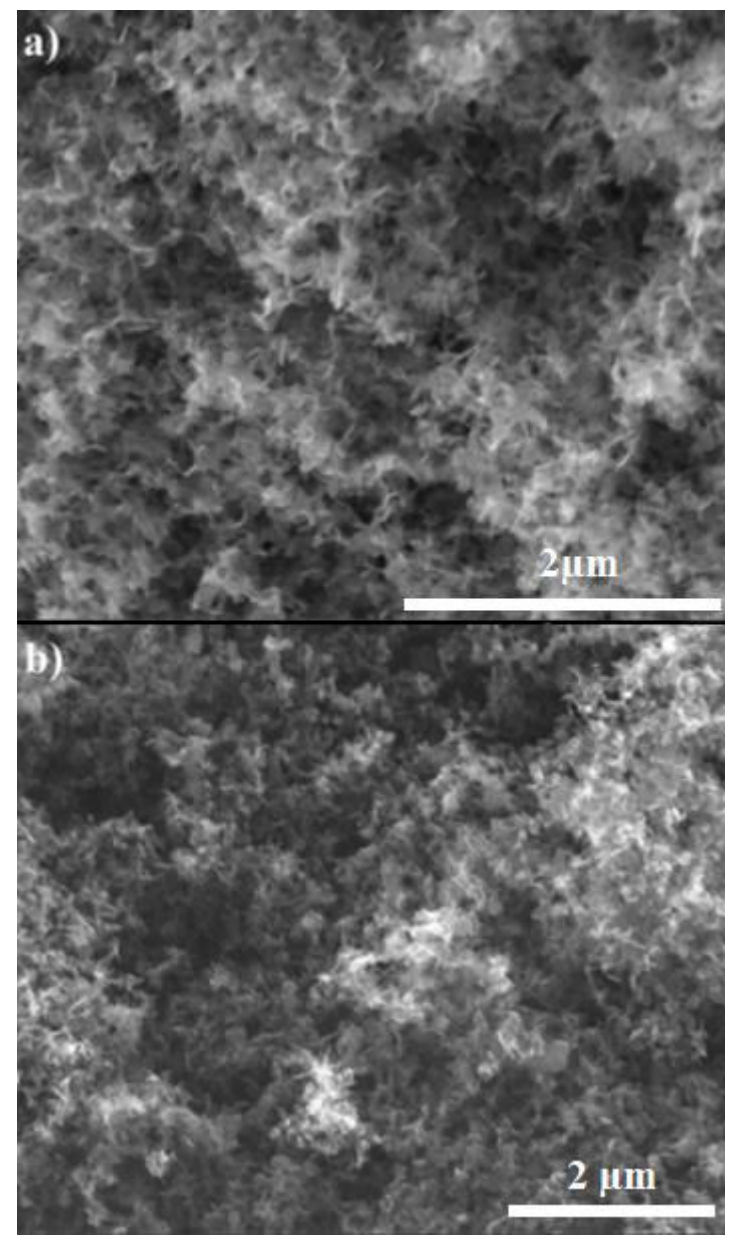


Figure 6-5: SEM picture of a) non-functionalized GNFs and b) O-GNFs from sample C, for a length scale bar of 2 $\mu m.$

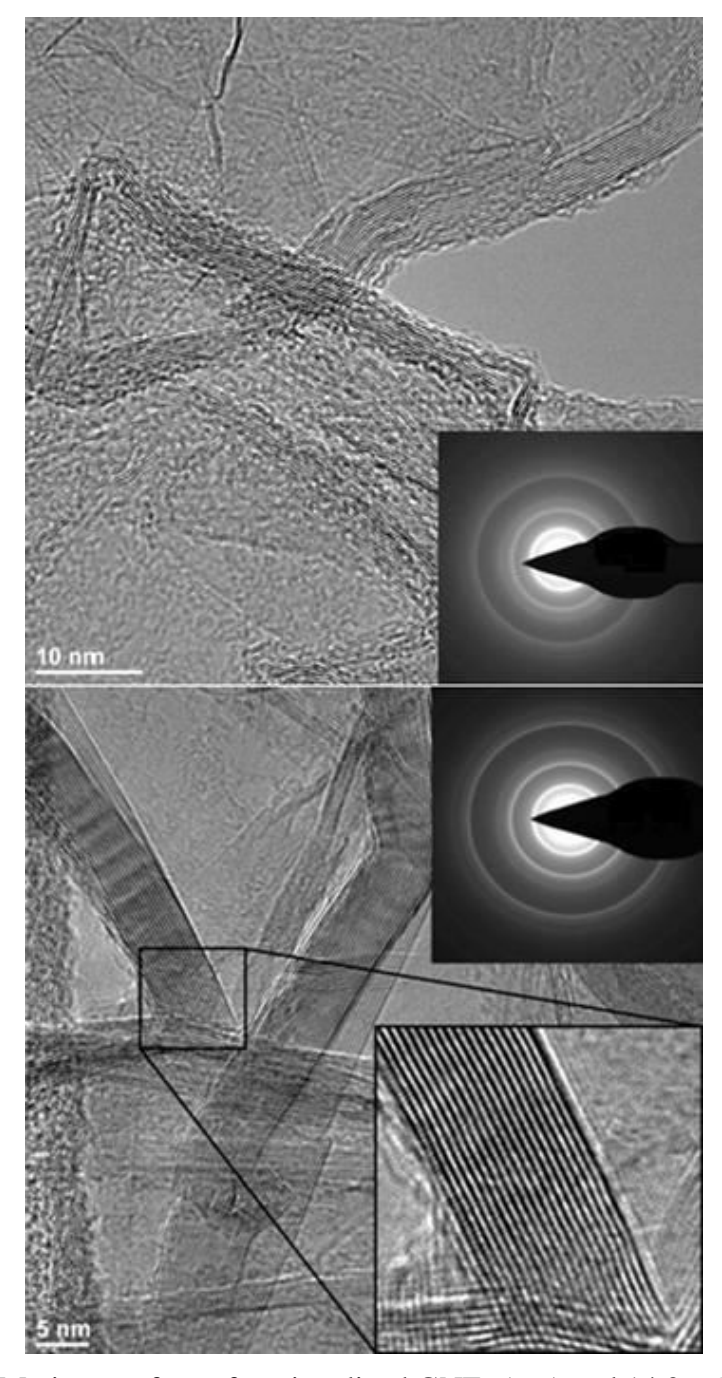


Figure 6-6: TEM picture of non-functionalized GNFs (top) and 14.2 at%O-GNFs from sample C (bottom), for a length scale bar of respectively 10 nm and 5 nm. The electron diffraction pattern for both materials are added. An enlargement of the O-GNFs edges in the bottom right corner shows a structure having 19 graphene planes.

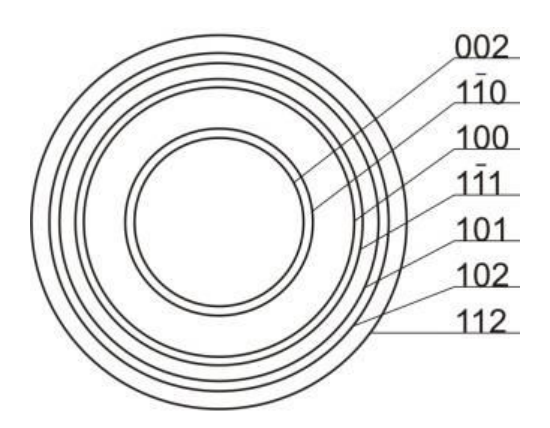


Figure 6-7: Identification of the diffraction pattern for graphitic materials [172].

The Raman spectra provide specific parameters to evaluate the graphitisation of the GNFs; these spectra are given for GNFs and 14.2 at%O-GNFs in Figure 6-8. Four peaks need to be examined when analysing carbon based samples. The D peak, found at 1350 cm⁻¹, provides information on non-graphitized carbon while the G peak, at 1580 cm⁻¹, is associated with the graphitic content of the sample. The G' peak at 2700 cm⁻¹ becomes sharper and intensifies as the number of graphene layers decreases. Finally, the D' peak at 1625 cm⁻¹ associated again to defects in the graphitic structure is an important signature of the quality of well crystallized graphene samples. Observation of this D' elbow for both cases reveals the sharpness of the G peak and confirms the intensity of the G peak is effectively associated to well graphitized structures and not contaminated by the defect content. Observation of a separate D' peak is one of the best signature of a truly graphene sample. One first observation on the Raman spectra of both GNF and 1.2 at%O-GNF is the absence of any strong fluorescence background on both samples when moving to Raman shifts above 2500 cm⁻¹. This highlights the absence of polyaromatic hydrocarbon impurities in the samples. Larouche et al. [120] provided relations to evaluate the purity, the crystallite size (L_a), and the average length of graphene planes (L_{eq}), these values being deduced from the intensity and the underlying area of the D, G, G' peaks (Table 3). In this analysis, La represents the size of planar crystalline zones that do not show defects, while L_{eq} can be seen as an integration of a series of planar structures linked by curvature and forming a graphene equivalent length L_{eq} .

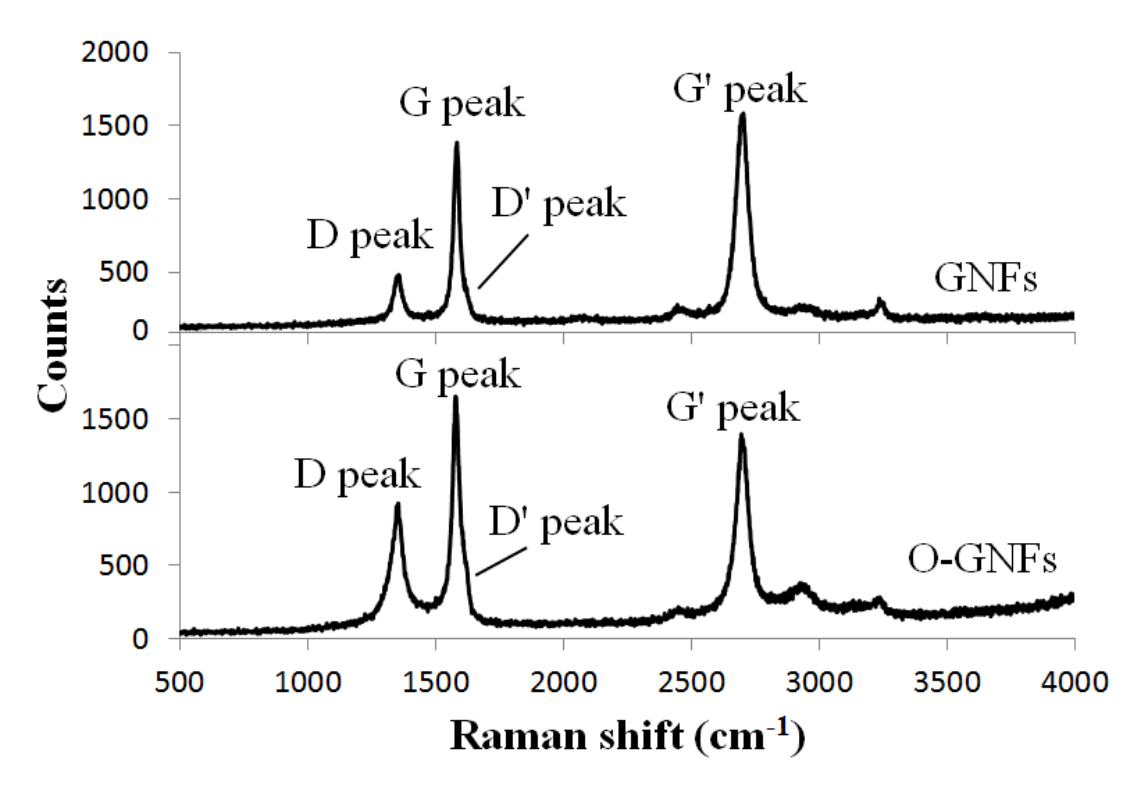


Figure 6-8: Raman spectrum for non-functionalized GNFs (top) and O-GNFs from sample C (bottom).

Table 6-3: Graphitic indices relations and results for non-functionalized GNFs and O-GNFs. The Formula for these evaluations follows from [120].

Indices	Formula	Non- functionalized GNFs	O-GNFs (Sample C)
Purity	$I_{\mathrm{G}}/I_{\mathrm{D}}$	2.83 ± 0.56	1.92 ± 0.17
L _a (nm)	4.44xA _G /A _D	8.76 ± 0.93	6.24 ± 0.29
L _{eq} (nm)	8.8xA _{G'} /A _D	28.16 ± 5.34	14.50 ± 1.65

It can be inferred from the graphitic indices that O-GNFs still have a strong graphitic structure. The oxygen functionalization causes partial damage to the O-GNFs structure by the decrease observed in purity, length of the crystallite and average length of the graphene planes. The different graphitic indices can be compared to other graphitic materials. For L_a and L_{eq} , Larouche *et al.* [120] tested a large variety of carbon blacks, which systematically show lower L_a and L_{eq} than the present GNFs even after the functionalization step. This can be explained by the large proportion of defects and amorphous carbon found in the materials tested by Larouche *et al.* Pure graphite has generally a high I_G/I_D ratio, and the D peak is almost absent for perfect crystallite, while materials mostly containing amorphous carbon have a I_G/I_D lower than 1 [173]. The graphene sheets functionalized by oxygen plasma which are reported in the literature generally present a I_G/I_D lower than 1 [163;167;173], confirming the higher quality of the materials produced here.

3.3. Decomposition temperature

TGA was performed on both non-functionalized GNFs and O-GNFs in order to follow their thermal decomposition under an oxidizing atmosphere (Figure 6-9). Most of the weight loss occurring for the GNFs occurs beyond 700 °C, which can be compared to common carbon materials, such as multiwall carbon nanotubes (550 °C) [175], graphite (650 °C) [176], single graphene sheets (600 °C) [177]. The high temperature resistance of the GNFs denotes the well crystallized structure with no evidence of amorphous carbon. Once functionalized, the O-GNFs start losing around 8 wt% at 200 °C, while the main weight loss is beyond 650 °C which also indicates the purity of the sample and the rather small effect of the oxygen functionalization on the structural integrity of the material. The low temperature weight loss can be most likely explained by the decomposition of the functional groups; this was confirmed by heating a sample of O-GNFs at 400 °C for 10 min, leading to a decrease of about 80% of the oxygen content, passing from 14.2 at%O to 2.5 at%O. The main weight loss

of O-GNFs occurs at a lower temperature for the O-GNFs than for the GNFs. The high amount of initial defects and the defects resulting from the early loss of hydrophilic groups in the material may be responsible of the degradation of the O-GNF nanoparticles at a lower temperature compared to the non-functionalized GNFs.

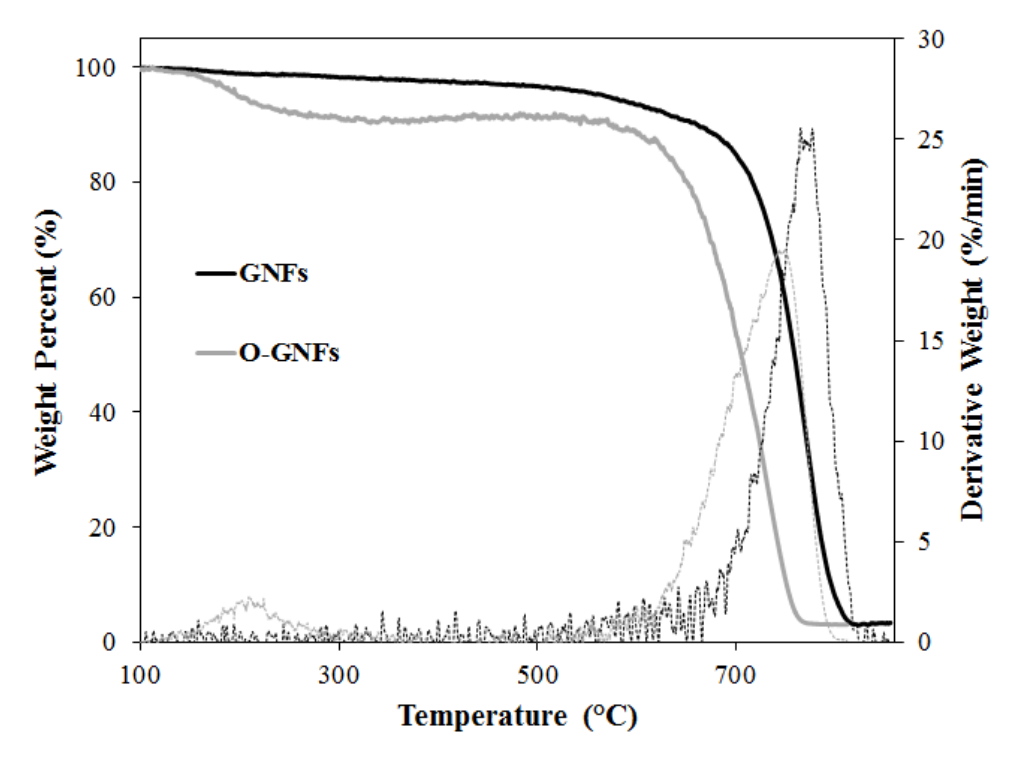


Figure 6-9: TGA profile for 14.2 at%O-GNFs (sample C) and non-functionalized GNFs in full lines with their respective derivative in dash lines.

3.4. Dispersion tests

It has already been shown that in the presence of water, the GNFs do not mix at all and stay at the surface of the liquid [114]. However, the O-GNFs with oxygen contents over 10 at% can be perfectly dispersed in water. No additional treatment to the powders is made and no surfactant is being added, the O-GNF powders are directly added to deionized water after collecting these from the synthesis reactor. The Zeta potential was measured on all the prepared samples (Figure 6-10) as an indication of their stability in water. The Zeta potential enables a quantification of the stability of a suspension by measuring the electrophoretic

mobility of particles in suspension. It is commonly accepted that a Zeta potential of less than -40 mV (or more than + 40 mV) denotes a good stability [178]. A suspension having a Zeta potential between ±10 and ±30 mV is considered as moderately stable; however for samples having Zeta potentials in this range, agglomeration over time is observed.

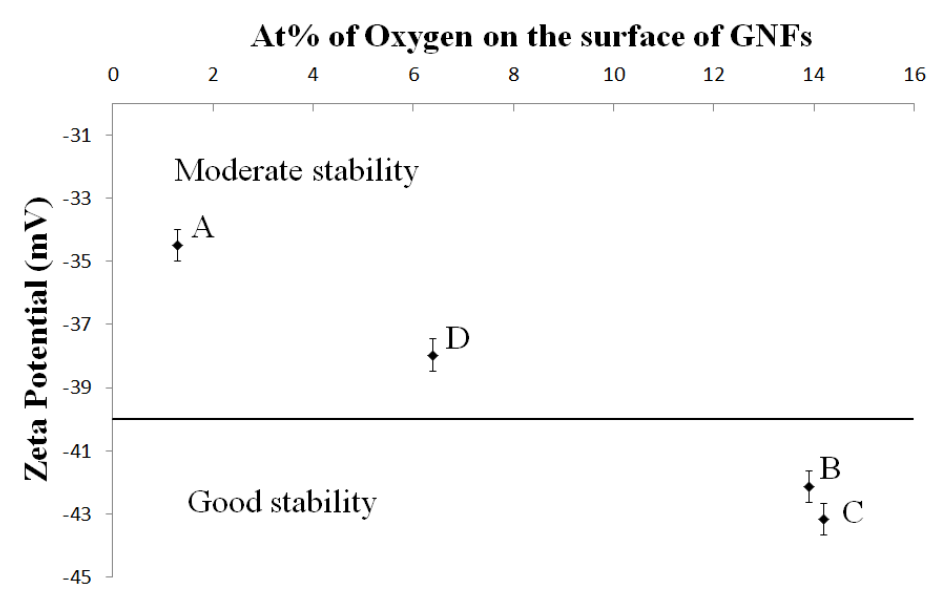


Figure 6-10: Zeta potential measurements for the A, B, C and D samples in a 1 mM NaHCO3 solution.

It was observed in previous work that when GNFs are mixed with ethanol, there is very little stability of the suspension and the material settles to the bottom after several minutes. The O-GNFs with high oxygen content (samples C and D) produced in this work do not exhibit similar behaviour; on the contrary they show excellent stability in both water and ethanol for long time periods. To further confirm this, samples were left undisturbed for 6 weeks and then observed visually (Figure 6-11).

Dispersion tests and visual observation showed that only the samples with the highest oxygen content can be perfectly mixed with water and ethanol. Their stability can be directly attributed to the number of hydrophilic groups on the nanoparticles. If this number of hydrophilic groups is insufficient, the stability of the nanoparticles in water is eventually lost

as seen in Figure 6-11(c). One can also notice that full dispersion is observed in Figure 6-11(a,b), meaning that no GNF is seen floating on top of the nanofluid as is observed in Figure 6-11(c,d). This indicates a full conversion of the material recovered in the reactor into O-GNF that can readily be dispersed in a fluid. It also indicates that the use of a flowing thermal plasma recombination zone enables a functionalization of not only the top layer of the particle bed deposited, but is able to penetrate the porous deposit and functionalize the entire bed.

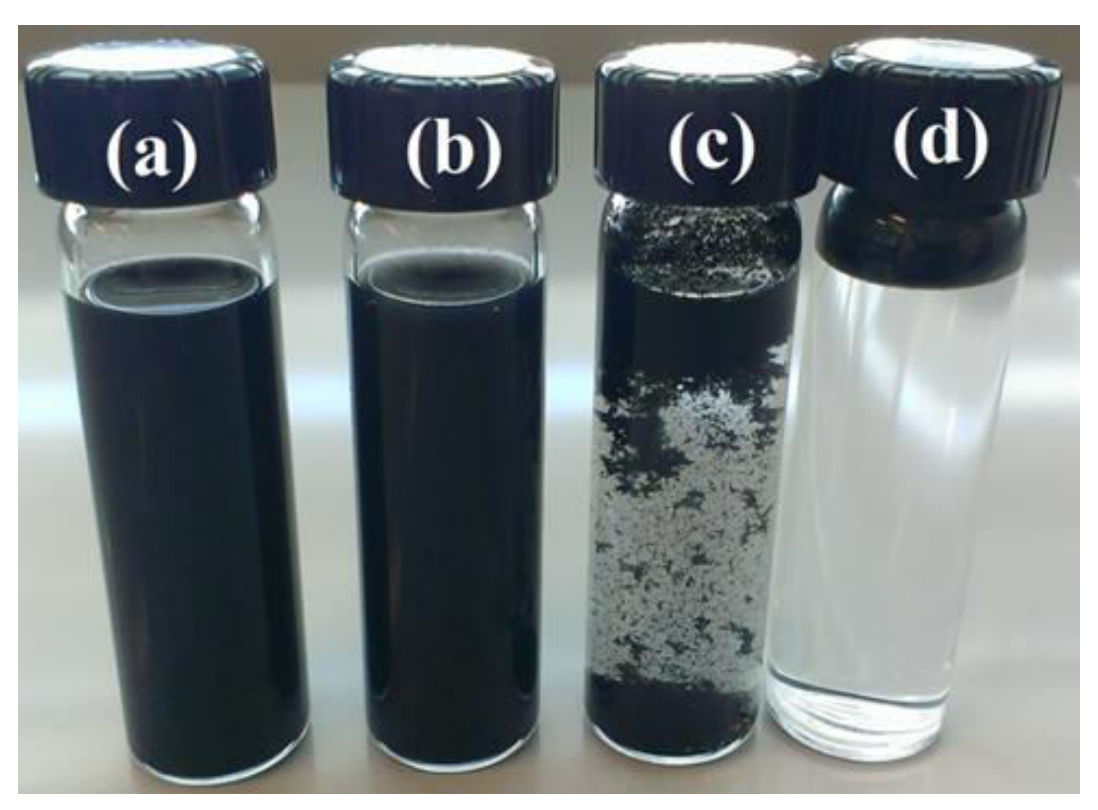


Figure 6-11. Observed stability after 6 weeks for a) O-GNFs with 14.2 at% Oxygen in ethanol b) O-GNFs with 14.2 at% Oxygen in water c) O-GNFs with 6.4 at% Oxygen in water and d) non-functionalized GNFs in water.

4. Conclusion

An original process was presented where highly crystalline graphene powders are grown from homogeneous nucleation and functionalized within the same reactor. Changing the experimental conditions of the functionalization step lead to oxygen content that could be controlled and varied between 0 and 14 at%O. Values above 10 at%O generated fully stable nanofluid suspensions for the full amount of material collected in the reactor, indicating an efficient functionalization is made throughout the porous structure of the graphene powder bed. This functionalization is occurring on nanoparticles located in a cold non-plasma region of the thermal plasma reactor. This indicates that excited species generated in out-ofequilibrium plasma can be maintained and used for functionalization in the low-temperature zone of a controlled thermal plasma expansion. The addition of oxygen atoms at the surface of the nanoparticles increases the amount of defects in the crystalline structure. However, O-GNFs maintain a high purity and crystallinity compared to other graphitic material. Hydrophobic GNFs become hydrophilic and can be stably dispersed in a suspension with a solvent such as water or ethanol. The ability of making a suspension from the treated nanoparticles is directly dependent on the oxygen content, and so on the hydrophilic groups content at the surface of the nanoparticles. Further investigation on the stability of the nanofluids is presently under way.

This study showed the possibility to disperse graphitic material in a polar solvent. The resulting nanofluids can be used in a wide range of applications, or be treated by wet chemistry for grafting atoms or molecules to the GNFs surface or edges.

Part II Additional information on the oxygen functionalization (non-published): Study on the nanofluid stability.

This study focuses on the ability of nanofluids to remain stable over time and over variations in temperature and pH. This study aims to test the limits of stability of the O-GNFs nanofluids and give a comparison with some commercial nanofluids. The tests are performed on the oxygen functionalized graphene nanoflakes (O-GNFS) synthesized by the method described in the previous part and dispersed in polar solvents, as well as commercial nanofluids of graphene oxide (GO) and edge-oxidized graphene (EOG) purchased at Sigma-Aldrich. GO is under the form of single layers, having a lateral diameter up to 100 nm and an oxygen content up to 33 at%. EOG particles consists in stack of 15 to 20 sheets of graphene measuring several micrometers and containing 4 to 10 at% of oxygen on their surface.

The dispersion of powders in a solvent is generally difficult. Suspensions based on large particles are governed by gravity and sedimentation forces. The optimal size for particles to be suspended ranges from nanometers to micrometers. The solid-liquid interaction has to be strong enough to overcome the particles interaction and break the initial agglomerates into individual particles. Different techniques exist to disperse nanoparticles, such as sonication where ultrasounds provide the energy to the particles to separate from each other, but with a risk of damaging them. Particles can be also coated with surfactants which lower the interfacial tension at the liquid-solid interface and facilitate the dispersion. A disadvantage of the surfactant-based dispersions is the low resistance to heating, causing flocculation and sedimentation of the particles. O-GNFs are dispersed in polar solvents instantaneously without the addition of any surfactant, or sonication. That indicates a high affinity of O-GNFs for polar solvents, such as water, ethanol and ethylene glycol.

In this study, the concentration of the tested nanofluids ranges from 5 to 200 mg/L. The commercial nanofluids were sonicated while partial agglomeration has been observed during the storage. The stability of the nanofluids was visually checked but UV-visible spectroscopy gives a quantification of the stability. UV-visible spectroscopy is used here to measure the transmittance of the light, in a wavelength range from 400 to 700 nm, through a known thickness of liquid sample. The nanofluid concentration can be retrieved from the Beer-Lambert law.

$$T = I/I_0 = e^{-\varepsilon XC}$$

where T is the transmittance, ε is the mass extinction coefficient (L.mg⁻¹.cm⁻¹), X is the length of the optical path (cm), and C is the concentration (mg/L).

The absorption coefficient of the materials is first determined from known concentrations suspensions, to be later used to estimate the unknown concentration of nanofluids. One can note that the calculated concentration is an apparent concentration and not the effective concentration. A decrease of the calculated concentration compared to the initial concentration denotes an agglomeration occurring in the suspension, while the effective concentration stays identical.

1. Absorption coefficient of the materials

Beer-Lambert law is generally difficult to apply to particles suspensions, since the particles can diffuse the light, or be shadowed by other particles. To test the validity of the Beer-Lambert law with the suspensions of O-GNFs, GO and EOG; concentrations from 5 to 200 mg/L have been prepared and the transmission has been measured for each. The suspensions with a concentration higher that 50 mg/L were diluted ten times to avoid

extremely low values of transmittance, leading to a larger error. From there, the absorbance coefficient has been calculated and represented in the Figure 6-12.

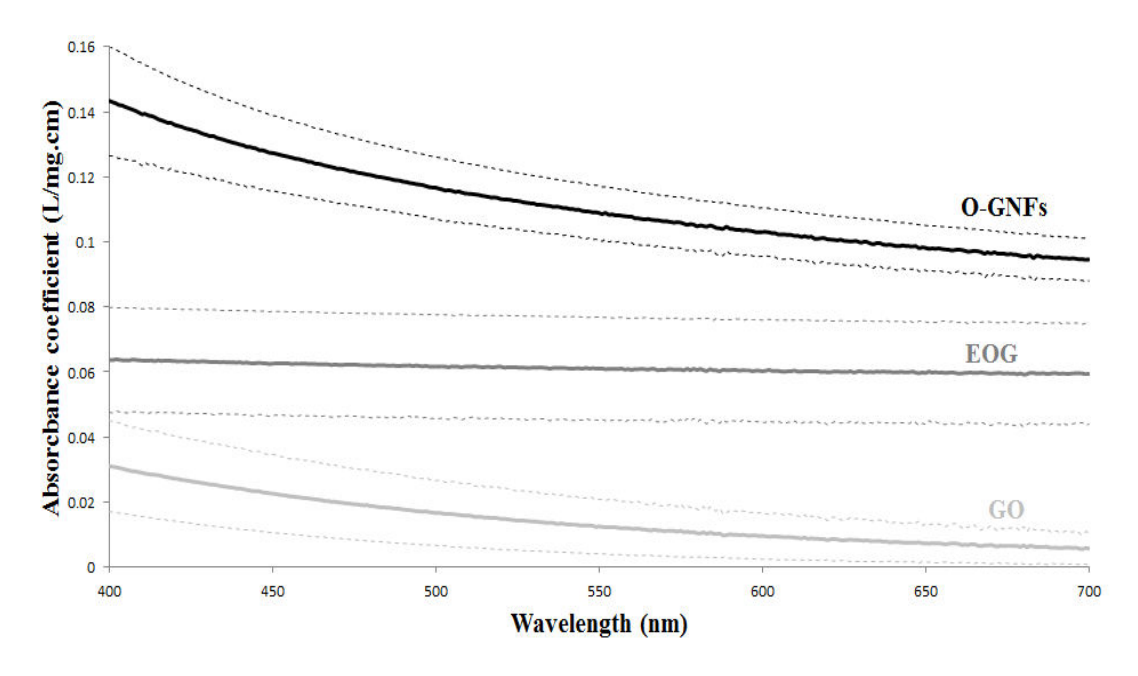


Figure 6-12: Average (15 measurements) of the absorbance coefficient of the O-GNFs, EOG and GO nanofluids with the 95% confidence interval, calculated based on concentrated suspensions from 5 to 200 mg/L.

Graphene nanoflake based nanofluids present the higher absorbance coefficient, while graphene oxide based nanofluids the lowest. The ability of carbon particles to absorb the light can be linked to different parameters, such as the graphitization of the material and the quality of the dispersion. The graphitization refers to the amount of carbon with sp2 bonds, in graphitic structure, in opposition of amorphous carbon having sp3 bonds in a disorganized structure. It has been shown that the unsaturated bonds from graphitic structure have a high light absorption compared to saturated bonds in amorphous carbon [179]. The higher number of defects observed by the Raman analysis in EOG and GO, corresponding to a higher amount of amorphous carbon, can partially explain the low absorbance values for these materials. The other cause for the low absorbance comes from the quality of the dispersion. O-GNFs are immediately dispersed in water without the help of sonication, while

the commercial nanofluids are sonicated to help the dispersion. A partial agglomeration at nanoscale can occur, leading to a lower accessible surface for light absorption, and so a lower absorption coefficient.

2. Stability over the time

The suspensions based on O-GNFs, GO and EOG were prepared at a concentration of 50 mg·L⁻¹ and sonicated before the transmittance was measured. From there, the relative concentration was measured regularly over the next 35 days, and represented in Figure 6-13.

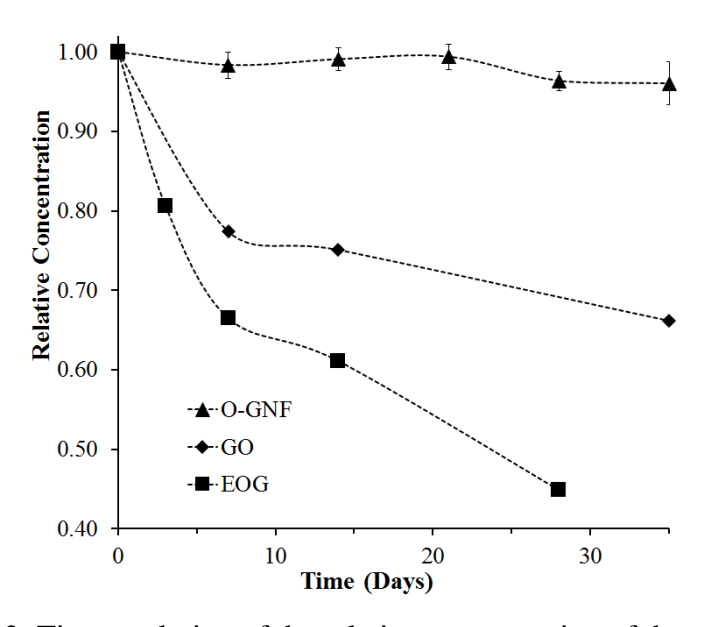


Figure 6-13: Time evolution of the relative concentration of the nanofluids.

O-GNFs nanofluids showed a good stability over the time. No difference was visually observed on the appearance of the nanofluid after 35 days, while the UV-Vis spectroscopy indicated a loss of 5% in the relative concentration. EOG and GO nanofluids were presenting a rapid flocculation after a couple of days, highlighted by a decrease of the relative concentration after 7 days of respectively 35 and 25%.

3. Stability after heating in water

The stability of the aqueous O-GNF nanofluids has been studied after heating at 90°C for one hour. The nanofluid is allowed to cool to ambient temperature. The concentration of the nanofluids is calculated before and after the heating period from the measured transmittance. Nanofluids with concentration from 5 to 200 mg/L are tested. The results for the O-GNFs are presented in Figure 6-14, which shows that the concentration after heating stay close to the concentration before heating, represented by the line at 100%. The error on the measurements mainly takes into account the 95% confidence interval on the absorbance coefficient.

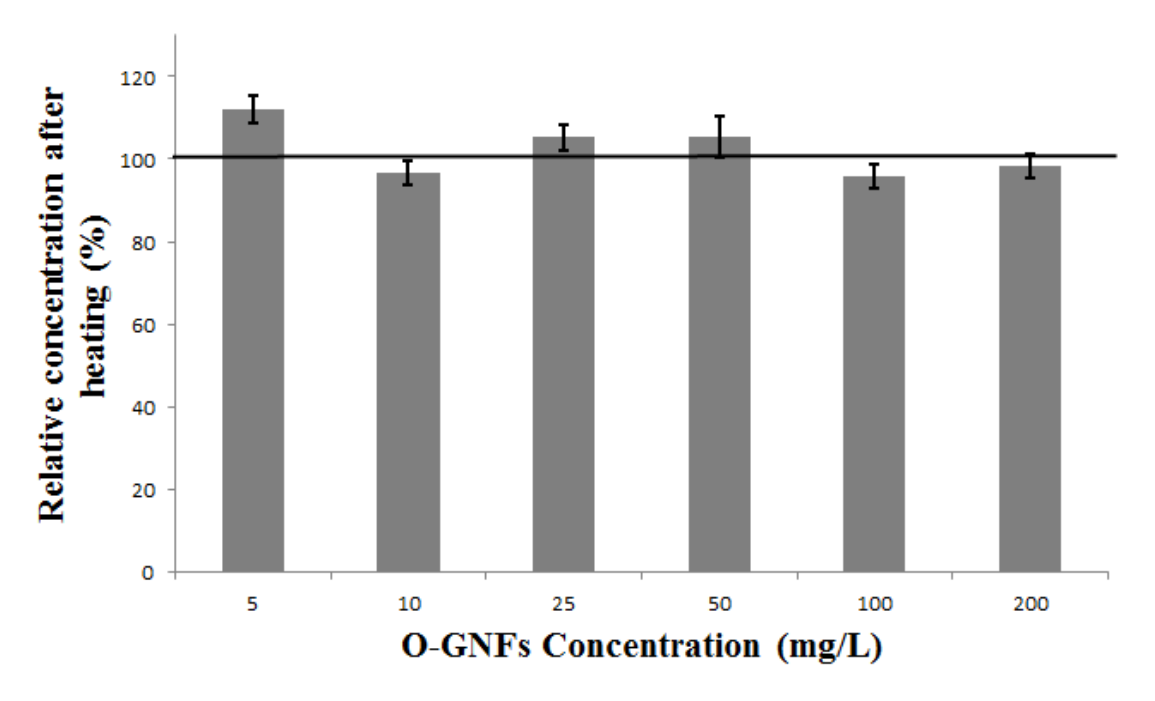


Figure 6-14: Relative concentration of the O-GNFs suspensions in water after heating at 90°C for 1h. The line at 100% represents no change in the concentration before and after the heating step.

The change of concentration after the heating step can be averaged with the concentrations from 5 to 200 mg/L, and compared with the EOG and GO based nanofluids in Figure 6-15. EOG nanofluids remain stable after the heating step, similarly to O-GNFs

nanofluid. The larger error for EOG is due to a larger incertitude on its absorbance coefficient. The apparent concentration for graphene oxide nanofluid is increasing drastically after the heating step. Visually, the concentrated nanofluids pass from yellow/brown to black colour. That can be potentially explained by the reduction of graphene oxide in suspension, where the hydrophilic groups are detached from the material. The change of the colour is due to the graphitization of the material, where the carbon evolves from mostly amorphous form in sp3 configuration to a partially graphitized form in sp2 configuration. The large error on the calculation of the apparent concentration is due to the non-controlled reduction reaction, leading to large variations in the measured transmittance after the heating step.

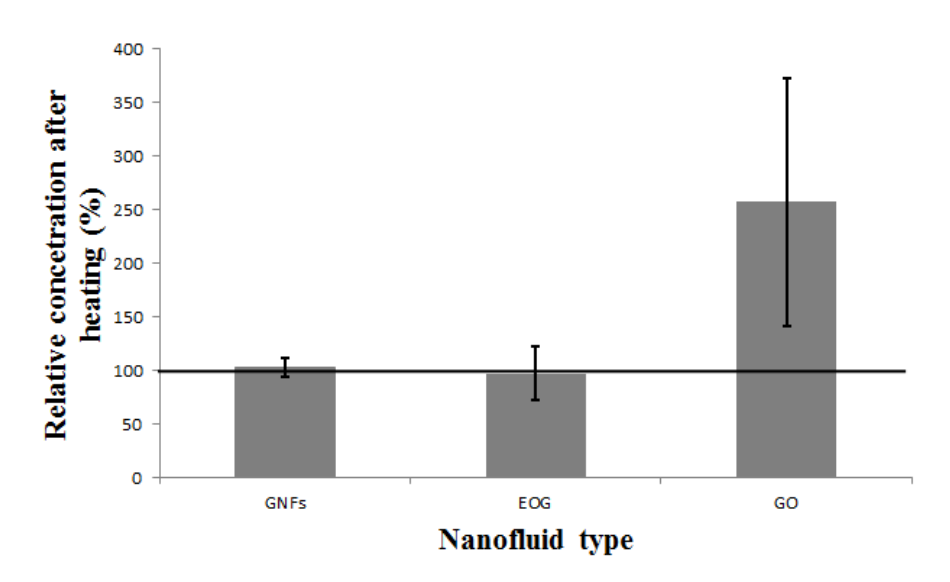


Figure 6-15: Average of the relative concentration of the O-GNFs, EOG and GO nanofluids in water after heating at 90°C for 1h. The line at 100% represents no change in the concentration before and after the heating step.

4. Further characterization of the O-GNFs based nanofluids

Compared to commercial nanofluids containing EOG and GO, O-GNFs based nanofluids presented the highest absorbance coefficient, with the best stability over time and after a heating step, due to a better crystallinity, purity, and dispersion in water. Following these experiments, the dispersion in solvents with a higher boiling point, such as ethylene

glycol, and the stability over a large range of pH was further investigated using O-GNFs nanofluids.

4.1. Stability after heating in Ethylene Glycol

O-GNFs were dispersed in ethylene glycol, C₂H₆O₂, having a boiling point of 197.3 °C. The dispersion of the powder in ethylene glycol required mechanical agitation, due to its higher density and viscosity. Using the same procedure followed for water based nanofluids, the nanofluid has been heated close to the boiling point during one hour, at 178 °C. The transmittance of the nanofluid was measured before and after the heating step for a range of concentration from 5 to 50 mg/L. The relative concentration was calculated and presented in Figure 6-16. The relative concentration was decreased by about 10% after the heating step. The O-GNFs appear to be stable in ethylene glycol after the heating step, with lower performances compared to water based nanofluids. These lower performances can be explained by the nature of the solvent, being less favourable to the O-GNFs and the temperature of the heating step, closer to the degradation temperature of the functionalities on the surface of the nanoparticles, observed on the TGA of the GNFs on Figure 6-9.

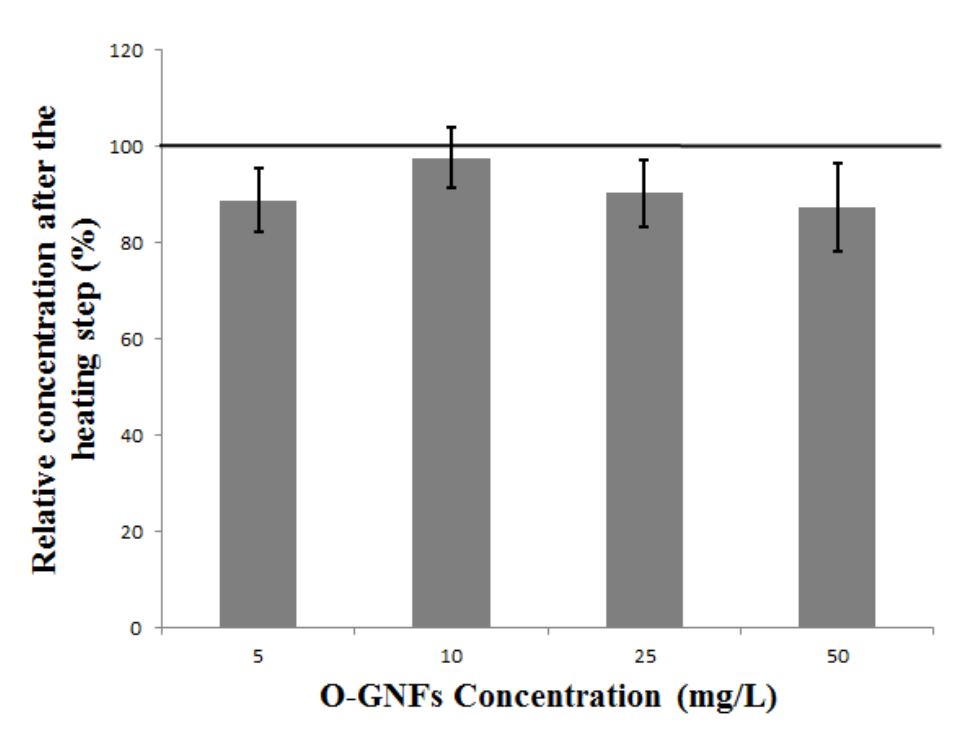


Figure 6-16: Relative concentration of the O-GNFs suspensions in ethylene glycol after heating at 90°C for 1h. The line at 100% represents no change in the concentration before and after the heating step.

4.2. *Influence of the pH on the nanofluid stability*

The O-GNFs are dispersed in water whose pH is controlled between 2 and 12 by changing the concentration of sulfuric acid and sodium hydroxide (10⁻³ to 10⁻⁷ M) for respectively lower and higher pH. Nanofluids from 5 to 200 mg/L are tested the same day than their preparation and their relative concentration is averaged (Figure 6-17). The range of stability of the O-GNFs is between a pH of 4 and 11. For pH lower than 4 or higher than 11, a decrease of 70 to 80% of the relative concentration is observed, and due to a total flocculation of the particles in the liquid. The strong acidic or basic environment at pH lower than 4 or higher than 11 can be correlated with the attack of the oxygen functionalities on the nanoparticles surface, and thus the loss of nanofluids stability.

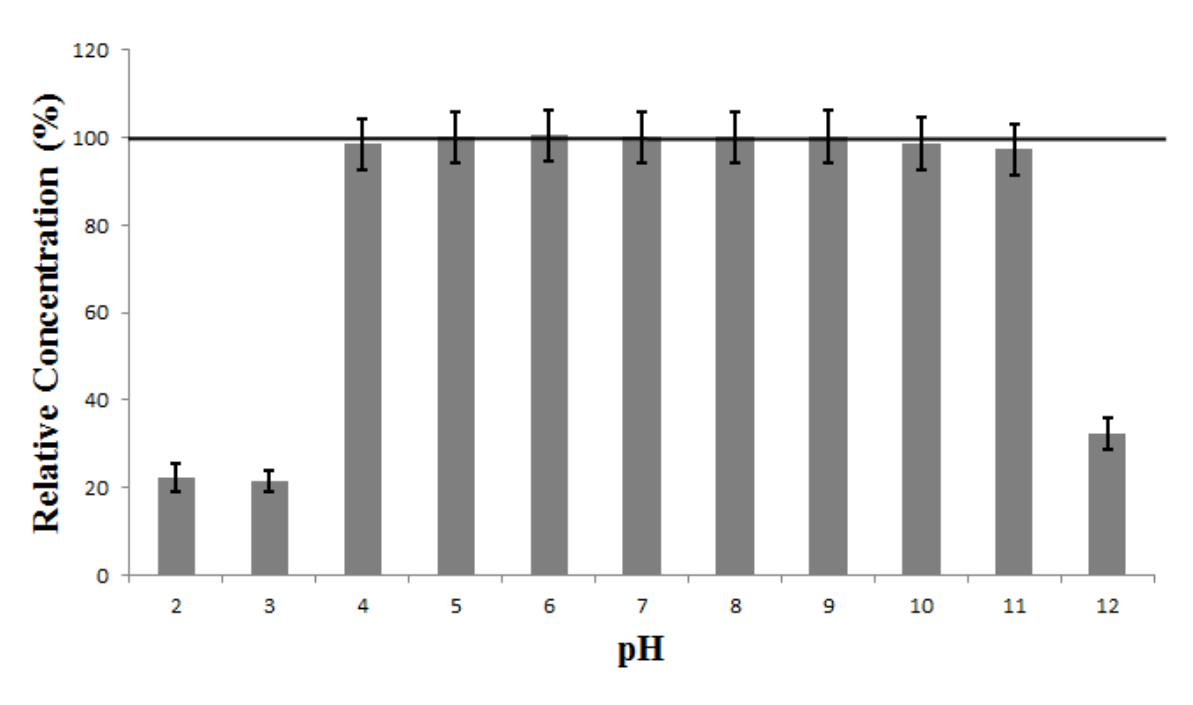


Figure 6-17: Average of the relative concentration of the O-GNFs in water having a range of pH from 2 to 12. The line at 100% represents no change in the concentration.

Chapter 7 CONCLUSION AND RECOMMENDATIONS

1. Conclusion

This Ph.D. thesis aims to develop a functionalization step in the same thermal plasma reactor that is used to grow the graphene nanoflakes in order to modify their surface properties of. The process is explored with the functionalization of the GNFs with iron, sulphur or oxygen. Different methods already exist to treat graphene based materials with such elements, but it is the first time that the growth and functionalization steps are performed in a single batch process. This method also offers other advantages, such as a precise control of the level of functionalities introduced on the GNFs in a bottom-up approach, and a high level of graphitization.

Thermal plasma is particularly appropriate to perform the functionalization step due to the high temperatures and the highly reactive environment of the plasma. The high temperatures allow the precursors to be vaporized and/or decomposed. The control of the plasma conditions allows the generation and transfer of the reactive species to the surface of the deposited GNFs. The reactive species are then able to react with the GNFs, modifying the chemical composition of their surface. The key parameter to optimize the functionalization is generally the residence time of the reactive species in the recombining zone of the plasma. It can be noted that the functionalization process occurs on the full amount of GNFs, which is particularly observed with the O-GNFs. This can be explained by the very porous structure of the deposited GNFs on the water-cooled walls of the reactor, allowing reactive species to reach each nanoparticle.

The functionalized GNFs are effective in their respective applications. Adding iron or sulphur to the GNFs improves the electrocatalytic activity of the samples toward the ORR, making them effective to potentially replace platinum as a catalyst in fuel cells. Also, the addition of oxygen on the surface of the GNFs successfully modifies their natural hydrophobicity into a highly hydrophilic behaviour, making possible the formation of stable nanofluids that are expected to provide optimized inks for the membrane assembly of fuel cells.

2. Original contribution

Several contributions to the fields of plasma functionalization and nanomaterials have been accomplished in this Ph.D. thesis, and are listed below:

- Nanomaterials are synthesized in a single batch method in two processing steps, including growth of the GNFs and functionalization of their surface. No additional processing step is required at the exit of the plasma reactor.
- 2) Changing the power of the ICP torch and the pressure within the plasma reactor modifies the residence time of the reactive species in the thermal plasma. A lower residence time has been linked with higher amount of functionalities incorporated on the surface of the GNFs. Additional parameters to tune the level of functionalization include the duration of the functionalization step, nature of the precursor and the way to feed the precursor in the reactor.
- 3) The addition of functionalities on the surface of the GNFs does not alter much the graphitic structure of the nanoparticles. It suggests that the functionalization of the GNFs is done on the edges and on the existing defects, without creating additional defects. Thus, the crystallinity of the functionalized GNFs remains higher than most of the functionalized graphene based material described in the literature.

- 4) The addition of iron in the form of iron oxide nanoparticles or atomic dispersion improves the electrocatalytic activity of the GNFs toward the ORR. The catalyst with the best performances has been obtained with the iron (II) phthalocyanine as the iron precursor, showing an onset potential of 0.74V and a current density of -2.40 mA.cm⁻² at 0.4V.
- 5) The addition of sulphur during the functionalization step leads to GNFs having sulphur atoms incorporated in the graphitic structure, and covered by a layer of sulphur-based plasma polymer. The S-GNFs also contain traces of orthorhombic sulphur. With the exception of the orthorhombic sulphur, the sulphur functionalities improve the electrocatalytic activity of the nanoparticles for the highest level of sulphur added.
- 6) Oxygen can be added on the surface of the GNFs under the form of functionalities (C=O, C-O, COOH) able to modify the hydrophobicity of the GNFs. At a level of 14 at%, the O-GNFs are fully hydrophilic and can be dispersed into a stable nanofluid without the addition of surfactants. The nanofluid remains stable for weeks, and after being heated for one hour at 90 °C for water and 178 °C for ethylene glycol or being in a pH range between 4 and 11.

3. Recommendations

Different functionalization steps have been realized in this project. Further studies could be done on the developed materials and additional functionalization steps could be explored.

1) The iron-based catalysts having the highest ORR performance should be tested in a fuel cell station. The samples have been tested with RDE, which acts as a screening technique to select the catalyst having the highest electrocatalytic activity among the

- other samples. However, gas diffusion is different in a fuel cell, and the samples should be tested in real conditions.
- 2) The sulphur functionalization step could be modified to produce only GNFs with sulphur atoms incorporated in the graphitic structure or only GNFs covered by the sulphur based plasma polymer. This could be achieved by changing the nature and concentration of the sulphur precursor. For example, the injection of a sulphur precursor containing no carbon, such as H₂S in low concentration would prevent the formation of the sulphur based plasma polymer.
- 3) The GNFs offering a good catalyst support, platinum based catalyst could be synthesized in the thermal plasma reactor following the same protocol employed during the thesis. Indeed, a platinum precursor in solid or solution form could be injected during the functionalization step to allow the growth and deposition of platinum nanoparticles on the GNFs surface. The resulting catalyst could then be tested and compared to commercial platinum based catalysts, and the catalysts developed in this thesis.
- 4) The O-GNFs based nanofluid could be studied in terms of their thermal conductivity. Well documented techniques such as the transient hot-wire would be suitable for the study of the O-GNFs nanofluid thermal conductivity.

REFERENCES

- [1] K.S. Novoselov, D. Jiang, F. Schedin, T.J. Booth, V. V Khotkevich, S. V Morozov, A.K. Geim, Two-dimensional atomic crystals, Proc. Natl. Acad. Sci. U. S. A. 102 (2005) 10451–10453. doi:10.1073/pnas.0502848102.
- [2] W. Choi, I. Lahiri, R. Seelaboyina, Y.S. Kang, Synthesis of Graphene and Its Applications: A Review, Crit. Rev. Solid State Mater. Sci. 35 (2010) 52–71. doi:10.1080/10408430903505036.
- [3] T.O. Wehling, K.S. Novoselov, S. V Morozov, E.E. Vdovin, Molecular Doping of Graphene, (2008) 0–4.
- [4] F. Bonaccorso, A. Lombardo, T. Hasan, Z. Sun, L. Colombo, A.C. Ferrari, Production and processing of graphene and 2d crystals, Mater. Today. 15 (2012) 564–589. doi:10.1016/S1369-7021(13)70014-2.
- [5] C. Gomez-Navarro, J.C. Meyer, R.S. Sundaram, A. Chuvilin, S. Kurasch, M. Burghard, K. Kern, U. Kaiser, Atomic Structure of Reduced Graphene Oxide, Nanoletters. (2010) 1144–1148. doi:10.1021/nl9031617.
- [6] R. Pristavita, J.L. Meunier, D. Berk, Carbon nano-flakes produced by an inductively coupled thermal plasma system for catalyst applications, Plasma Chem. Plasma Process. 31 (2011) 393–403. doi:10.1007/s11090-011-9289-0.
- [7] A.H.C. Neto, F. Guinea, N.M.R. Peres, K.S. Novoselov, A.K. Geim, The electronic properties of graphene, Rev. Mod. Phys. 81 (2009) 109–162. doi:10.1103/RevModPhys.81.109.
- [8] D.M. Binny, J.L. Meunier, D. Berk, Nitrogen doping of graphene nanoflakes by thermal plasma as catalyst for oxygen reduction in Proton Exchange Membrane fuel cells, Proc. IEEE Conf. Nanotechnol. (2012) 5–10. doi:10.1109/NANO.2012.6322208.
- [9] P.-A. Pascone, D. Berk, J.-L. Meunier, A stable and active iron catalyst supported on graphene nano-flakes for the oxygen reduction reaction in polymer electrolyte membrane fuel cells, Catal. Today. 211 (2013) 162–167. doi:10.1016/j.cattod.2013.03.026.
- [10] A. Piel, Plasma physics: An introduction to laboratory, space, and fusion plasmas, Plasma Phys. An Introd. to Lab. Space, Fusion Plasmas. (2010) 1–398. doi:10.1007/978-3-642-10491-6.
- [11] C. Tendero, C. Tixier, P. Tristant, J. Desmaison, P. Leprince, Atmospheric Pressure Plasmas: A Review, Spectrochem. Acta Part B. 61 (2006) 2–30. doi:10.1016/j.sab.2005.10.003.
- [12] H. Conrads, M. Schmidt, Plasma generation and plasma sources, Plasma Sources Sci. Technol. 9 (2000) 441–454. doi:10.1088/0963-0252/9/4/301.
- [13] H. Herman, Plasma-sprayed Coatings, (1988) 112–117.
- [14] C.H. Liebert, R.E. Jacobs, S. Stecura, C.R. Morse, C. Liebert, R.E. Jacobs, S. Stecura,

- C.R. Morse, Durability of Zirconia Thermal-Barrier Ceramic Coatings on Air-Cooled Turbine Blades in Cyclic Jet Engine Operation, Nasa Tech. Memo. (1976).
- [15] M. Boulos, Plasma power can make better powders, Met. Powder Rep. 59 (2004) 16–21. doi:10.1016/S0026-0657(04)00153-5.
- [16] L. Xie, M. Dorfman, A. Patel, M. Mueller, Method for making high purity and free flowing metal oxides powder, 2011.
- [17] J. Heberlein, A.B. Murphy, Thermal plasma waste treatment, J. Phys. D. Appl. Phys. 41 (2008) 53001. doi:10.1088/0022-3727/41/5/053001.
- [18] P. Convertors, Thermal Destruction of Waste, (2010) 1–5.
- [19] E. Gomez, D.A. Rani, C.R. Cheeseman, D. Deegan, M. Wise, A.R. Boccaccini, Thermal plasma technology for the treatment of wastes: A critical review, J. Hazard. Mater. 161 (2009) 614–626. doi:10.1016/j.jhazmat.2008.04.017.
- [20] E. Pfender, Thermal plasma technology: Where do we stand and where are we going?, Plasma Chem. Plasma Process. 19 (1999) 1–31. doi:10.1023/A:1021899731587.
- [21] N.Y. Mendoza-Gonzalez, M. El Morsli, P. Proulx, Production of Nanoparticles in Thermal Plasmas: A Model Including Evaporation, Nucleation, Condensation, and Fractal Aggregation, J. Therm. Spray Technol. 17 (2008) 533–550. doi:10.1007/s11666-008-9209-x.
- [22] N. Rao, S. Girshick, J. Heberlein, P. McMurry, S. Jones, D. Hansen, B. Micheel, Nanoparticle Formation Using a Plasma Expansion Process, Plasma Chem. Plasma Process. 15 (1995).
- [23] S.L. Girshick, C.-P. Chiu, C.Y. Wu, L. Yang, S.K. Singh, P.H. Mcmurry, Thermal plasma synthesis of ultrafine iron particles, J. Aerosol Sci. 24 (1993) 367–382.
- [24] F. Fabry, G. Flamant, L. Fulcheri, Carbon black processing by thermal plasma. Analysis of the particle formation mechanism, Chem. Eng. Sci. 56 (2001) 2123–2132. doi:10.1016/S0009-2509(00)00486-3.
- [25] A. Malesevic, R. Vitchev, K. Schouteden, A. Volodin, L. Zhang, G. Van Tendeloo, A. Vanhulsel, C. Van Haesendonck, Synthesis of few-layer graphene via microwave plasma-enhanced chemical vapour deposition., Nanotechnology. 19 (2008) 305604. doi:10.1088/0957-4484/19/30/305604.
- [26] M. Meyyappan, L. Delzeit, A. Cassell, D. Hash, Carbon nanotube growth by PECVD: a review, Plasma Sources Sci. Technol. 12 (2003) 205–216. doi:10.1088/0963-0252/12/2/312.
- [27] D. Harbec, J. Meunier, Growth of carbon nanotubes above the peritectic temperature of tungsten metal catalyst, Carbon N. Y. 49 (2011) 2206–2215. doi:10.1016/j.carbon.2011.01.050.
- [28] J.L. Meunier, N.Y. Mendoza-Gonzalez, R. Pristavita, D. Binny, D. Berk, Two-Dimensional Geometry Control of Graphene Nanoflakes Produced by Thermal Plasma for Catalyst Applications, Plasma Chem. Plasma Process. (2014) 505–521. doi:10.1007/s11090-014-9524-6.
- [29] A. Felten, C. Bittencourt, J.J. Pireaux, G. Van Lier, J.C. Charlier, Radio-frequency plasma functionalization of carbon nanotubes surface O 2, NH 3, and CF 4 treatments, J. Appl. Phys. 98 (2005). doi:10.1063/1.2071455.

- [30] F. Denes, S. Manolache, L.E. Cruz-barba, M. Lagally, B. Larson, Plasma-Enhanced Functionalization of Carbon-Containing Substrates, 2007.
- [31] D. Bodas, C. Khan-malek, Hydrophilization and hydrophobic recovery of PDMS by oxygen plasma and chemical treatment An SEM investigation, Sensors Actuators B. 123 (2007) 368–373. doi:10.1016/j.snb.2006.08.037.
- [32] K.W.H.A. Oh, S.H.U.N. Kim, E.U.N.A.E. Kim, Improved Surface Characteristics and the Conductivity of Polyaniline – Nylon 6 Fabrics by Plasma Treatment, J. Appl. Polym. Sci. (2001) 684–694.
- [33] A. Nourbakhsh, M. Cantoro, T. Vosch, G. Pourtois, F. Clemente, M.H. Van Der Veen, J. Hofkens, M.M. Heyns, S. De Gendt, B.F. Sels, Bandgap opening in oxygen plasmatreated graphene, Nanotechnology. 21 (2010). doi:10.1088/0957-4484/21/43/435203.
- [34] N. Hordy, S. Coulombe, J.L. Meunier, Plasma functionalization of carbon nanotubes for the synthesis of stable aqueous nanofluids and poly(vinyl alcohol) nanocomposites, Plasma Process. Polym. 10 (2013) 110–118. doi:10.1002/ppap.201200075.
- [35] H.O. Pierson, HANDBOOK OF CARBON, GRAPHITE, DIAMOND AND FULLERENES by, (n.d.).
- [36] G.A. Slack, Anisotropic Thermal Conductivity of Pyrolytic Graphite, Physocal Rev. 127 (1962).
- [37] A. V. Tamashausky, An Introduction to Synthetic Graphite., 2006.
- [38] P.J.F. Harris, Carbon Nanotubes and Related Strutures: New Materials for the Twenty-first Century, 1999.
- [39] M. Moreno-Couranjou, M. Monthioux, J. Gonzalez-Aguilar, L. Fulcheri, A non-thermal plasma process for the gas phase synthesis of carbon nanoparticles, Carbon N. Y. 47 (2009) 2310–2321. doi:10.1016/j.carbon.2009.04.003.
- [40] J.-B. Donnet, A. Voet, Carbon black: Physics, Chemistry, and Elastomer Reinforcement, 1976.
- [41] J.C. Krejci, Furnace carbon black process and apparatus, 1958.
- [42] B. Clau, Fibers for Ceramic Matrix Composites, (2008) 1–20.
- [43] L. Fulcheri, Y. Schwob, G. Flamant, Comparison between new carbon nanostructures produced by plasma with industrial carbon blacks grades, J. Phys. III Fr. 7 (1997) 491–503.
- [44] M. Akaishi, H. Kanda, S. Yamaoka, Synthesis of diamond from graphite-carbonate systems under very high temperature and pressure, J. Cryst. Growth. 104 (1990) 578–581.
- [45] J.O. Berghaus, J.L. Meunier, F. Gitzhofer, Local growth studies of CVD diamond using a probe-like substrate, IEEE Trans. Plasma Sci. 25 (1997) 1058–1065. doi:10.1109/27.649626.
- [46] O. Berghaus, J. Meunier, Monitoring and control of RF thermal plasma diamond deposition via substrate, 161 (n.d.). doi:10.1088/0957-0233/15/1/023.
- [47] M. Kamo, Y. Sato, S. Matsumoto, N. Setaka, Diamond synthesis from gas phase in microwave plasma, J. Cryst. Growth. 62 (1983) 642–644.
- [48] N. Ohtake, M. Yoshikawa, Diamond film preparation by arc discharge plasma jet

- chemical vapor deposition in the methane atmosphere, J. Electrochem. Soc. 137 (1990) 717–722.
- [49] K. Okano, K.K. Gleason, Electron emission from phosphorus- and boron-doped polucrystalline diamond films, Electron. Lett. 31 (1995) 74–75.
- [50] B.E.I. Peng, M. Locascio, P. Zapol, S. Li, S.L. Mielke, G.C. Schatz, H.D. Espinosa, Measurements of near-ultimate strength for multiwalled carbon nanotubes and irradiation-induced crosslinking improvements, Nat. Nanotechnol. 3 (2008) 626–631. doi:10.1038/nnano.2008.211.
- [51] M.S. Dresselhaus, G. Dresselhaus, P. Avouris, Carbon Nanotubes: Synthesis, Structure, Properties, and Applications, 201AD.
- [52] T. Guo, P. Nikolaev, A. Thess, D.T. Colbert, R.E. Smalley, Catalytic growth of single-walled nanotubes by laser vaporization, Chem. Physics Lett. 243 (1995) 49–54.
- [53] Y. Ando, X. Zhao, Synthesis of Carbon Nanotubes by Arc-Discharge Method, New Diam. Forntier Carbon Technol. 16 (2006) 123–137. doi:10.7209/tanso.2006.347.
- [54] D. Harbec, Producing Carbon Nanotubes using the technology of DC Thermal Plasma Torch, McGill University, 2006.
- [55] D. Harbec, J. Meunier, Method for producing carbon nanotubes using a DC non-transferred thermal plasma torch, Patent US7846414 B2, 2010.
- [56] G.-P. Dai, J.-L. Meunier, Large-scale continuous synthesis of high purity carbon nanotubes in a DC thermal plasma torch reactor, in: 18th Int. Symp. Plasma Chem., Kyoto, 2007.
- [57] D. Venegoni, P. Serp, R. Feurer, Y. Kihn, C. Vahlas, P. Kalck, Parametric study for the growth of carbon nanotubes by catalytic chemical vapor deposition in a fluidized bed reactor, Carbon N. Y. 40 (2002) 1799–1807.
- [58] C.E. Baddour, Direct growth of carbon nanotubes on metal surfaces without an external catalyst and nanocomposite production, 2010.
- [59] C.E. Baddour, F. Fadlallah, D. Nasuhoglu, R. Mitra, L. Vandsburger, J. Meunier, A simple thermal CVD method for carbon nanotube synthesis on stainless steel 304 without the addition of an external catalyst, Carbon N. Y. 47 (2008) 313–318. doi:10.1016/j.carbon.2008.10.038.
- [60] N. Hordy, N.Y. Mendoza-Gonzalez, S. Coulombe, J.L. Meunier, The effect of carbon input on the morphology and attachment of carbon nanotubes grown directly from stainless steel, Carbon N. Y. 63 (2013) 348–357. doi:10.1016/j.carbon.2013.06.089.
- [61] M.C. Wang, C. Yan, L. Ma, N. Hu, M.W. Chen, Effect of defects on fracture strength of graphene sheets, Comput. Mater. Sci. 54 (2012) 236–239. doi:10.1016/j.commatsci.2011.10.032.
- [62] A. Reina, X. Jia, J. Ho, D. Nezich, H. Son, V. Bulovic, M.S. Dresselhaus, J. Kong, K.S.K.S. Kim, Y. Zhao, H. Jang, S.Y. Lee, J.M. Kim, J.-H. Ahn, P. Kim, J.-Y. Choi, B.H. Hong, Large-scale pattern growth of graphene films for stretchable transparent electrodes., Nano Lett. 9 (2009) 30–35. doi:10.1038/nature07719.
- [63] C. Mattevi, H. Kim, M. Chhowalla, A review of chemical vapour deposition of graphene on copper, J. Mater. Chem. 21 (2011) 3324–3334. doi:10.1039/c0jm02126a.
- [64] S. Pei, H.M. Cheng, The reduction of graphene oxide, Carbon N. Y. 50 (2012) 3210–

- 3228. doi:10.1016/j.carbon.2011.11.010.
- [65] R.T. Weitz, A.M. Bittner, M. Scolari, A. Mews, M. Burghard, K. Kern, M. Festkoerperforschung, Electronic Transport Properties of Individual Chemically Reduced Graphene Oxide Sheets, Nano Lett. 7 (2007) 3499–3503.
- [66] A. Reina, X. Jia, J. Ho, D. Nezich, H. Son, V. Bulovic, M.S. Dresselhaus, J. Kong, Large Area, Few-Layer Graphene Films on Arbitrary Substrates by Chemical Vapor Deposition, Nano Lett. 9 (2009) 30–35.
- [67] G. Wang, B. Wang, J. Park, Y. Wang, B. Sun, J. Yao, Highly efficient and large-scale synthesis of graphene by electrolytic exfoliation, Carbon N. Y. 47 (2009) 3242–3246. doi:10.1016/j.carbon.2009.07.040.
- [68] L. Carrette, K.A. Friedrich, U. Stimming, Fuel Cells: Principles, Types, Fuels, and Applications, ChemPhysChem. 1 (2000) 162–193. doi:10.1002/1439-7641(20001215)1:4<162::AID-CPHC162>3.0.CO;2-Z.
- [69] H. Sotouchi, A. Hagiwara, Phosphoric Acid Fuel Cells, in: Energy Carriers Convers. Syst., 2009: p. 436.
- [70] N. Sammes, R. Bove, K. Stahl, Phosphoric acid fuel cells: Fundamentals and applications, Solid State Mater. Sci. 8 (2004) 372–378. doi:10.1016/j.cossms.2005.01.001.
- [71] A.L. Dicks, Molten carbonate fuel cells, Solid State Mater. Sci. 8 (2004) 379–383. doi:10.1016/j.cossms.2004.12.005.
- [72] R.M. Ormerod, Solid oxide fuel cells, R. Soc. Chem. 32 (2003) 17–28. doi:10.1039/b105764m.
- [73] Y. Wang, K.S. Chen, J. Mishler, S. Chan, X. Cordobes, A review of polymer electrolyte membrane fuel cells: Technology, applications, and needs on fundamental research, Appl. Energy. 88 (2011) 981–1007. doi:10.1016/j.apenergy.2010.09.030.
- [74] G. McLean, An assessment of alkaline fuel cell technology, Int. J. Hydrogen Energy. 27 (2002) 507–526. doi:10.1016/S0360-3199(01)00181-1.
- [75] C. Song, J. Zhang, Electrocatalytic Oxygen Reduction Reaction, PEM Fuel Cell Electrocatal. Catal. Layers. (2008) 89–134. doi:10.1007/978-1-84800-936-3_2.
- [76] E. Gülzow, Alkaline Fuel Cells, Fuel Cells. 4 (2004) 251–255. doi:10.1002/fuce.200400042.
- [77] J.C. Amphlett, R.M. Baumert, R.F. Mann, B. a Peppley, P.R. Roberge, A. Rodrigues, The effect of Carbon Monoxide contamination on Anode Efficiency in PEM Fuel Cells, Energy Convers. Eng. Conf. 1997. IECEC-97., Proc. 32nd Intersoc. (1997) 1477–1482. doi:10.1109/IECEC.1997.660236.
- [78] Z. Wu, S. Yang, Y. Sun, K. Parvez, X. Feng, K. Müllen, 3D nitrogen-doped graphene aerogel-supported Fe3O4 nanoparticles as efficient electrocatalysts for the oxygen reduction reaction., J. Am. Chem. Soc. 134 (2012) 9082–5. doi:10.1021/ja3030565.
- [79] Y. Liang, Y. Li, H. Wang, J. Zhou, J. Wang, T. Regier, H. Dai, Co3O4 Nanocrystals on Graphene as a Synergistic Catalyst for Oxygen Reduction Reaction, Nat. Mater. 10 (2011) 780–786. doi:10.1038/nmat3087.
- [80] R. Jasinski, A New Fuel Cell Cathode Catalyst, Nature. 201 (1964) 1212–1213. doi:10.1038/2011212a0.

- [81] G. Lalande, G. Faubert, R. Cote, D. Guay, J.P. Dodelet, L.T. Weng, P. Bertrand, Catalytic activity and stability of heat-treated iron phthalocyanines for the electroreduction of oxygen in polymer electrolyte fuel cells, J. Power Sources. 61 (1996) 227–237. doi:10.1016/s0378-7753(96)02356-7.
- [82] M. Lefèvre, E. Proietti, F. Jaouen, J. Dodelet, Iron-based catalysts with improved oxygen reduction activity in polymer electrolyte fuel cells, Science. 324 (2009). doi:10.1038/ncomms1427.
- [83] U.I. Kramm, J. Herranz, N. Larouche, T.M. Arruda, M. Lefèvre, F. Jaouen, P. Bogdanoff, S. Fiechter, I. Abs-Wurmbach, S. Mukerjee, J.-P. Dodelet, Structure of the catalytic sites in Fe/N/C-catalysts for O2-reduction in PEM fuel cells., Phys. Chem. Chem. Phys. 14 (2012) 11673–88. doi:10.1039/c2cp41957b.
- [84] F. Charreteur, F. Jaouen, S. Ruggeri, J. Dodelet, Fe / N / C non-precious catalysts for PEM fuel cells: Influence of the structural parameters of pristine commercial carbon blacks on their activity for oxygen reduction, Electrochim. Acta. 53 (2008) 2925–2938. doi:10.1016/j.electacta.2007.11.002.
- [85] E.J. Biddinger, D. Von Deak, U.S. Ozkan, Nitrogen-containing carbon nanostructures as oxygen-reduction catalysts, Top. Catal. 52 (2009) 1566–1574. doi:10.1007/s11244-009-9289-y.
- [86] Z. Yang, Z. Yao, G. Li, G. Fang, H. Nie, Z. Liu, X. Zhou, X. Chen, S. Huang, Sulfurdoped graphene as an efficient metal-free cathode catalyst for oxygen reduction, ACS Nano. 6 (2012) 205–211. doi:10.1021/nn203393d.
- [87] F. Razmjooei, K.P. Singh, M.Y. Song, J.S. Yu, Enhanced electrocatalytic activity due to additional phosphorous doping in nitrogen and sulfur-doped graphene: A comprehensive study, Carbon N. Y. 78 (2014) 257–267. doi:10.1016/j.carbon.2014.07.002.
- [88] Z.-H. Sheng, H.-L. Gao, W.-J. Bao, F.-B. Wang, X.-H. Xia, Synthesis of boron doped graphene for oxygen reduction reaction in fuel cells, J. Mater. Chem. 22 (2012) 390–395. doi:10.1039/C1JM14694G.
- [89] L. Zhang, J. Niu, M. Li, Z. Xia, Catalytic mechanisms of sulfur-doped graphene as efficient oxygen reduction reaction catalysts for fuel cells, J. Phys. Chem. C. 118 (2014) 3545–3553. doi:10.1021/jp410501u.
- [90] R. Kamatchi, S. Venkatachalapathy, Parametric study of pool boiling heat transfer with nanofluids for the enhancement of critical heat flux: A review, Int. J. Therm. Sci. 87 (2015) 228–240. doi:10.1155/2012/435873.
- [91] J. Veilleux, The Hydrodynamics of Mass Diffusion Enhancement in Nanofluids, PhD Thesis, McGill University (2010).
- [92] R. Saidur, K.Y. Leong, H.A. Mohammad, A review on applications and challenges of nanofluids, Renew. Sustain. Energy Rev. 15 (2011) 1646–1668. doi:10.1016/j.rser.2010.11.035.
- [93] N. Hordy, D. Rabilloud, J. Meunier, S. Coulombe, High temperature and long-term stability of carbon nanotube nanofluids for direct absorption solar thermal collectors, Sol. ENERGY. 105 (2014) 82–90. doi:10.1016/j.solener.2014.03.013.
- [94] I. Sharifi, H. Shokrollahi, S. Amiri, Ferrite-based magnetic nanofluids used in hyperthermia applications, J. Magn. Magn. Mater. 324 (2012) 903–915.

- doi:10.1016/j.jmmm.2011.10.017.
- [95] W. Yu, H. Xie, A Review on Nanofluids: Preparation, Stability Mechanisms, and Applications, J. Nanomater. (2012). doi:10.1155/2012/435873.
- [96] TEKNA website, (n.d.). http://www.tekna.com/.
- [97] M.I. Boulos, P. Fauchais, E. Pfender, Thermal plasmas: fundamentals and applications, Springer Science & Business Media, 2013.
- [98] R. Pristavita, The Synthesis and Functionalization of Nanostructured Carbon Black by Thermal Plasma for Use in PEM Fuel Cells, (2011).
- [99] D.M.. Binny, Plasma Functionalization of Graphene Nanoflakes for Non-Noble Catalyst in Fuel Cells, McGill University, Master thesis, 2013.
- [100] J.-H. Wee, Applications of proton exchange membrane fuel cell systems, Renew. Sustain. Energy Rev. 11 (2007) 1720–1738. doi:10.1016/j.rser.2006.01.005.
- [101] V. Tripkovic, E. Skulason, S. Siahrostami, J.K. Norskov, J. Rossmeisl, The oxygen reduction reaction mechanism on Pt(111) from density functional theory calculations, Electrochim. Acta. 55 (2010) 7975–7981. doi:10.1016/j.electacta.2010.02.056.
- [102] L. Zhang, J. Zhang, D.P. Wilkinson, H. Wang, Progress in preparation of non-noble electrocatalysts for PEM fuel cell reactions, J. Power Sources. 156 (2006) 171–182. doi:10.1016/j.jpowsour.2005.05.069.
- [103] K. Niu, B. Yang, J. Cui, J. Jin, X. Fu, Q. Zhao, J. Zhang, Graphene-based non-noble-metal Co/N/C catalyst for oxygen reduction reaction in alkaline solution, J. Power Sources. 243 (2013) 65–71. doi:10.1016/j.jpowsour.2013.06.007.
- [104] H.R. Byon, J. Suntivich, Y. Shao-Horn, Graphene-based non-noble-metal catalysts for oxygen reduction reaction in acid, Chem. Mater. 23 (2011) 3421–3428. doi:10.1021/cm2000649.
- [105] X. Zhang, W. Ouyang, D. Zeng, Y. Zhan, F. Xie, W. Zhang, J. Chen, H. Meng, Nitrogen doped sublimed carbon as non-noble metal catalyst for oxygen reduction reaction, Catal. Today. (2015). doi:10.1016/j.cattod.2015.07.009.
- [106] C.W.B. Bezerra, L. Zhang, K. Lee, H. Liu, A.L.B. Marques, E.P. Marques, H. Wang, J. Zhang, A review of Fe-N/C and Co-N/C catalysts for the oxygen reduction reaction, Electrochim. Acta. 53 (2008) 4937–4951. doi:10.1016/j.electacta.2008.02.012.
- [107] Z. Wang, C.J. Liu, Preparation and application of iron oxide/graphene based composites for electrochemical energy storage and energy conversion devices: Current status and perspective, Nano Energy. 11 (2015) 277–293. doi:10.1016/j.nanoen.2014.10.022.
- [108] J.H. Yang, Y. Gao, W. Zhang, P. Tang, J. Tan, A.H. Lu, D. Ma, Cobalt phthalocyanine-graphene oxide nanocomposite: Complicated mutual electronic interaction, J. Phys. Chem. C. 117 (2013) 3785–3788. doi:10.1021/jp311051g.
- [109] L. Cui, G. Lv, Z. Dou, X. He, Fabrication of iron phthalocyanine/graphene micro/nanocomposite by solvothermally assisted π - π Assembling method and its application for oxygen reduction reaction, Electrochim. Acta. 106 (2013) 272–278. doi:10.1016/j.electacta.2013.05.077.
- [110] C. Zhang, R. Hao, H. Yin, F. Liu, Y. Hou, Iron phthalocyanine and nitrogen-doped graphene composite as a novel non-precious catalyst for the oxygen reduction reaction,

- Nanoscale. (2012) 7326–7329. doi:10.1039/c2nr32612d.
- [111] S. Abdolhosseinzadeh, H. Asgharzadeh, H. Seop Kim, Fast and fully-scalable synthesis of reduced graphene oxide, Sci. Rep. 5 (2015) 10160. doi:10.1038/srep10160.
- [112] E. Proietti, F. Jaouen, M. Lefevre, N. Larouche, J. Tian, J. Herranz, J.-P. Dodelet, Iron-based cathode catalyst with enhanced power density in polymer electrolyte membrane fuel cells, Nat. Commun. 2 (2011) 1–6. doi:10.1038/ncomms1427.
- [113] P.-A. Pascone, J. de Campos, J.-L. Meunier, D. Berk, Iron Incorporation on Graphene Nanoflakes for the Synthesis of a Non-noble Metal Fuel Cell Catalyst, Appl. Catal. B Environ. 193 (2016) 9–15. doi:10.1016/j.apcatb.2016.04.002.
- [114] R. Pristavita, N.Y. Mendoza-Gonzalez, J.L. Meunier, D. Berk, Carbon blacks produced by thermal plasma: The influence of the reactor geometry on the product morphology, Plasma Chem. Plasma Process. 30 (2010) 267–279. doi:10.1007/s11090-010-9218-7.
- [115] U. Legrand, N.Y. Mendoza Gonzalez, P. Pascone, J.L. Meunier, D. Berk, Synthesis and in-situ oxygen functionalization of deposited graphene nanoflakes for nanofluid generation, Carbon N. Y. 102 (2016) 216–223. doi:10.1016/j.carbon.2016.02.043.
- [116] K. Shinozaki, J.W. Zack, R.M. Richards, B.S. Pivovar, S.S. Kocha, Oxygen Reduction Reaction Measurements on Platinum Electrocatalysts Utilizing Rotating Disk Electrode Technique: I. Impact of Impurities, Measurement Protocols and Applied Corrections, J. Electrochem. Soc. 162 (2015) F1144–F1158. doi:10.1149/2.1071509jes.
- [117] S.S. Kocha, Y. Garsany, D. Myers, Testing Oxygen Reduction Reaction Activity with the Rotating Disc Electrode Technique, DOE Webinar. (2013).
- [118] N. Ohno, M. Yoshimi, M. Tokitani, S. Takamura, K. Tokunaga, N. Yoshida, Spherical cauliflower-like carbon dust formed by interaction between deuterium plasma and graphite target and its internal structure, J. Nucl. Mater. 390–391 (2009) 61–64. doi:10.1016/j.jnucmat.2009.01.051.
- [119] J. Lu, X. Jiao, D. Chen, W. Li, Solvothermal Synthesis and Characterization of Fe 3 O 4 and γ -Fe 2 O 3 Nanoplates, (2009) 4012–4017.
- [120] N. Larouche, B.L. Stansfield, Classifying nanostructured carbons using graphitic indices derived from Raman spectra, Carbon N. Y. 48 (2010) 620–629. doi:10.1016/j.carbon.2009.10.002.
- [121] Q. Wei, X. Tong, G. Zhang, J. Qiao, Q. Gong, S. Sun, Nitrogen-Doped Carbon Nanotube and Graphene Materials for Oxygen Reduction Reactions, Catalysts. 5 (2015) 1574–1602. doi:10.3390/catal5031574.
- [122] T. Yamashita, P. Hayes, Analysis of XPS spectra of Fe2+ and Fe3+ ions in oxide materials, Appl. Surf. Sci. 254 (2008) 2441–2449. doi:10.1016/j.apsusc.2007.09.063.
- [123] S. Pylypenko, S. Mukherjee, T.S. Olson, P. Atanassov, Non-platinum oxygen reduction electrocatalysts based on pyrolyzed transition metal macrocycles, Electrochim. Acta. 53 (2008) 7875–7883. doi:10.1016/j.electacta.2008.05.047.
- [124] W. Zhou, L. Ge, Z.G. Chen, F. Liang, H.Y. Xu, J. Motuzas, A. Julbe, Z. Zhu, Amorphous iron oxide decorated 3D heterostructured electrode for highly efficient oxygen reduction, Chem. Mater. 23 (2011) 4193–4198. doi:10.1021/cm201439d.

- [125] V. Subramanian, R. Baskaran, H. Krishnan, Thermal Plasma Synthesis of Iron Oxide Aerosols and Their Characteristics, 9 (2009) 172–186.
- [126] M. Peuckert, Oxygen Reduction on Small Supported Platinum Particles, J. Electrochem. Soc. 133 (1986) 944. doi:10.1149/1.2108769.
- [127] U.A. Paulus, T.J. Schmidt, H.A. Gasteiger, R.J. Behm, Oxygen reduction on a high-surface area Pt/Vulcan carbon catalyst: A thin-film rotating ring-disk electrode study, J. Electroanal. Chem. 495 (2001) 134–145. doi:10.1016/S0022-0728(00)00407-1.
- [128] V.S. Bagotzky, N. V. Osetrova, A.M. Skundin, Fuel Cells: State-of-the-Art and Major Scientific and Engineering Problems, Russ. J. Electrochem. 39 (2003) 919–934. doi:10.1023/A:1025719619261.
- [129] J.-M. Le Canut, R.M. Abouatallah, D.A. Harrington, Detection of Membrane Drying, Fuel Cell Flooding, and Anode Catalyst Poisoning on PEMFC Stacks by Electrochemical Impedance Spectroscopy, J. Electrochem. Soc. 153 (2006) A857–A864. doi:10.1149/1.2179200.
- [130] F. Zhao, F. Harnisch, U. Schröder, F. Scholz, P. Bogdanoff, I. Herrmann, Application of pyrolysed iron(II) phthalocyanine and CoTMPP based oxygen reduction catalysts as cathode materials in microbial fuel cells, Electrochem. Commun. 7 (2005) 1405–1410. doi:10.1016/j.elecom.2005.09.032.
- [131] M. Musilová, J. Mrha, J. Jindra, Carbon electrodes with phthalocyanine catalyst in acid medium, J. Appl. Electrochem. 3 (1973) 213–218. doi:10.1007/BF00619163.
- [132] K. Parvez, S. Yang, Y. Hernandez, A. Winter, A. Turchanin, X. Feng, K. Müllen, Nitrogen-doped graphene and its iron-based composite as efficient electrocatalysts for oxygen reduction reaction, ACS Nano. 6 (2012) 9541–9550. doi:10.1021/nn302674k.
- [133] M. Jahan, Q. Bao, K.P. Loh, Electrocatalytically Active Graphene Porphyrin MOF Composite for Oxygen Reduction Reaction, J. Am. Chem. Soc. 134 (2012) 6707–6713.
- [134] Y. Liu, Y.Y. Wu, G.J. Lv, T. Pu, X.Q. He, L.L. Cui, Iron(II) phthalocyanine covalently functionalized graphene as a highly efficient non-precious-metal catalyst for the oxygen reduction reaction in alkaline media, Electrochim. Acta. 112 (2013) 269–278. doi:10.1016/j.electacta.2013.08.174.
- [135] T. Taniguchi, H. Tateishi, S. Miyamoto, K. Hatakeyama, C. Ogata, A. Funatsu, S. Hayami, Y. Makinose, N. Matsushita, M. Koinuma, Y. Matsumoto, A self-assembly route to an iron phthalocyanine/reduced graphene oxide hybrid electrocatalyst affording an ultrafast oxygen reduction reaction, Part. Part. Syst. Charact. 30 (2013) 1063–1070. doi:10.1002/ppsc.201300177.
- [136] P.-A. Pascone, J.-L. Meunier, D. Berk, Influence of iron on structure and catalyst activity of nitrogen-functionalized graphene nanoflakes, Mater. Today Commun. 9 (2016) 54–59. doi:10.1016/j.mtcomm.2016.10.003.
- [137] U. Legrand, J. Meunier, D. Berk, Iron functionalization of graphene nanoflakes in thermal plasma conditions for catalyst applications P-II-7-14, "Applied Catal. A, Gen. 528 (2015) 5–8. doi:10.1016/j.apcata.2016.09.015.
- [138] U. Legrand, N.Y. Mendoza Gonzalez, P. Pascone, J.L. Meunier, D. Berk, Synthesis and in-situ oxygen functionalization of deposited graphene nanoflakes for nanofluid generation, Carbon N. Y. 102 (2016) 216–223.

- [139] C. Chilian, G. Kennedy, The NAA method at Polytechnique Montreal: An efficient alternative way to use the k0 NAA models, J. Radioanal. Nucl. Chem. 300 (2014) 533–538. doi:10.1007/s10967-014-3025-1.
- [140] H.P. Boehm, Surface oxides on carbon and their analysis: A critical assessment, Carbon N. Y. 40 (2002) 145–149. doi:10.1016/S0008-6223(01)00165-8.
- [141] P. Chen, T.Y. Xiao, Y.H. Qian, S.S. Li, S.H. Yu, A nitrogen-doped graphene/carbon nanotube nanocomposite with synergistically enhanced electrochemical activity, Adv. Mater. 25 (2013) 3192–3196. doi:10.1002/adma.201300515.
- [142] D. Yang, A. Velamakanni, G. Bozoklu, S. Park, M. Stoller, R.D. Piner, S. Stankovich, I. Jung, D.A. Field, C.A. Ventrice, R.S. Ruoff, Chemical analysis of graphene oxide films after heat and chemical treatments by X-ray photoelectron and Micro-Raman spectroscopy, Carbon N. Y. 47 (2009) 145–152. doi:10.1016/j.carbon.2008.09.045.
- [143] A.C. Ferrari, Raman spectroscopy of graphene and graphite: Disorder, electron-phonon coupling, doping and nonadiabatic effects, Solid State Commun. 143 (2007) 47–57. doi:10.1016/j.ssc.2007.03.052.
- [144] G. Wu, C.M. Johnston, N.H. Mack, K. Artyushkova, M. Ferrandon, M. Nelson, J.S. Lezama-Pacheco, S.D. Conradson, K.L. More, D.J. Myers, P. Zelenay, Synthesis-structure-performance correlation for polyaniline-Me-C non-precious metal cathode catalysts for oxygen reduction in fuel cells, J. Mater. Chem. 21 (2011) 11392–11405. doi:10.1039/c0jm03613g.
- [145] Y. Zhang, T. Han, J. Fang, P. Xu, X. Li, J. Xu, C.-C. Liu, Integrated Pt2Ni alloy@Pt core-shell nanoarchitectures with high electrocatalytic activity for oxygen reduction reaction, J. Mater. Chem. A. 2 (2014) 11400–11407. doi:10.1039/C4TA00731J.
- [146] S.J. Amirfakhri, D. Binny, J. Meunier, D. Berk, Investigation of hydrogen peroxide reduction reaction on graphene and nitrogen doped graphene nano fl akes in neutral solution, J. Power Sources. 257 (2014) 356–363. doi:10.1016/j.jpowsour.2014.01.114.
- [147] S. Mukerjee, S. Srinivasan, Enhanced electrocatalysis of oxygen reduction on platinum alloys in proton exchange membrane fuel cells, J. Electroanal. Chem. 357 (1993) 201–224. doi:10.1016/0022-0728(93)80380-Z.
- [148] J. Greeley, I.E.L. Stephens, a S. Bondarenko, T.P. Johansson, H. a Hansen, T.F. Jaramillo, J. Rossmeisl, I. Chorkendorff, J.K. Nørskov, Alloys of platinum and early transition metals as oxygen reduction electrocatalysts., Nat. Chem. 1 (2009) 552–556. doi:10.1038/nchem.367.
- [149] M.A. Olivella, J.M. Palacios, A. Vairavamurthy, J.C. Del Río, F.X.C. De Las Heras, A study of sulfur functionalities in fossil fuels using destructive- (ASTM and Py-GC-MS) and non-destructive- (SEM-EDX, XANES and XPS) techniques, Fuel. 81 (2002) 405–411. doi:10.1016/S0016-2361(01)00198-3.
- [150] J. Park, Y.J. Jang, Y.J. Kim, M.-S. Song, S. Yoon, D.H. Kim, S.-J. Kim, Sulfur-doped graphene as a potential alternative metal-free electrocatalyst and Pt-catalyst supporting material for oxygen reduction reaction., Phys. Chem. Chem. Phys. 16 (2013) 103–9. doi:10.1039/c3cp54311k.
- [151] S. Yang, L. Zhi, K. Tang, X. Feng, J. Maier, K. M??llen, Efficient synthesis of heteroatom (N or S)-doped graphene based on ultrathin graphene oxide-porous silica sheets for oxygen reduction reactions, Adv. Funct. Mater. 22 (2012) 3634–3640. doi:10.1002/adfm.201200186.

- [152] M. Schmid, H.P. Steinrück, J.M. Gottfried, A new asymmetric Pseudo-Voigt function for more efficient fitting of XPS lines, Surf. Interface Anal. 46 (2014) 505–511. doi:10.1002/sia.5521.
- [153] L. Bokobza, J.-L. Bruneel, M. Couzi, Raman Spectra of Carbon-Based Materials (from Graphite to Carbon Black) and of Some Silicone Composites, C—Journal Carbon Res. 1 (2015) 77–94. doi:10.3390/c1010077.
- [154] P.D. Harvey, I.S. Butler, Raman spectra of orthorhombic sulfur at 40 K, J. Raman Spectrosc. 17 (1986) 329–334. doi:10.1002/jrs.1250170407.
- [155] B. Downs, S. Robinson, H. Yang, P. Mooney, RRUFF, (n.d.). http://rruff.info/Sulfur/R050006.
- [156] K. Tanaka, K. Yoshizawa, T. Takeuchi, J.U.N. Yamauchi, Plasma polymerization of thiophene and 3-methylthiophene, 38 (1990) 107–116.
- [157] Y. Zhou, S.L. Candelaria, Q. Liu, Y. Huang, E. Uchaker, G. CaO, Sulfur-rich carbon cryogels for supercapacitors with improved conductivity and wettability, J. Mater. Chem. A. 2 (2014) 8472. doi:10.1039/c4ta00894d.
- [158] C. Li, G. Shi, Polythiophene-based optical sensors for small molecules, ACS Appl. Mater. Interfaces. 5 (2013) 4503–4510. doi:10.1021/am400009d.
- [159] Y. Shao, J. Wang, H. Wu, J. Liu, I. a. Aksay, Y. Lin, Graphene based electrochemical sensors and biosensors: A review, Electroanalysis. 22 (2010) 1027–1036. doi:10.1002/elan.200900571.
- [160] X. Li, W. Cai, J. An, S. Kim, J. Nah, D. Yang, R. Piner, A. Velamakanni, I. Jung, E. Tutuc, S.K. Banerjee, L. Colombo, R.S. Ruoff, Large-area synthesis of high-quality and uniform graphene films on copper foils., Science. 324 (2009) 1312–1314. doi:10.1126/science.1171245.
- [161] M. Choucair, P. Thordarson, J. a Stride, Gram-scale production of graphene based on solvothermal synthesis and sonication., Nat. Nanotechnol. 4 (2009) 30–33. doi:10.1038/nnano.2008.365.
- [162] Y. Hernandez, V. Nicolosi, M. Lotya, F.M. Blighe, Z. Sun, S. De, I.T. McGovern, B. Holland, M. Byrne, Y.K. Gun'Ko, J.J. Boland, P. Niraj, G. Duesberg, S. Krishnamurthy, R. Goodhue, J. Hutchison, V. Scardaci, A.C. Ferrari, J.N. Coleman, High-yield production of graphene by liquid-phase exfoliation of graphite., Nat. Nanotechnol. 3 (2008) 563–568. doi:10.1038/nnano.2008.215.
- [163] S. Park, R.S. Ruoff, Chemical methods for the production of graphenes., Nat. Nanotechnol. 4 (2009) 217–224. doi:10.1038/nnano.2009.58.
- [164] Y. Zhu, S. Murali, W. Cai, X. Li, J.W. Suk, J.R. Potts, R.S. Ruoff, Graphene and graphene oxide: Synthesis, properties, and applications, Adv. Mater. 22 (2010) 3906–3924. doi:10.1002/adma.201001068.
- [165] N. McEvoy, H. Nolan, N. Ashok Kumar, T. Hallam, G.S. Duesberg, Functionalisation of graphene surfaces with downstream plasma treatments, Carbon N. Y. 54 (2013) 283–290. doi:10.1016/j.carbon.2012.11.040.
- [166] A.J. Marsden, P. Brommer, J.J. Mudd, M.A. Dyson, R. Cook, M. Asensio, J. Avila, A. Levy, J. Sloan, D. Quigley, G.R. Bell, N.R. Wilson, Effect of oxygen and nitrogen functionalization on the physical and electronic structure of graphene, Nano Res. 8 (2015) 1–16. doi:10.1007/s12274-015-0768-0.

- [167] M. Baraket, S.G. Walton, E.H. Lock, J.T. Robinson, F.K. Perkins, The functionalization of graphene using electron-beam generated plasmas, Appl. Phys. Lett. 96 (2010) 10–12. doi:10.1063/1.3436556.
- [168] S.C. Hernández, V.D. Wheeler, M.S. Osofsky, G.G. Jernigan, V.K. Nagareddy, A. Nath, E.H. Lock, L.O. Nyakiti, R.L. Myers-Ward, K. Sridhara, A.B. Horsfall, C.R. Eddy, D.K. Gaskill, S.G. Walton, Plasma-based chemical modification of epitaxial graphene with oxygen functionalities, Surf. Coatings Technol. 241 (2014) 8–12. doi:10.1016/j.surfcoat.2013.11.015.
- [169] M. Yi, W. Zhang, Z. Shen, X. Zhang, X. Zhao, Y. Zheng, S. Ma, Controllable functionalization and wettability transition of graphene-based films by an atomic oxygen strategy., J. Nanopart. Res. 15 (2013) 1811–1824. doi:10.1007/s11051-013-1811-2.
- [170] Y. Sun, Q. Wu, G. Shi, Graphene based new energy materials, Energy Environ. Sci. 4 (2011) 1113–1132. doi:10.1039/c0ee00683a.
- [171] P. V. Lakshminarayanan, H. Toghiani, C.U. Pittman, Nitric acid oxidation of vapor grown carbon nanofibers, Carbon N. Y. 42 (2004) 2433–2442. doi:10.1016/j.carbon.2004.04.040.
- [172] T. Tański, Investigation of the Structure and Properties of PVD and PACVD-Coated Magnesium Die Cast Alloys, in: New Featur. Magnes. Alloy., 2012. doi:10.5772/2810.
- [173] S. Reich, C. Thomsen, Raman spectroscopy of graphite., Philos. Trans. A. Math. Phys. Eng. Sci. 362 (2004) 2271–2288. doi:10.1098/rsta.2004.1454.
- [174] A. Felten, A. Eckmann, J.-J. Pireaux, R. Krupke, C. Casiraghi, Controlled modification of mono- and bilayer graphene in O2, H2 and CF4 plasmas., Nanotechnology. 24 (2013) 355705. doi:10.1088/0957-4484/24/35/355705.
- [175] D. Bom, R. Andrews, D. Jacques, J. Anthony, B. Chen, M.S. Meier, J.P. Selegue, Thermogravimetric Analysis of the Oxidation of Multiwalled Carbon Nanotubes: Evidence for the Role of Defect Sites in Carbon Nanotube Chemistry, Nano Lett. 2 (2002) 615–619. doi:10.1021/nl020297u.
- [176] L.S.K. Pang, J.D. Saxby, S.P. Chatfield, Thermogravimetric Analysis of Carbon Nanotubes and Nanoparticles, J. Phys. Chem. 97 (1993) 6941–6942. doi:10.1113/jphysiol.2011.220392.
- [177] V. Chabot, B. Kim, B. Sloper, C. Tzoganakis, A. Yu, High yield production and purification of few layer graphene by gum arabic assisted physical sonication., Sci. Rep. 3 (2013) 1378–1385. doi:10.1038/srep01378.
- [178] R.J. Hunter, Zeta Potential in Colloid Science: Principles and Applications, Academic Press, 1988.
- [179] P. Taylor, T.C. Bond, R.W. Bergstrom, T.C. Bond, R.W. Bergstrom, Light Absorption by Carbonaceous Particles: An Investigative Review, Aerosol Sci. Technol. 40 (2007) 27–67. doi:10.1080/02786820500421521.